DYNAMICALLY TUNABLE DIELECTRIC HUYGENS METASURFACES:

AN EMERGING FRAMEWORK FOR ACTIVELY RECONFIGURABLE PHOTONIC DEVICES

AN ABSTRACT

SUBMITTED ON THE 29th OF AUGUST 2022

TO THE DEPARTMENT OF PHYSICS

IN PARTIAL FULFILMENT OF THE REQUIREMENTS OF THE SCHOOL OF SCIENCE AND ENGINEERING

AT TULANE UNIVERSITY, FOR THE DEGREE OF

DOCTOR OF PHILOSOPHY

BY

ISAAC OLUWASEGUN OGUNTOYE

APPROVED:

Matthew D. Escarra, Ph.D.
Director

Ryan Glasser, Ph.D.

Jiang Wei, Ph.D.

Abstract

Optical metamaterials have naturally followed the law of increasing miniaturization to yield unprecedented manipulation and control of light at the nanoscale, thus paving the way toward the realization of next-generation photonic devices. These devices, based on two-dimensional flat metasurfaces, are already proving to be more compact and efficient when compared to their traditional bulky counterparts. Most of the ongoing research in this field has focused on static functionality, where optical performance is fixed after fabrication and cannot be altered. Hence, the scope of possible exciting applications is limited to only passive performance.

Taking advantage of the abundance of external stimuli around us, such as temperature, pressure, stress, strain, electric field, and light, active optical metasurfaces can be realized which expand the frontiers of realizable implementations of photon-matter interactions. This dissertation surveys different approaches toward obtaining dynamic reconfigurability in dielectric Huygens metasurface platforms. Dielectric Huygens metasurfaces have been demonstrated to show unique optical performance by supporting multipolar resonance modes which can be spectrally manipulated by changes in geometry, incidence angle, and refractive index. This creates a versatile platform to achieve multifunctional metasurfaces via various tuning methods. Also, the choice of dielectric materials over plasmonics is beneficial due to lower dissipative losses, excitation of multipolar resonances, and potential CMOS adaptability.

This dissertation is split into four important chapters. Chapter 2 discusses the prototyping of a custom-built sensor for refractive index measurement and biomarker detection. By tuning the refractive index of the capping fluid, the optical performance of the metasurface was altered,

enabling the full characterization of the bulk fluid. This same approach was used to characterize culture filtrate peptide (CFP-10), a prominent tuberculosis biomarker that yielded different optical responses for different concentrations. Chapter 3 studies a well-known phase transition material, vanadium dioxide (VO_2), whose optical performance is altered from semiconducting properties to metallic properties above its transition temperature (68^{o}C). Changing the refractive index of resonant VO_2 nanostructures leads to decoupled phase modulation and amplitude modulation at different wavelengths. Chapter 4 investigates mutual coupling in nanoantenna arrays. A figure of merit is proposed for estimating the nearest neighbor crosstalk in these systems. To experimentally verify this, three silicon-based Huygens beam deflectors were designed and fabricated. Chapter 5 shows efforts toward achieving highly efficient tunable metasurface holograms. A phase map is generated from the original intensity map using the Gerchberg-Saxton algorithm. The triangulation method for obtaining a nanoantenna-phase map is proposed and tested for three-point emitters whose amplitude and phase information are known.

In summary, we examine the exciting physics of tunable dielectric Huygens metasurfaces and engineer them to realize fascinating functionality in diverse applications.

DYNAMICALLY TUNABLE DIELECTRIC HUYGENS METASURFACES:

AN EMERGING FRAMEWORK FOR ACTIVELY RECONFIGURABLE PHOTONIC DEVICES

A DISSERTATION

SUBMITTED ON THE 29th OF AUGUST 2022

TO THE DEPARTMENT OF PHYSICS

IN PARTIAL FULFILMENT OF THE REQUIREMENTS OF THE SCHOOL OF SCIENCE AND ENGINEERING

AT TULANE UNIVERSITY, FOR THE DEGREE OF

DOCTOR OF PHILOSOPHY

BY

ISAAC OLUWASEGUN OGUNTOYE

APPROVED:

Matthew D. Escarra, Ph.D.
Director

Ryan Glasser, Ph.D.

Jiang Wei, Ph.D.

Acknowledgments

The Almighty God, The Father of lights, whose help and strength I have greatly received to put this work together

Prof. Matthew D. Escarra, for your incredible patience and attention to detail throughout these five years. I am grateful for working with you for these five years. Also, I want to highlight here that I received what is arguably the best gift during my graduate school from you in Romans 5:3-5. As I read the email where you sent this to me again this morning, it just brought tears back to my eyes. There were times during graduate school when these verses were what assured me that it will end well. I felt like I experienced how “suffering” led to perseverance, perseverance yielded character, and character gradually produced and is producing hope. I knew that through the ups and downs of graduate school it was going to end well. Thank you so much for this, your advice, and your support.

Prof. Ryan Glasser and Prof. Jiang Wei, for being on my committee and providing edits and suggestions in this work.

Dr. Michael Johnson, for timeless hours of troubleshooting, training, and problem-solving. One of the most favorite things about graduate school for me was just staying with you to troubleshoot and learn as much as I can.

Dr. Jibao He, for help and reassuring words during SEM hours.

Dr. Xiaodong Zhang, for assistance with XPS measurements and analysis.

Dr. John Robertson, Dr. Adam Ollanik, Dr. Yaping Ji, Dr. Kazi Islam, Timothy Ismael, Siddharth Padmanabha, and Aamir Abbas for supporting, encouraging, advising, and helping to make this a success.

Dr. Peisong Peng, Dr. Xiaojiang Li, Ron Koshita, and Kaitlyn Prenger for many hours of research and coursework rants and assistance.

Zack Hartfield, Brittany Simone, Thalia Koutsougeras, Max Hinkle for wonderful ideas, energy, and support on the exciting metasurface projects in the lab.

Members of our Friday Bible study group, for continuous encouragement, laughter, and fun.

Members of ChiAlpha Life group, for food, fun, laughter, and cooperate Bible study and prayer.

Dad, Mom, Pst. Mayowa, Sis. Dunni, Aunty Moyin, Bro. Moses, Sis. Bisi, for all your calls, prayers, supports, and advise.

Dr. Olalekan Afuye, Daniel Akuma, and Gbolahan Adeola, my three secondary school friends who motivated me in my academic pursuits. Special acknowledgement for Dr. Afuye, who provided support and help while writing this dissertation.

I would like to acknowledge three people here especially. First, my brother Dr. Moses Oguntoye whose advise and help was very vital towards completing this degree. Second, ChiAlpha Director, Revd. Matt DeGier, whose prayers, encouragements, exposure, and advise helped me to grow. Third, and by no means the least, Busayo Alagbe, who is a friend that has stuck and will stick closer to me like a brother. Thank you for being there with me through the grind and rough roads as well as all the pleasurable moments.

Finally, thanks to everyone who has been part of this success story. I can’t thank you enough.

Table of Contents

List of Figures

List of Tables

Chapter 1 – Introduction

The dawn of the 21st century has led to further unraveling of the mystery of light and paved the way for new methods to useful performance for the benefit of the universe. Since the beginning of time, the daily routine of every creature in the universe has involved light. From the early sunshine at dawn to tales by moonlight, every activity is laced with the influence of light waves. The enigma surrounding the concept of light opened the portal to understanding its fundamental properties.

One of the big moments in this pursuit occurred in the 19th century when James Clerk Maxwell proved mathematically that light is an electromagnetic wave. This was pivotal in unifying optics and electromagnetism. This also deepened the understanding of researchers and was helpful in the development of optical communication networks requiring the use of antennas such as in mobile phones, satellites, laptops, and so on. These antennas can establish communication by transmitting and receiving radio waves with frequencies from 300 GHz to 3 kHz[1]. So, the natural question that follows is: Can this concept of transmission and reception be applied to optical frequencies? Previous work done by Faraday, Maxwell, Heaviside, Hertz in the 19th century can provide an answer to that. Basically, the answer is yes. The same operational guidelines for transmission and reception of electromagnetic waves are not constrained to work in only a certain region of the electromagnetic spectrum. This has led to extensive research and implementation of various nano- and microscale devices functioning from the microwave to the ultraviolet regime of the electromagnetic spectrum. This gradually resulted in the demonstration of negative refraction in the early 2000s which is one of the distinct phenomena that occurs in metamaterials.

1.1 – Metasurface Overview

It is important to dig a little deeper into the concept of metamaterials before touching on the topic of metasurfaces. Metamaterials have been defined as man-made structured materials that obtain their properties from the unit structure rather that its constituent materials[2]. Also, for a material to be called an optical metamaterial, its geometric dimensions must be subwavelength in scale.

It is not easy to pinpoint a certain time in history when the first metamaterial was produced. It is known however, that metamaterials have been used from as early as the 4th century in the Lycurgus Cup, which is made from ruby glass with gold nanoparticles immersed within. The metamaterial appeared green when seen in daylight and reddish with light transmitted through glass[3]. At the end of the 19th century, Bose proposed a "twisted jute" material possessing chiral properties which perhaps was one of the first modern artificially made structured materials[4]. There was also the development of artificial dielectrics, which are repeated patterned arrays of metallic wires, spheres or plates, investigated by around the middle of the 20th century. Taking a quantum leap from fundamental science towards applications, there were interesting research demonstrations of metamaterial functionality, such as Veselago media, which are a practical proof of a left-handed phenomenon[5], and perfect lensing[6]. Metamaterials are typically subdivided into many branches including acoustic, elastic, electromagnetic, and thermal metamaterials[7]. The focus of this dissertation is briefly on electromagnetic metamaterials and extensively on their quasi 2-D counterparts, optical metasurfaces.

Every material's reaction to external electromagnetic fields is largely governed by only two material parameters, permittivity (ε) and permeability (μ). Due to this dependence, an

electromagnetic parameter space can be defined to classify materials based on the values of these two parameters[2]. As shown in **Figure 1.1**, each material type is placed in a quadrant of the circle based on the sign of the value of ε and μ.

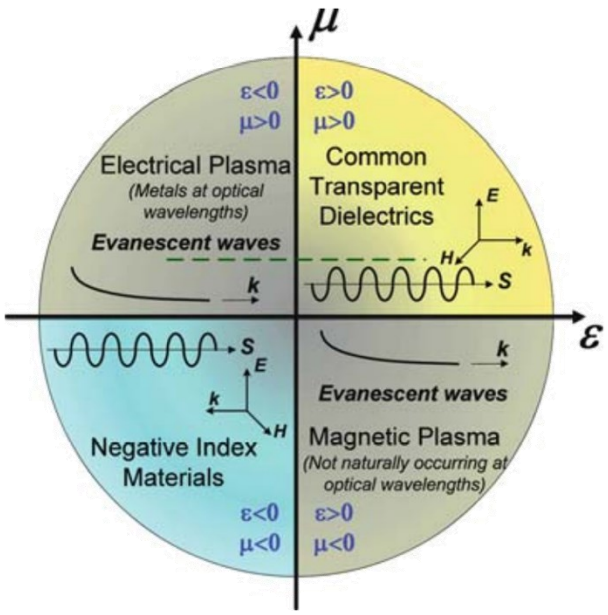

Figure 1.1: Electromagnetic parameter space for ε and μ.

Adapted from "Optical Metamaterials – Fundamentals and Applications" by W. Cai and V. Shalaev. The two black solid lines correspond to the real parts of ε and μ based on the direction of the arrow. The green dashed line depicts non-magnetic materials with μ = 1.

Traditionally known optically transparent materials are found in the first quadrant where the ε and μ values are positive. In the second quadrant, a negative value of ε shows that the direction of the electric field induced inside the material is in the opposite direction to the incident field. Examples of materials that show this behavior are noble metals at optical frequencies. In the third quadrant, negative values of ε and μ are for materials that do not exist in nature. These kind of materials are artificially made or tailored to yield interesting optical phenomena such as

negative refraction and backward propagation[7]. In the fourth quadrant, a negative value of μ informs that the direction of the magnetic field induced inside the material is in the opposite direction to the incident field. Examples of these materials are ferromagnetic media near a resonance.

Due to their 3-D, nanoscale structure, metamaterials pose fabrication challenges that limit their optimized performance. Metasurfaces are 2-D periodic or aperiodic arrays of subwavelength dimensions that can manipulate light in nontraditional ways. They can impart a sudden shift in amplitude, phase, wavenumber, and/or polarization of the impinging beam. Their diminished geometric degree of freedom relative to metamaterials minimizes the fabrication challenge and is useful for realizing unprecedented optical functionality. Metasurfaces can be divided into two classes based on their material platform and geometry/orientation. Based on their material platform, metasurfaces could be plasmonic, dielectric, or a hybrid of plasmonics and dielectrics. Dielectrics are preferred to their plasmonic counterparts because they have low absorptive losses at optical frequencies. Based on their geometry/orientation, they could be PB-phase metasurfaces, truncated waveguide metasurfaces, or Huygens metasurfaces. Each of these metasurface types have distinct properties and limitations[8].

Until recently, most of the demonstrated metasurface applications in literature have been static, that is, their function is encoded at the time of fabrication and cannot be altered due to an external stimulus. Active metasurfaces, however are desired for displays, optical neural networks, filters, compact beam-steering devices, tunable metalenses, holography, and much more.

1.2 – Actively Reconfigurable Metasurfaces

Dynamically tunable metasurfaces can have their optical properties altered by external stimuli. Examples of these stimuli include electric field, magnetic field, temperature, pressure, strain, and optical pumping. In general, there are three distinct channels through which the optical functionality of a metasurface can be altered post-fabrication[9] .

The first method is by tuning the metasurface geometry. This can be achieved using stretchable materials like PDMS or PMMA to mechanically shrink or expand the spacing between adjacent resonators, thereby altering the nearest neighbor coupling between the resonators. Reconfigurable metasurface lensing has been shown using this approach[10,11]. The second method is by tuning the nanoantenna environment. This can be realized by using external control parameters such as temperature, applied voltage, or fluid motion over the metasurface. Bulk refractive index sensing and biomarker detection have been demonstrated through this approach[12]. The third method is by tuning the resonator material. This is obtained by changing the optical properties of the material(s) that make up the resonator material by an external stimulus. Refractive index tuning of resonator materials can be realized through thermo-optic effects, free carrier excitation, piezoelectricity, and applied voltage. These resonators could also be made from phase change materials where you can achieve refractive index modulation using thermal, optical, and electrical means to modify the material's phase. Each of the above mentioned tuning methods can lead to one or a mixture of these resultant effects in resonant dielectric metasurfaces, namely a spectral relocation of the metasurface resonances, an alteration in resonant intensity, or a disappearing or reappearing of resonances[9].This dissertation focuses on the second and third tuning

methods described above and discusses the applications of these methods in fluidic sensing and continuously tuned amplitude and phase modulation in VO_2 Huygens metasurfaces.

1.3 – Thesis Overview

This dissertation discusses active tunability in dielectric Huygens metasurfaces and is divided into four chapters. Two of the chapters focus on detailed applications of optical tunability through sensing and switching. The other two chapters focus on the development of complex optical fields such as holograms and how this low aspect ratio dielectric platform can be optimized for achieving highly efficient performance.

Chapter 2 discusses the implementation of a portable and relatively cheap bulk refractive index sensor and biomarker detector. Evanescent wave coupling between nearest neighbor antennas is exploited to achieve active tuning by changing the environment of the nanoantennas. A single chip containing multiple metasurfaces with different resonance effects is used to demonstrate the versatility of the system. We show a computational sensitivity of 5.8 T/RIU and 11.1 T/RIU for the lower quality factor Mie resonance metasurface and the higher quality factor asymmetric resonance metasurface, respectively. By flowing different concentrations of saline over the metasurface, a limit of detection of 1.9×10^{-6} is demonstrated, which agrees well with state-of-the-art dielectric refractive index sensing systems to date. Finally, a tuberculosis biomarker (CFP-10 peptide) is tested across different concentrations. A limit of detection of 10 pM corresponding to 16 $pgmL^{-1}$ is obtained. Opportunities for sensor testbed improvement and development for greater versatility and for more advanced biomarker characterization, compared with state-of-the-art and expensive industrial tools, are discussed.

Chapter 3 focuses on the tunability of the nanomaterial itself, leading to continuously active modulation in Huygens metasurfaces. Taking advantage of the dielectric to plasmonic refractive index modulation accessible in vanadium dioxide, tunable optical modulators can be implemented. A single dual-function metasurface chip, designed to function as an amplitude modulator with suppressed residual phase modulation at one wavelength, and as a phase modulator with reduced residual amplitude modulation at another wavelength is illustrated. Computationally, gradual thermal control results in maximum amplitude modulation of 19 dB with a residual phase modulation of ~35^{o} at 1920 nm. Also, maximum phase modulation of 228^{o} with residual amplitude modulation of ~4 dB is obtained. Possibilities towards obtaining a 360^{o} total phase shift are mentioned. Also, other potential applications of dynamic tunability using vanadium dioxide are discussed.

Chapter 4 explores an intrinsic characteristic of antennas that are near each other: mutual coupling. This effect is most pronounced in low aspect ratio Huygens nanoantennas as well as nanoantennas with a low index contrast relative to their surroundings. Engineered Huygens metasurface designs based on dielectric materials can result in higher optical confinement and suppressed nearest neighbor crosstalk. Three different dielectric Huygens metasurface designs are studied: silicon nanodisks, silicon nanodonuts, and silicon nanobeignets. A coupling figure of merit is proposed that is based on the interaction of a nanoantenna with a fixed geometry interacting with its nearest neighbor whose geometry is varied. This figure of merit examines how the optical performance (amplitude and phase) of the fixed geometry deviates from the performance of a homogenous array (where nearest neighbors are identical) with changes in the varied nanoantenna geometry. The calculated coupling figure of merit values for each of the geometries studied are: 0.52 (nanodisk), 0.42 (nanodonut), and 0.59 (nanobeignet). The nanodonut

geometry has the least coupling, suggesting that it has better confinement. Beam deflectors are designed and fabricated to experimentally verify the proposed coupling metric. Computational beam deflection efficiencies of ~65% (nanodisk), 47% (nanodonut), and 28% (nanobeignet) are obtained. A future test towards confirming the robustness of the proposed figure of merit is proposed.

Chapter 5 reports the attempt towards obtaining a highly efficient tunable metasurface hologram. The Kerker's condition of enhanced forward scattering and minimized backward scattering due to constructive interference of electric and magnetic dipole modes, when met in these metasurfaces, could be of huge significance towards making highly efficient holographic displays. Nearest neighbor coupling between these nanoantennas, though beneficial in some cases, is deleterious in the design and fabrication of complex optical devices because of the inability to independently encode optical information in each nanoantenna. A computed phase hologram is shown using the Gerchberg-Saxton algorithm. The triangulation method is implemented to obtain a nanoantenna-to-phase map and is successfully tested with three-point emitters whose amplitude and phase information is already known. A path towards obtaining accurate point-by-point mapping between the nanoantenna and phase map is briefly discussed.

Chapter 2 – Metasurface-Based Refractive Index and Biomarker Sensing

2.1 – Chapter Overview

Biomarker detection and bulk refractive index sensing are essential across multiple industries ranging from early medical diagnosis to chemical process quality control. The bulky size, high cost, and complex architecture of existing refractive index and biomarker sensing technologies limit their use to highly professional environments like hospitals, large food processing plants, and research labs. Therefore, point-of-care testing and detection are needed to facilitate rapid and early detection of trace molecules in bulk fluids and biofluids. One way we can demonstrate tunability in metasurface applications is actively tuning the environment of the nanoantenna array, namely the encapsulant or the substrate. Here, we demonstrate a compact and inexpensive refractive index sensor based on resonant dielectric photonic nanoantenna arrays or metasurfaces while tuning the encapsulant medium to provide different optical responses based on different media used. These dielectric resonances support Mie dipole and asymmetric resonances that shift with changes in their external environment. A single wavelength transmission measurement in a portable (<250 $in.^3$), low-cost (<$4,000) sensor shows sensitivity to 1.9×10^{-6} change in the fluid refractive index without the use of a spectrometer or other complex optics. Our sensor assembly allows measurements using multiple metasurfaces with identical resonances or varying resonance types for enhanced diagnostics on the same chip. Furthermore, 10-kDa culture filtrate peptide CFP-10, a marker for human tuberculosis, is detected with our sensor with 10 pM

resolution. This system has the potential to enable facile, fast, and susceptible measurements with adequate limits of detection for personalized biomedical diagnoses.

2.2 – Introduction

Refractive index sensing has garnered much attention due to its usefulness in determining fluid concentration, food contamination, biomedical diagnosis, and trace gas detection[13]. The ability of light to change its speed as it traverses from one medium to another represents an important measurement helpful in characterizing the composition of a bulk fluid[14]. Conventional refractive index sensing platforms are large and expensive, limiting scalable deployment and applicability. Many of these are based on complex instrumentation or beam propagating mechanisms such as prisms, interferometers, spectrometers, and optical fibers[15]. Their large and complex form makes them difficult for portable and robust on-chip device integration, thus limiting the usability of these systems to highly skilled technicians in industry or research labs. These include surface plasmon resonance (SPR) based sensors, relying on electromagnetic field oscillations along the interface between a metal and a dielectric, e.g., prism-coupled Kretschmann structured sensors[16–18], localized surface plasmon resonance (LSPR) based sensors[19–21], and fiber gratings[22]. Also, LSPR and SPR-based sensing methods have been combined in plasmonic nanohole arrays, utilizing their extraordinary transmission for refractive index sensing[23,24]. Each of these methods presents a unique way of tracking changes in the refractive index of fluids. Surface plasmon resonance-based sensing has been extended for use in biosensor applications in industry through implementation in the Biacore system. Although this method has proven to be highly sensitive, it also relies on complex optics for functionality[25,26]. The highly absorbing nature of plasmonic materials at visible and infrared wavelengths could limit

the application of these sensors due to absorption-induced heating. Interferometric-based based sensors have been developed and studied extensively for plasmonic platforms[27]; many of highly sensitive methods still requires the use of external spectroscopy for characterization[28]. Additionally, two dimensional materials have been utilized for photonic enhanced refractive index sensing, namely graphene and similar materials with high chemical stability and bio compatability[29]. These materials are typically integrated into plasmonic sensing platforms, implying the same drawbacks of cost and complexity. Dielectric nanoparticles and nanoresonator arrays are preferred over their plasmonic counterparts as the antenna material for our metasurfaces due to their low absorption losses, and thu high efficiency, in the near-infrared regime of the electromagnetic spectrum[30]. Many platforms have been demonstrated using dielectric based structures designed to locally interrogate refractive index changes in their environment. Examples include Bloch surface wave-based photonic crystal sensors. While achieving a high resolution, the propagating Bloch surface wave (BSW) platform depend on a prism and spectrometer for spectrally resolving local refractive index variations. Recently, a simple common path interferometric based sensor was demonstrated; however, the optics components used present challenges for compact device integration[31]. The aim of this work is to present an all-in-one device utilizing a low-cost dielectric metasurface-based resonant platform for highly sensitive bulk fluid refractive index sensing. This same approach can be used for biomolecule detection, where adsorption of the biomarker of interest onto the metasurface similarly disturbs the resonances and corresponding transmission.

To validate its performance, this sensor is demonstrated to accurately measure tuberculosis (TB), one of the top ten most deadly diseases worldwide. While the number of people with access to preventive treatment has grown in recent years, access to quality and prompt detection is still a

challenge. The World Health Organization predicted that a 50% drop in TB detection over a period of three months could have resulted in 400,000 additional deaths in countries with high TB cases in 2020.[32] This, as well as the recent global COVID-19 pandemic, has accentuated the need for accurate, fast, inexpensive, and reliable methods for label-free biomolecule detection in the world today. Although some demonstrations of label-free resonant photonic biosensors have been done for various biomolecules such as streptavidin[33], immunoglobin G antibody[34], and prostate-specific antigen[25], most efforts have been made towards proof-of-concept demonstrations and not so much on implementation of a novel photonic sensing method in a low-price and portable sensor. Here, we design and assemble a compact and low-cost optoelectronic sensor for bulk and surface refractive index sensing as well as TB biomarker surface analyte detection using a dielectric nanodisk array platform.

2.2.1 – Principle of Refractive Index Sensing

The strong forward or backward scattering in dielectric subwavelength nanoantennas is possible due to the simultaneous excitation of electric and magnetic dipole modes. Obtaining high scattering efficiencies in either direction is achieved by interference of these resonant modes. Here we illustrate our dielectric nanoantenna array based on amorphous silicon on a glass substrate. The structure and dimensions of this dielectric platform are shown in **Figure 2.1a**. These dielectric nanoantenna arrays, or Huygens metasurfaces, can be engineered such that the electric and magnetic dipole resonances are spectrally aligned as shown in **Figure 2.1c**, leading to near unity transmittance at the resonant wavelength. On the contrary, a careful spectral misalignment of the electric and magnetic dipole resonances leads to high reflectance, resulting from these destructively interfering modes[35] (**Figure 2.1d**). The slope of the metasurface-induced reflectance

peak, in addition to the spectral shift of this peak caused by varying the encapsulant index, makes it possible to perform single wavelength measurements using transmittance shift as the detected optical response. This may be accomplished without any deviation in optical path and without the use of complex or expensive optics, such as a spectrometer. The low-loss nature of these dielectric metasurfaces makes them preferable to their plasmonic counterparts. This resonant interaction is accompanied by coupling to their nearest neighbor antennas. This coupling leads to undesirable effects in certain static applications such as beam deflectors, where phase-gradient metasurfaces are used. However, it is a strong advantage for applications such as surface analyte detection and bulk fluid sensing involving photon-matter coupling in the metasurface surroundings[36,37]. The evanescent field around the resonators is sensitive to changes in the refractive index of the nanoantenna environment (**Figure 2.1b**). As a further advantage, these Huygens metasurfaces have a low aspect ratio, allowing easy fabrication and precise engineering of their dimensions to achieve electric and magnetic dipole resonances designed to interact with specific fluids and biomolecules (fabrication steps are shown in **Figure 2.1e**). The light-matter interactions in these metasurfaces depend on the size and shape of the meta-atoms as well as their material properties[38].

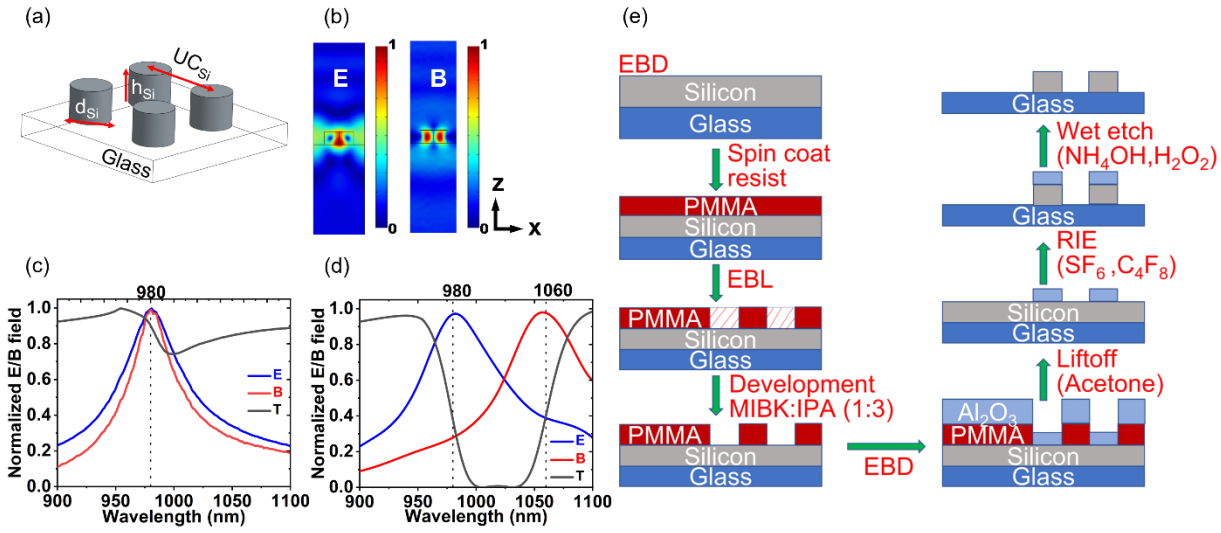

Figure 2.1: Design and fabrication of amorphous silicon Huygens metasurface

(a) Schematic of a portion of the dielectric nanoantenna array composed of amorphous silicon resonators on a glass substrate. The dimensions shown are: diameter (d_{Si} – 330 nm), height (h_{Si} – 190 nm), and unit cell periodicity (UC_{Si} – 581 nm). (b) Field profiles for electric field (E) and magnetic field (B) confinement in nanodisk meta-atoms at resonance. The field outside the nanodisk signifies nearest neighbor interaction in a periodic array. (c) Spectrally overlapping electric and magnetic dipole resonances are shown for a highly transmissive dielectric metasurface (d) Spectrally misaligned electric and magnetic dipole resonances are shown for a metasurface with a strong reflectance peak. (e) Schematic showing fabrication protocol for silicon nanodisk arrays (EBD – Electron beam deposition, EBL – Electron beam lithography, RIE – Reactive ion etching, PMMA – Polymethyl methacrylate, Al_2O_3 – Aluminum oxide, SF_6 – Sulfur hexafluoride, C_4F_8 – Octafluorocyclobutane, NH_4OH – Ammonium hydroxide, H_2O_2 – Hydrogen peroxide).

2.3 – Metasurface Design

The metasurface-based chip measurement setup is illuminated with light impinging at normal incidence on the chip in the presence of an encapsulating fluid (**Figure 2.2a**) which is varied to demonstrate the sensing capabilities of the chip. This metasurface is designed using finite element modeling (COMSOL Multiphysics) to predict the optical response of the chip before fabrication. A strong reflectance peak is obtained when the electric and magnetic dipole resonances are spectrally separated by 80 nm (**Figure 2.2b**). Device sensitivity can be defined in multiple ways as established in a previous work[39]. Here, we use the definition of sensitivity as the T/RIU - change in transmittance (T) per change in one refractive index unit (RIU).

A single wavelength laser passes through three metasurfaces and one reference (no metasurface) channel, and the corresponding transmission is measured by a four-quadrant photodetector. This merging approach may use three of the same metasurface for improved data averaging and fidelity. Or, taking advantage of the responsiveness of our Huygens metasurface platform to geometric changes, the sensor may utilize three different metasurfaces designs. Multiple simultaneous measurements on the same chip with different metasurface designs demonstrate the versatility of our sensing method as, for example, it enables us to measure fluid samples over a wider refractive index range than is possible with a single metasurface. In this work, we design and make three Mie-resonance metasurfaces on a single chip. As reported in a previous work, this type of metasurface demonstrates an experimental sensitivity and figure of merit (FOM) of 323 $nmRIU^{-1}$ and 5.4 respectively[40]. Each of these three metasurfaces is designed to have the same resonant behavior yielding a peak sensitivity of 5.8 T/RIU (**Figure 2.2c**) and an FOM of 2.1 (**Figure 2.2b**). We also design and make two different metasurfaces in three channel slots – one channel for the Mie resonance metasurface and the other two channels for the asymmetric resonance nanocylinder arrays. This results in a strong and more sensitive device thus obtaining a sensitivity of 20 T/RIU for the asymmetric resonance metasurface (**Figure 2.2d**) and an FOM of 11.1 (see **Figure 2.3c**).

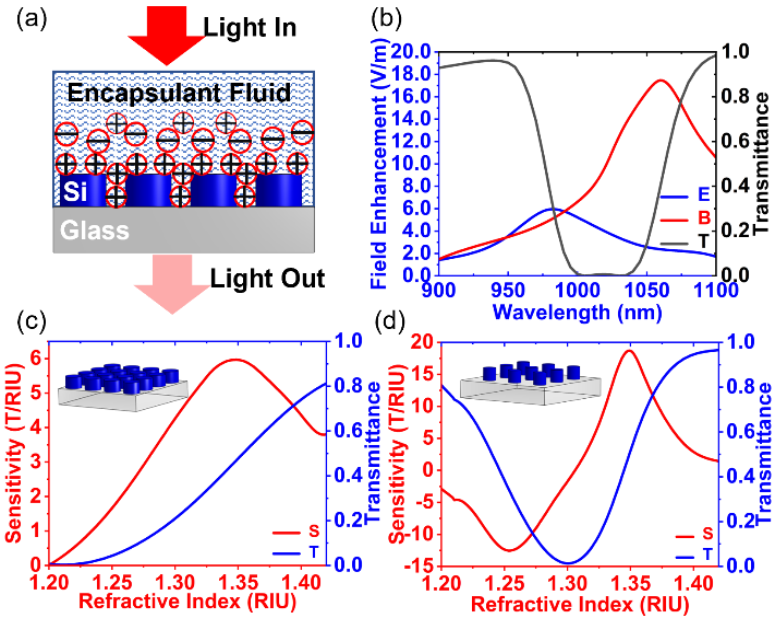

Figure 2.2: Field confinement and modeled sensitivities

(a) Schematic showing encapsulant fluid, nanoantenna, and substrate domains. Light is incident from the top, interacts with the molecules of the fluid creating an electric double layer and the optically induced response is transmitted through the glass and collected on a detector. (b) The resulting reflectance peak (black) from spectrally shifting electric (red) and magnetic (blue) fields. Field enhancement is calculated as the amount by which the electric and magnetic field is enhanced due to the presence of the silicon metasurface relative to no metasurface. (c) Metasurface design one: Mie-resonance nanodisks with maximum sensitivity of 5.8 T/RIU and d) Metasurface design two: Asymmetric resonance nanocylinders with maximum sensitivity of 20 T/RIU.

2.3.1 – Metasurface Resonance Sensitivity

The Huygens metasurfaces used in this work are distinguished by the type of resonances they excite. In the Mie resonance metasurfaces, the electric dipole resonance is more sensitive to changes in the encapsulant fluid refractive index compared to the magnetic dipole resonance (**Figure 2.3a**). In the asymmetric resonance metasurfaces, the magnetic field and electric field resonances shift at nearly equal rates as seen in **Figure 2.3b**. These dual resonance designs lead to enhanced sensitivity of the metasurfaces due to the contribution of multiple resonances. Other methods for improving metasurface sensitivity involves using higher quality factor resonances which in turn improves the FOM of the metasurface. Some proof-of-concept demonstrations of

this include antisymmetric resonances with light impinging at off-normal incidence[40], guided mode resonances[41], and bound states in a continuum (BIC) resonances[42].

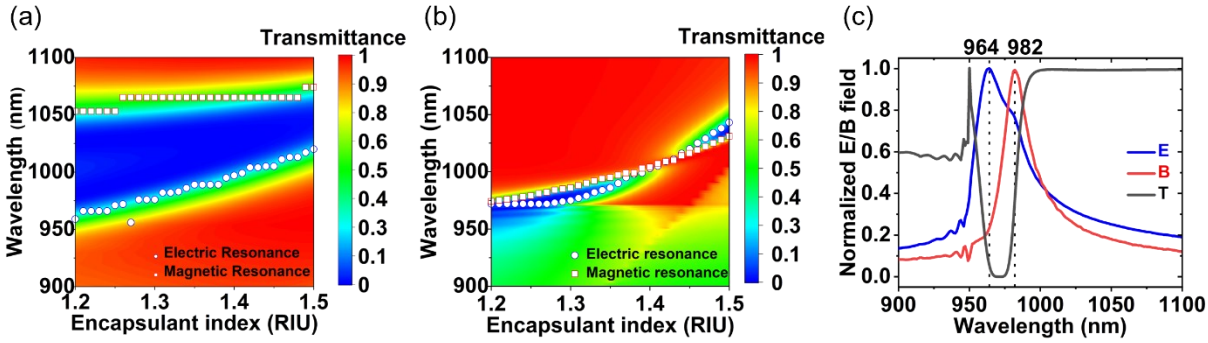

Figure 2.3: Metasurface resonance sensitivity to refractive index change

(a). Metasurface transmittance (color map) as a function of incident wavelength and encapsulant refractive index showing that the electric field resonance (blue circles) is more sensitive to changes in the encapsulant index than the magnetic field resonance (red squares) (b). Resonance shifts from varying encapsulant fluid refractive index for asymmetric resonance metasurfaces. (c). Electric and magnetic field amplitude vs. incident light wavelength at a fixed encapsulant fluid index (R.I. = 1.333) showing electric field and magnetic field asymmetric resonances at 964 nm and 982 nm respectively.

2.4 – Sensor Design

Taking advantage of resonant metasurfaces with a distinct spectral reflectance peak allows for highly sensitive single wavelength measurements using inexpensive optics. The use of a small data logger and a proportional-integral-derivative (PID) temperature controller to reduce the size and cost of computational equipment enables a highly competitive refractive index sensor at a fraction of the cost. The produced system is a result of integrating the metasurfaces into a microfluidic chip that is interrogated by a simplified optical system. The full system diagram showing all inputs, outputs, and subfunctions is given in **Figure 2.4**. The sample fluid is injected through exterior tubing before passing through the microfluidic measurement chip and then out of the sensor. These three systems (microfluidic, optical, and electrical) come together within a single

integrated housing and produce output voltage data that corresponds to relative transmittance, an indicator for refractive index change.

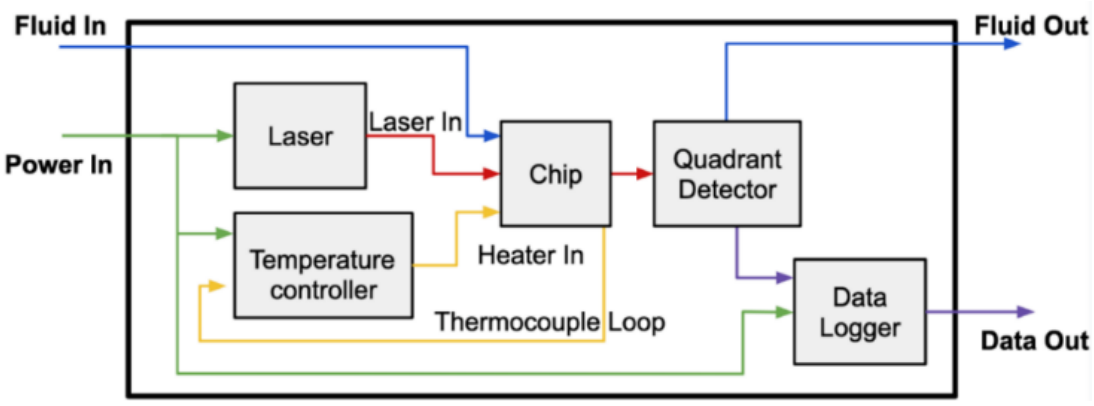

Figure 2.4: Nanophotonic microfluidic sensor block diagram

The blue path is the sample fluid stream, the green path is electrical power, the red path is the laser light stream, the yellow path is the heater loop, and the purple path is data output.

2.5 – Microfluidic Design

Microfluidic channels facilitate changing the metasurfaces' encapsulating layer, and therefore, the resonant response of the metasurfaces[43]. The inlet path length of the microfluidic channel is maximized before entering the measurement stage to allow the fluid temperature to equilibrate with that of the surrounding glass and PDMS (**Figure 2.5a**). Sample fluid then passes over a microfabricated reflectance mask (**Figure 2.5b**), designed to split a single incident beam into four: three metasurface sample beams and one reference beam where no metasurface is present. The reflectance mask is also intended to prevent the impinging beam from reaching the photodetector without first passing through the metasurfaces. This design allows up to three separately tuned metasurfaces and a reference measurement to be taken simultaneously, accounting for noise in the measured signal due to fluctuations in ambient temperature, liquid

pressure, and the intensity or wavelength of the laser. **Figure 2.5c** shows a fabricated metasurface measurement chip with microfluidic channels.

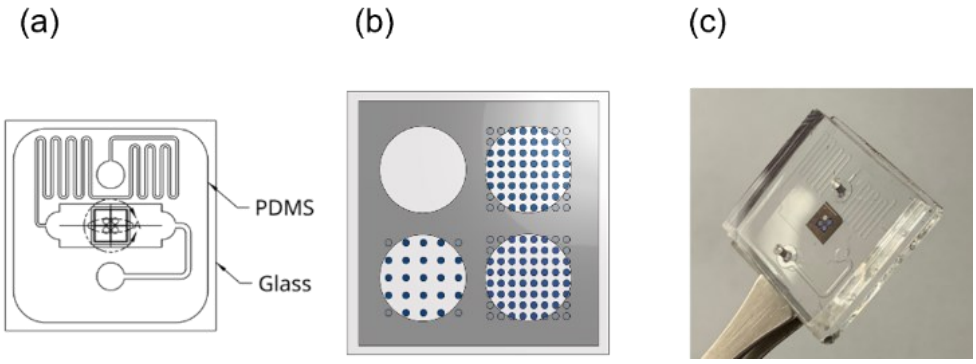

Figure 2.5: PDMS stamp design and microfabrication

(a) Microfluidic diagram showing fluid inlet (top circle), temperature stabilization channel, the main testing channel with the optically active area, and a fluid outlet (bottom circle). Fabrication processes are included in Appendix B. (b) Diagram showing three different metasurfaces and a reference channel with overlaid reflectance mask. (c) Sensing chip showing three 500-micron square metasurfaces and a blank reference within a chromium reflectance mask.

These are fabricated on a microscope glass slide and bound within a PDMS microfluidic channel. Fluid inlet and outlets are shown above and below the chromium mask, respectively.

2.6 – Electro-optics Design and Prototyping

All metasurface dimensions are designed for maximum T/RIU at a wavelength of 980 nm, so that the sensor can employ affordable, off-the-shelf parts. A Thorlabs L980P010 Laser Diode is chosen as the light source, which is collimated and incident upon the microfluidic measurement chip. This diode was characterized using the Ocean Optics NIRQuest Spectrometer to verify an operating wavelength of 980 nm. The outgoing light beams are then collected by a First Sensor QP5.8-6-TO5 Quadrant Photodiode, containing four distinct active areas corresponding to each beam. The optical train is shown schematically in **Figure 2.6a**. All optics are aligned and positioned with standard Thorlabs dovetail rails, mounts, and posts (see **Figure 2.6b**). The voltages for each

active area are logged in a Delphin Loggito USB Data Logger using the included Profilog software package for analysis.

All electronic components within the sensor are powered through a 24 V (DC) wall adapter that connects to the housing on the backside of the enclosure. 24 V is passed to an Omega CND3 PID Controller for temperature regulation, and in parallel the voltage is stepped down through a series of cascading voltage regulators to meet the power requirements of a Thorlabs LD1100 Constant Power Laser Diode Driver (see circuit diagram in **Figure 8.1**). The PID controller regulates the measurement chip temperature to within ±1°C based on feedback from a K-type thermocouple. This is accomplished using a ceramic heater modulated by a relay switch (see **Figure 8.1**) placed underneath the glass substrate of the measurement chip; the heater has a 4.0 mm diameter hole in the center to pass the transmitted light to the quadrant photodetector.

Temperature control is critical to minimize noise-based uncertainty in measurement resolution, for example maintaining the metasurface and reference channels at the same temperature during measurements.

A custom housing (L=8.5", W=6.5", H=4") containing all required equipment developed for this sensor testbed was manufactured by Protocase, to prevent ambient light from interfering with measurements and to promote portability (**Figure 2.6c**). Vibration-damping feet on the bottom of the enclosure reduce exterior mechanical noise. Cutouts are included for the through-wall PID temperature controller, power supply inlet, and USB connector for data output. In addition to a removable cover, a hinged door provides access to the measurement stage for optical alignment and quick measurement chip replacement. The microfluidic/metasurface measurement chip itself is precisely positioned via a small manual two-axis micrometer stage to ensure proper alignment. The inlet and outlet ports for the sample liquid are syringe-compatible and are affixed close to the

laser path to minimize required sample volumes. An external container collects the output fluid on completion of testing.

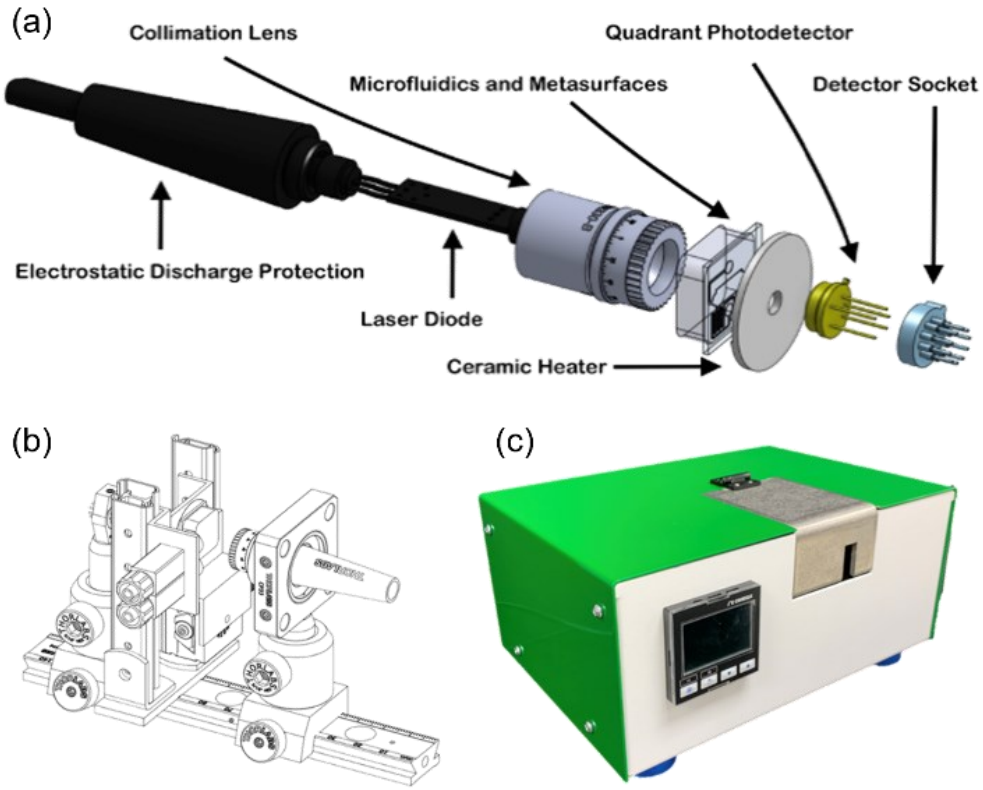

Figure 2.6: Refractive index sensor housing

(a) Exploded view of the optical train aligned to the metasurface-based measurement chip. (b) Schematic of the optical system and microfluidic chip stage with mounting and alignment components. (c) Image of the fully functional, portable sensor.

2.7 – Experimental Methodology

For solution refractive index and composition measurements, demonstrations are done using saline at varying concentrations. The sample fluid is introduced to the microfluidic chip by

a syringe via the inlet tubing. The measurement is taken while the solution is at rest within the channel to ensure there is no fluctuation introduced by flow-induced pressure changes. The sample fluid then passes through the outlet tubing and a pocket of air is introduced to flush out any remaining fluid. The channel is cleaned with deionized water to remove any residue left in the channel. De-ionized water is measured first as the zero-concentration baseline to which all changes in transmittance (ΔT) values are referenced. Photodetector voltage data is collected over a period of two minutes. The reference (no-metasurface channel) beam is used to normalize into transmittance using equation 2.1 below.

$$T_s = \frac{V_{meta}}{V_r} \qquad (2.1)$$

here T_s is relative transmittance, V_{meta} is the photodetector voltage output from the metasurface incident beam, and V_r is the reference beam voltage. The resultant transmittance values are relative and not absolute, and thus the quantity of interest in finding refractive index is not transmittance, but a normalized change in transmittance from the zero-concentration solution.

At lower concentrations, the sodium cations (Na^+) in solution are preferentially adsorbed to the surface terminating hydroxyl anion (OH^-) bond on the silicon surface. This explains the relatively significant change in the sensor's optical response for very small changes in refractive index due to the changing effective encapsulant refractive index surrounding the metasurfaces. This surface adsorption phenomenon results in a nonlinear relationship between the transmitted signal and saline concentration and enables sensor performance with lower detection limit. This nonlinear behavior occurs for concentrations of saline below 10^{-2} M. The surface adsorption feature, illustrated in **Figure *2.2*a**, is in agreement with electrical double layer theory where co-ions are repelled, and counter-ions are attracted to a charged surface[44,45].

When higher saline concentrations flow through the sensor, the sites available for surface adsorption become quickly saturated. The influence of bulk encapsulant refractive index changes begin to dominate resulting in a linear trend. The following equation is then used to convert ΔT values into refractive index measurements for a linear system:

$$\mathrm{RI} = \frac{\mathrm{T_S} - \mathrm{T_0}}{\mathrm{S}} + \mathrm{RI_0} \qquad (2.2)$$

Here, RI is the refractive index of the sample solution, T_0 is the same relative transmittance calculation (Equation 1) but for a zero saline concentration solution, S is bulk metasurface sensitivity in units T/RIU, and RI_0 is the refractive index value of the zero-concentration base solution. Equation 2.2 is used to calculate the linear sensitivity (S) of the sensor. A known empirical relation for saline's refractive index change with concentration and temperature is used to set the RI_0 and RI values for the bounds of the measured range[46,47]. With this information, by rearranging the terms in equation 2, S can be solved for and used to find RI for all intermediate values in the linear operating range.

Detection of biomarkers of interest, such as those associated with infectious diseases, may be accomplished with the same sensor by utilizing a biochemical assay to perform functionalized surface sensing as opposed to the bulk fluid sensing discussed before. The assay procedure ensures selectivity through antibody-antigen interactions, where the antibodies are bound to the surface-functionalized metasurface as a capture site and antigens from the sample solution attach during the measurement phase. Sensor optical measurements are taken at each step of the assay to track the change in transmission caused by each component. The complete assay can be seen in **Figure 2.8(a)-(e)** with further details given in the Appendix B[48–53].

2.8 – Sensor Performance

Figure 2.7a and **b** show measured optical response data collected for saline solutions with varying concentrations. Results indicate a .9849 R^2 linear fit for an experimental standard curve consisting of 11 points (excluding water) representing saline concentrations varying from 18.9 mM to 150 mM. We define the sensor limit of detection (LOD) in two ways. First, the concentration LOD (LOD_{conc}) describes the smallest concentration of solution below which the sensor can detect no change in optical response. Also, the refractive index LOD (LOD_{RI}) represents the smallest change in effective encapsulant refractive index that can be detected by our sensor because of solute concentration change from one fluid to another. From system noise (see **Table 2.2.2**) we expect to see a theoretical LOD_{RI} of about 1 x 10^{-6} RIU as limited by the data logger resolution and our current level of noise control. Here, we demonstrate a measured LOD_{conc} of 7.3 x 10^{-5} M (4,272.8 $ngmL^{-1}$) corresponding to an LOD_{RI} of 1.9 x 10^{-6} RIU using the aforementioned empirical relation. The obtained LOD is compared with state-of-the-art dielectric-based photonic sensors in **Error! Reference source not found.**. **Figure 2.6c** shows the data on a log plot, i llustrating the LOD for this sensor's bulk refractive index measurements.

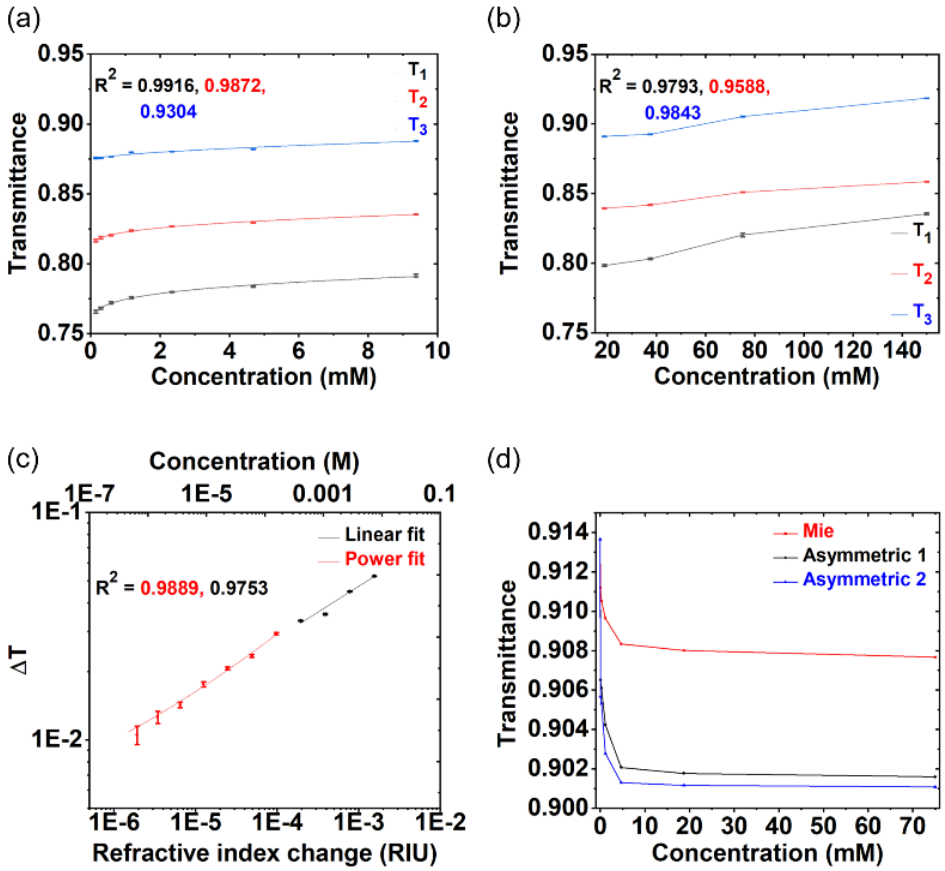

Figure 2.7: ***Refractive index sensor performance for bulk fluids***

Transmittance vs. concentration measurements for three similar metasurfaces with saline solutions showing a similar repeatable trend across the three metasurfaces for (a) low saline concentrations (<~10^{-2} M) and (b) high saline concentrations (> ~10^{-2} M). (c) LOD plot for one Mie dipole resonance metasurface for a broad range of saline concentrations. ΔT represents relative transmittance change. (d) Transmittance vs. saline concentration for one Mie dipole resonance and two asymmetric resonance metasurfaces measured on the same chip. Red is the Mie nanodisk array; the other two are nanocylinder arrays with different lateral dimensions supporting asymmetric resonances.

Sensor Type	Interferometer-based	Photonic Crystals	Bloch Surface Waves	Photonic Crystal Cavity	Whispering Gallery Mode	Dielectric Nanodisks (this work)
LOD [RIU]	1.8×10^{-6} [31]	1.97×10^{-6} [54]	3.8×10^{-6} [55]	7.8×10^{-6} [56]	4.5×10^{-6} [57]	1.9×10^{-6}

Table 2.1: Dielectric-based photonic sensor types and their limits of detection[a]

[a]The low-cost dielectric metasurface-based sensor demonstrated here has a LOD comparable to these state-of-the-art refractive index sensors.

The device design approach (three metasurface slots and one reference channel slot measured simultaneously) enables the measurement of three similar or three different metasurfaces at a time. Testing three similar metasurfaces serves to enhance measurement fidelity and assess reproducibility, whereas a chip with different metasurfaces expands the range of testable fluid refractive indices and increases system measurement flexibility. This can be seen in **Figure 2.7d** where we show an increasing sensitivity for the low concentration region for bulk saline solutions when measured with asymmetric resonance metasurfaces vs. Mie resonance metasurfaces. Furthermore, optical transmittance decreases with increasing saline concentration, showing a different trend from our earlier measured metasurface results in **Figure 2.7a**. This can be attributed to a mismatch between fabricated geometries and modeled geometries, where the transmission band has red shifted such that these measurements are happening at a different spectral location relative to that transmission band, with opposite change in transmittance vs. concentration.

System noise is a limiting factor in achieving a competitive LOD. Refractive index is dependent upon temperature[58] and pressure[59]. As shown in **Table 2.2.2**, we have demonstrated control over these two parameters to measure refractive index changes (Δn) on the order of 10^{-4} RIU without continuously averaging to reduce environmental perturbation effects. Taking advantage of simultaneous referencing eliminates the impact of drift from temperature, pressure, and even incident power and wavelength fluctuations. Vibrational noise is more difficult to

characterize and mechanically stabilize in a portable sensor but utilizing a rolling average along with a reference channel that experiences the same mechanically induced fluctuation has proven effective enough to allow for refractive index changes to be detectable down to ~10^{-6} RIU. The main factor that limits the achievement of lower LOD is the cost of higher precision data loggers, which we avoid maintaining competitive sensor total cost. A lower noise limit exists due to the resolution of the Delphin Loggito USB Logger used for data collection of voltage signals at .01% of the range. In our case, the maximum signal is ~0.250 V, leading to a $2.5*10^{-5}$ V resolution before averaging or normalization.

Noise Analysis	**Metric**	**Current Possibilities (Δn)**	**Control needed ($\Delta n \sim 10^{-4}$)**	**Control needed ($\Delta n \sim 10^{-6}$)**	**Control needed ($\Delta n \sim 10^{-8}$)**
Detector/Power	**~3.7 x 10^{-14} RIU·mW^{-1}**	**~ 10^{-8}**	**10^{10} mW**	**2.7 x 10^{7} mW**	**10^{6} mW**
Vibrational	**~2.9 x 10^{-3} RIU·nm^{-1}**	**~10^{-4}**	**3.5 x 10^{-2} nm**	**3.5 x 10^{-4} nm**	**3.5 x 10^{-6} nm**
Temperature	**10^{-4} RIU·^{o}C^{-1}**	**~10^{-5}**	**1^{o}C**	**10^{-2} ^{o}C**	**10^{-4} ^{o}C**
Pressure	**10^{-5} RIU·atm^{-1}**	**~10^{-8}**	**10 atm**	**10^{-1} atm**	**10^{-3} atm**
Wavelength	**10^{-5} RIU·nm^{-1}**	**~10^{-6}**	**10 nm**	**10^{-1} nm**	**10^{-3} nm**
Data Logger	**5 digits for 10^{-6}**	**~10^{-6}**	**3 digits**	**5 digits**	**7 digits**

Table 2.2: Noise Analysis Table Defining Metrics Needed to Achieve Acceptable Control at Three Different Sensitivity Levels: 10^{-4} Δn, 10^{-6} Δn, and 10^{-8} Δn[b].

[b]*With our current level of control of each of these factors, sensitivity of $\Delta n \sim 10^{-4}$ can be achieved with simultaneously referenced data. Referencing and data averaging are needed to attain $\Delta n \sim 10^{-6}$. Achieving temperature control and data logger precision to obtain $\Delta n \sim 10^{-8}$ is currently beyond the scope of our sensor.*

A complete bill of materials, as given in Appendix B, places our current sensor cost for one unit at $3,994. In comparison to equally sensitive technologies, our price point per unit is 87% - 96% lower[40]. This is possible due to the simplicity of the required equipment for the sensor described here as compared to other established methods[60]. Implementing more accurate controls

and data acquisition would decrease the current LOD while increasing sensor cost. This could also be done through incorporation of a microcontroller and simple display to directly output data from the device.

We use the bioassay described in the experimental section to measure a wide range of concentrations of the TB antigen CFP-10 (one of the top two biomarkers for detecting TB)[61] in a Phosphate Buffer Solution (PBS). The metasurface-based sensor produces the results seen in **Figure 2.8f** and **Figure 2.8g**. Specifically, we are interested in identifying the dynamic range, the LOD, and the sensitivity of this CFP-10 peptide measurement. The dynamic range is the measured region of concentrations where we can identify distinct changes in transmittance. In our current data set, we measure a dynamic range of 11 orders of magnitude, spanning from 1 pM (1.6 $pgmL^{-1}$) to 10 mM (16.0 $mgmL^{-1}$) We use the standard IC_{10} metric that sets the LOD as 10% saturation of the dynamic range[25]. This places our LOD at 10 pM which corresponds to 16.0 $pgmL^{-1}$. This indicates that the obtained LOD value is several orders of magnitude more sensitive compared to standard ELISA measurements.[62] Similarly, we denote the sensitivity as the IC_{50} value, or 50% saturation of the dynamic range[25]. On our standard curve, this equates to 0.1 μM (160.3 $ngmL^{-1}$). This proof-of-concept demonstration is for CFP-10 suspended in a homogeneous PBS solution, and performance will certainly change with samples spiked in commercialized human serum and clinical samples[61]. However, with future improvements in sample filtration[63,64], optimization of antibody-antigen pairing[65], and recycling steps, this sensor is expected to show similar functionality for more complex human samples.

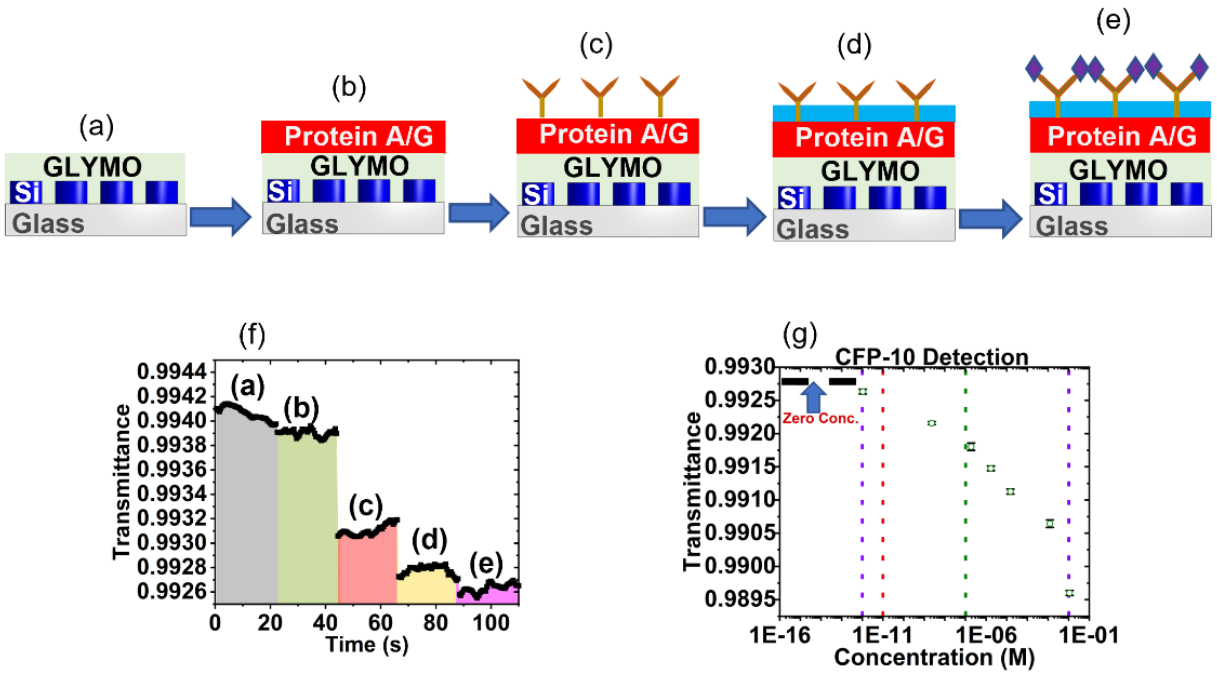

Figure 2.8: Functionalized metasurface platform

(a) Silicon metasurfaces on a glass substrate with GLYMO added to bind proteins to Si and SiO_2; (b) Protein A/G is added, which enhances the binding affinity of human IgG (the capture antibody); (c) The "Y-shaped" structures are capture antibodies (anti-CFP-10 antibody) that serve as antigen-binding sites; (d) The blue layer represents a blocking buffer which reduces the noise introduced by unspecific binding; and (e) The purple rhombuses represent CFP-10 peptide in the sample that have bound to the measurement chip. (f) Sensor transmittance vs time highlighting the data collection time frame for each layer added to the metasurface chip according to Figures 7(a)–(e), with CFP-10 concentration of 1.06 pM (1.7 $pgmL^{-1}$) measured in this figure. Temperature fluctuation effects during measurement are nullified by post-measurement averaging. (g) Sensor transmittance versus CFP-10 peptide concentration after averaging. Here we identify the dynamic range as 1 pm-10 mM (purple dashed lines), the LOD (IC_{10}) as 10 pM (red dashed line), and the sensitivity (IC_{50}) as 0.1 μM (blue dashed line). Zero antigen concentration is represented by the black horizontal dashed line in the low concentration region of the plot.

2.9 – Conclusions and Future Outlook

To sum up, we have developed and characterized a compact and portable metasurface-based refractive index sensor applicable for bulk and surface detection. Final prototype cost represents an 87% - 96% cost reduction over existing detection methods offering comparable sensitivity. The measured LOD for bulk fluid refractive index measurements of $1.9*10^{-6}$ RIU rivals state-of-the-art dielectric-based photonic refractive index measurement devices. Metasurface full

wave model results have been replicated experimentally to verify nanoantenna array functionality. Biomolecule surface detection is demonstrated for the CFP-10 peptide, a tuberculosis biomarker. We measure an IC_{50} maximum sensitivity of 0.1 μM and an IC_{10} detection limit of 10 pM. The entire sensor described here may be further integrated into a photonic chip, making it deployable in smart phones and handheld devices to aid with preventative diagnostics and clinical monitoring. Although this platform was designed and fabricated to operate in the near infrared regime, similar Huygens nanodisk arrays can be employed for portable sensors in the visible regime using a different material platform.[66] By incorporating a more precise data logger and signal averaging, the limit of detection for this sensor could be further improved by two orders of magnitude at an additional cost less than 50% of the current overall assembly cost. Ultimately, this platform shows promise for further improvements in sensitivity, cost, and size reduction, for applications in industrial process monitoring, infectious disease diagnostics, trace gas detection, and more.

Further developments of this sensor could lead to enhanced device functionality with better performance. This could allow for multiple metasurfaces based on different optical resonant phenomena to be fabricated on one chip for multiple simultaneous measurements. Although this was achieved in this work for bulk fluid samples, it could be significant for biofluid measurements. This, in addition with a highly precise readout system, could be useful to determine the fundamentally constrained detection limit of a single biomarker by making simultaneous measurements. This can be explored by using resonances of different quality factors ranging from low quality factor Mie resonances to high quality factor guided mode resonances or asymmetric resonances. Using resonant metasurfaces with different sensitivities, we can study how the photon-matter interactions in these optical systems are affected by binding kinetics of a single biomarker

of interest, revealing the underlying physics of how different resonance types affect the limit of detection.

Furthermore, a sensor chip with multiple nanoantenna arrays could be useful for measuring multiple biomarkers simultaneously. This could really extend the applicability of the device towards point-of-care diagnostics. One challenge to overcome when making this could be to eliminate cross talk between biomarkers in different channels. One way to surmount this would be to use microfluidic channel filtering where microfluidic channel widths are custom made to fit the diameter of the biomarker molecule. This would ensure that each microfluidic channel accepts the biomarker that fits its width while rejecting larger biomolecules. The setup could be achieved by illuminating multiple channels with individual beams. Each beam may be guided into each channel using some micromirror arrays or other guiding optics. This could be utilized to detect multiple varying biomarkers simultaneously at the cost of a larger footprint device. Another way could be using different antibodies for different biomarkers. This could also prove useful for studying the specificity of the system, which is a critical parameter for functional biosensors.

To enhance performance, it is important that this sensor is capable of quantifying binding kinetics of biomarkers in biofluids and surface molecule interactions in bulk fluids. The Langmuir model may be used for understanding molecule binding interactions, from which the association and dissociation rate constants can be determined[67]. The association constant can be calculated using the law of mass action which states that at equilibrium, the ratio between the concentrations of the products (complex) and the reactants (antigen and antibody) is a constant term, K_{eq} which is the equilibrium constant. This constant is the association equilibrium constant and is equal to the ratio of the association rate to the dissociation rate. The dissociation equilibrium constant is the multiplicative inverse of the association constant. The concentration of antigen, antibody, and

complex could be determined at equilibrium outside the device from which the association equilibrium constant may be determined[68].

Chapter 3 – Continuously Tunable Amplitude and Phase Modulation with Vanadium Dioxide Metasurfaces

3.1 – Chapter Overview

In the preceding chapter, we showed how we can achieve optical tunability by altering the encapsulant material on the metasurface. Dynamic control of the optical beam properties can also be achieved by refractive index tuning of the substrate or nanoantenna material itself through various external stimuli such as mechanical deformation, free carrier effect, thermo-optic effect, and the use of phase change materials. This can result in efficient light manipulation at optical frequencies which is highly desirable for many photonics applications. Active optical metasurfaces represent a useful way of achieving this due to their smaller footprint and low power consumption paving a way toward the realization of chip-scale photonic devices with desired optical functionality on demand. Here, we show a dynamically tunable dual-function metasurface based on dielectric resonances, capable of independent active amplitude and phase control without the use of mechanical parts. Gradual thermal control of the metasurface yields a continuously tuned amplitude modulation of 19 dB with negligible phase modulation and a continuously tuned phase modulation of 228^{o} with negligible amplitude modulation. Reprogrammable optical functionality can thus be achieved using precisely engineered nanoantenna arrays for adaptive modulation of

amplitude and phase of light for exciting applications such as tunable holograms, lenses, and beam deflectors.

3.2 – Introduction

The need for manipulation of light at very small dimensions is important for the design and production of next-generation integrated photonic devices. Traditional optical elements like lenses and holograms are bulky and rely on relatively long-distance (mm to cm) variation of amplitude, phase, wavenumber, and/or polarization along the path that the light wave traverses. These bulky devices need error-free shaping and molding techniques to direct the impinging optical wave efficiently, leading to a high cost of production.[69] Due to rapid developments in micro-and nanoscale photonics in the 21st century, there has arisen an inevitable need for the design and fabrication of small-scale optical components for easy integration in next-generation devices.

Over the last decade, research has resulted in the emergence of a diverse class of structures called optical metasurfaces. Metasurfaces are subwavelength structures with the ability to impart a sudden change to the amplitude, phase, polarization, and/or wavevector of optical waves at the interface between two media (over distances of nm to μm). They can be made from metallic or dielectric materials and are engineered to yield a desired optical function such as flat lenses,[70–72] holograms,[73–75]and biosensors.[25,33,76] These metasurfaces can be designed to scatter light in the desired direction by taking advantage of their material properties as well as their geometry. Dielectric materials are preferred over their plasmonic counterparts because of their low energy dissipation. They can also be designed to spatially confine light, resulting in electric and magnetic Mie resonance behavior which allows for full control of the optical properties of light[9].

Although these metasurfaces have demonstrated excellent properties and performance, in some cases surpassing their traditional bulky counterparts, most of them are passive, with functionality stored in the resonators that cannot be altered after fabrication. The development of active metasurfaces whose performance can be altered after fabrication is highly desirable, with far-reaching applications in vari-focal lensing, dynamic holography, optical communications, and more. Dynamic tuning can be achieved through many methods, including tuning the nanoantenna array by some external stimulus such as temperature, electric bias, and optical pumping. Other methods of tunability include tuning the nanoantenna size, spacing and/or shape by mechanical distortion to the nanoantenna substrate or surrounding material[40,77]. Finally, the nanoantenna material itself may be tuned by using phase change materials (PCMs) or free carrier effects[78,79].

PCMs have particularly shown significance in paving the way for active modulation of optical properties. They can either be non-volatile or volatile. Non-volatile PCMs, such as GeSbTe (GST) and Sb_2S_3, undergo a binary phase change from one state to another with external stimulus. This phase change endures when the initial stimulus is removed, and the material does not undergo a reverse phase change without the input of an additional external stimulus. Non-volatile PCMs are good candidates for memory materials and programmable photonics[80,81]. On the other hand, volatile PCMs like vanadium dioxide (VO_2) reversibly change their phase naturally when the initial stimulus is removed. This volatile transition enables the potential for rapid and/or continuous modulation of optical properties. Vanadium dioxide atoms go through a structural rearrangement from their monoclinic structure in the insulating phase to a tetragonal rutile structure in the metallic phase at a temperature of ~ 68^0C. The transition has been demonstrated to be switchable on sub-picosecond time scales[82]. If the material is inhomogenous, as is often the case, then the transition can result in a gradual modulation from one state to the other over a range

of stimuli (e.g. 65 to 74 °C). The volatile nature of VO_2 has resulted in the use of this material for thermal regulation and tunable waveguides in the near-infrared regime. VO_2-based integrated photonic devices have also been demonstrated for optical memory applications[83,84].

VO_2 can also be deployed for nanoscale manipulation of the optical properties of light as a tunable layer or a tunable structured material. When used as a tunable layer, it provides dynamic reconfigurability to an adjacent nanostructure. Examples include tunable reflectarray modulators,[85] tunable metasurface absorbers, and more.[86,87] Using VO_2 as a tunable layer in a multilayer metasurface could pose fabrication challenges and lead to less optical field confinement in VO_2, resulting in unoptimized metasurface performance. When VO_2 is used as the nanostructured material for the metasurface, greater optical confinement in the metasurface can be achieved. For example, Bukatov et al., illustrated a dual plasmonic to dielectric resonant behavior using VO_2 thin films, wire arrays, and disk arrays at near-infrared wavelengths[88]. Also, Kepič et al., showed optical tunability of VO_2 nanodisks in the visible[89]. Each of these groups could demonstrate some amplitude modulation of the fabricated disks but did not show continuously tunable phase modulation. Dynamic amplitude modulaton is useful for thermally switching applications like active amplitude modulators however, it is highly profitable to achieve incessant amplitude and phase modulation using the same metasurface design.

In this work, VO_2 is used as the nanoantenna material in the design of dielectric Huygens metasurfaces, which are known for their spectrally overlapping electric and magnetic dipole Mie resonances in carefully structured dielectric materials[90]. **Figure 3.1** shows a 2 x 2 array representing a section of VO_2 Huygens metasurfaces with labeled domains.

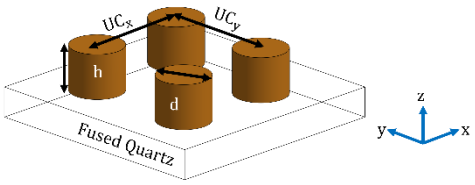

Figure 3.1: Schematic of section of Huygens nanoantenna array

UC_x and UC_y stand for unit cell dimensions in x and y axes respectively. h_{VO2} is the height and d is the diameter of the nanoantenna element.

Although VO_2 has a high refractive index modulation between its insulating and metallic phase, it is significantly lossy (k > 0.2) over a large range of the visible (400 to 700 nm) and near-infrared spectrum (800 to 1870 nm) in its insulating phase and over a much wider wavelength range in its metallic phase. This makes it challenging to achieve good optical modulation in nanophotonic designs in that region due to its highly absorbing nature over this range. To harness the intrinsic tunability of refractive index in VO_2 with high performance, resonant metasurface designs are made in the near-zero loss region (1960 to 2050 nm) for the insulating phase. In this work, we focus on the design of Huygens metasurfaces which support spectrally overlapping electric and magnetic dipole Mie resonances, thereby enhancing forward scattering. The presence of overlapping dipole resonances at higher wavelengths yields higher-order resonant modes at lower wavelengths, which we also take advantage of, and allows for multiplexed optical modulation in a single switchable nanophotonic device.

3.3 – VO_2 Metasurface Design

Huygens metasurfaces supporting overlapping electric and magnetic dipole resonances can be achieved using a broad design space. For this work, the optimal design selected should yield

the largest continuous amplitude or phase modulation at individual wavelengths with little or no residual change in the other property. That is, if the amplitude (phase) is tuned continuously, there is little or no phase (amplitude) change. Resonant nanostructures permit decoupling the modulation of individual optical properties and so outperform non-resonant thin films, whose performance is based on propagation. Resonant metasurfaces are a better choice for approaching the fundamental limit of optical performance for modulators.[91]

In pursuit of an easily fabricable VO_2 metasurface with the best optical performance, we swept across a broad design space. These metasurfaces are designed with COMSOL Multiphysics software, which uses the finite element method for obtaining the optical performance of the design. Periodic boundary conditions are applied to the model to simulate an infinitely extending nanoantenna array in two dimensions. To simulate dynamic optical manipulation, we adopted a tuning parameter, "TuneFrac", which represents a fractional variation in the optical properties (*n* and *k*) of VO_2 as we tune from its insulating to metallic phase. We use temperature dependent ellipsometry on our synthesized VO_2 thin films to extract the *n* and *k* data used for the simulations reported in this work, as shown in **Figure 3.4**. This is critical since the optical properties of as-grown VO_2 thin films depends on growth methods, post-growth treatments, and defect concentration[92]. shows schematics of the unit cell of different designs we use. Each nanoantenna geometry is simulated in a periodic array using fused silica as the substrate and PDMS as the encapsulant layer. The low index of the substrate and encapsulant domains yields a high refractive index contrast between the VO_2 nanoantenna and its surroundings, which enables high optical field confinement in the resonators. Also, selecting an encapsulant with optical properties similar to the substrate ensures refractive index matching, which is useful for highly transmissive optical devices. We first investigate an idealized VO_2 metasurface design where we have set the losses to

zero. Then we observe how the absorption increases when tuning from the insulator to the metal phase. We observe resonant-enhanced absorption across all the nanoantenna element designs investigated and a resonance decay as well as a redshift as it approaches the metallic phase; the hole array is an exception, where there is a blue shift. This resonance decay is comparable to a classical critically damped oscillator whose damping is increased due to resonance-amplified absorption[93]. To quantify the relative impact of this effect for each geometry, we show the resonant absorption after increasing the loss to $k = 0.1$. **Error! Reference source not found. 3.1** summarizes t he optimized performance of each design for both amplitude (ΔT) and phase ($\Delta\varphi$) modulation.

The nanodisk geometry is chosen for further study, as it gives the best combination of amplitude and phase modulation potential, in fact enabling us to fabricate a phase and amplitude modulator on the same chip. Other designs investigated have inclusions or voids created within them that lead to variation in spectral resonance intensity and location, thereby altering its modulating properties. The details of these design geometries are shown in Table 8.1.

	Nanodisks	Si disks in VO_2 film	Donut	Holes	Split ring & bar
Geometry	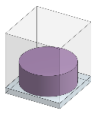	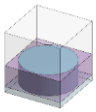	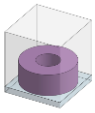	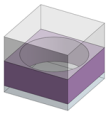	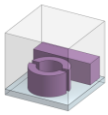
Resonant wavelength (no loss) (nm)	1980	2050	2000	2020	1960
Absorption at resonance (k=0.1)	96%	22%	68%	89%	67%
ΔT (dB)	-19.2 (1920 nm)	-13.9 (1800 nm)	-12.1 (2130 nm)	23.4 (1280 nm)	-15.1 (1890 nm)
$\Delta\varphi$ (deg.)	228 (1676 nm)	185 (1556 nm)	165 (1690 nm)	116.5 (1690 nm)	184 (1605 nm)

Table 3.1: Optical performance of various VO_2 Huygens metasurface designs

3.3.1 – VO_2 Nanodisk Metasurface Design

The disk geometry is carefully engineered to excite interfering magnetic and electric dipole resonances at 2020 nm. This wavelength is chosen because it lies in the low loss wavelength range where spectrally overlapping electric and magnetic dipole modes can be excited and yield useful performance. The dielectric nature of the VO_2 nanoantennas in their insulating phase allows for the excitation of multiple Mie resonant modes, increasing the degrees of freedom available for optical modulation.[38] We observe a strong higher-order magnetic mode at a shorter wavelength relative to the fundamental resonant wavelength of the metasurface where spectral overlap occurs; both are shown in **Figure 3.2a**. Using our tuning parameter, TuneFrac, the effects of decreasing refractive index and increasing absorption on both the amplitude and the phase of the impinging light wave in resonant and non-resonant regimes of the spectrum were investigated as shown in **Figure 3.2b** and **c**. **Figure 3.2d** shows the amplitude modulation at the resonant wavelength of spectral overlap between the electric and magnetic dipole modes. Amplitude modulation of ~11 dB is obtained at resonance with a negligible phase shift (~40^o). The intrinsic damping present in VO_2 is amplified at this wavelength precluding optimal amplitude modulation. For optimal amplitude modulation, we choose an off-resonant spectral location where we can minimize the effects of absorption enhancement as we tune from dielectric to metallic behavior. **Figure 3.2e** shows that at 1920 nm (off-resonant wavelength), we obtain a continuously tunable amplitude change of ~19 dB with a minimal phase shift (~35^o). This photonic device can be useful in variable optical attenuators and has the potential of replacing conventional variable optical attenuators which require mechanical parts for operation[94]. For phase modulation, we choose to operate in the vicinity (1676 nm) of the higher-order magnetic resonance, as this resonance yields a total

continuously tunable phase shift of 228° (**Figure 3.2f**) with little residual amplitude shift (~4 dB). The phase modulation without amplitude modulation obtained for this higher-order resonance mode suggests that absorption has minimal effect on this resonance. Using either stacking (transmission mode) or a mirror (reflection mode) to achieve >360° tunable phase shift, such a modulator could be engineered for use in low-loss, high-speed, and continuously reconfigurable optical wavefront shaping devices.

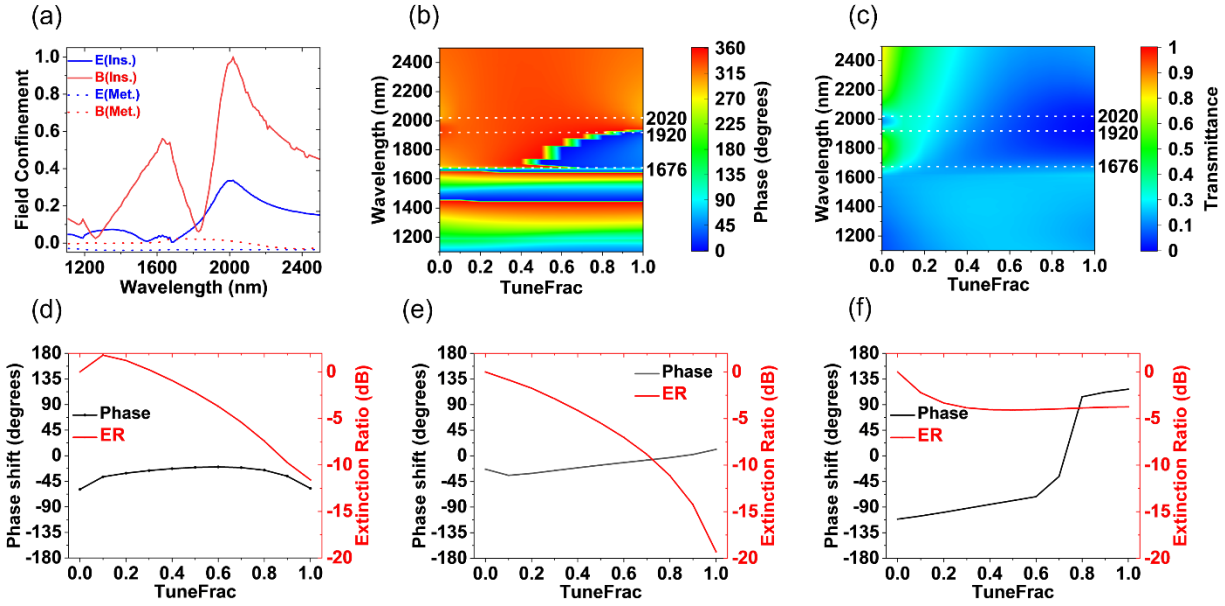

Figure 3.2: Tunable metasurface nanodisk array design

(a). Normalized field confinement at the center of the VO_2 nanodisks showing a spectral overlay of electric and magnetic dipole modes at 2020 nm and a higher-order magnetic resonance at 1630 nm. (b). Modeled continuously tunable optical phase spectrum and (c). Modeled continuously tunable transmittance spectrum from dielectric phase to metallic phase of VO_2. (d). Amplitude and phase modulation at spectrally overlapping dipole mode (2020 nm). (e). Amplitude and phase modulation along the slope of spectrally overlapping resonant modes showing large amplitude change (-19 dB) with little residual optical phase change (35°). (f). Amplitude and phase modulation around higher-order magnetic resonant mode (1676 nm) showing an optical phase tuning of 228° with little residual amplitude modulation (4 dB).

3.3.2 – Resonant plots for lossless and lossy VO_2 geometries (artificial loss set to 0.1)

Due to the lossy nature of VO_2, the absorptive response of the resonators is amplified at resonance like a damped oscillator. This loss is often accompanied by a red shift of the resonances as well as resonance decay for most of the geometries investigated as listed in **Error! Reference s ource not found.**. In the hole geometry, the resonance is blue-shifted as loss is introduced into the system which could be due to Babinet's principle[95]. This section shows the impact of introducing a small loss (k=0.1) to an idealized lossless VO_2 system and shows the absorption enhancement at resonance for each of these geometries.

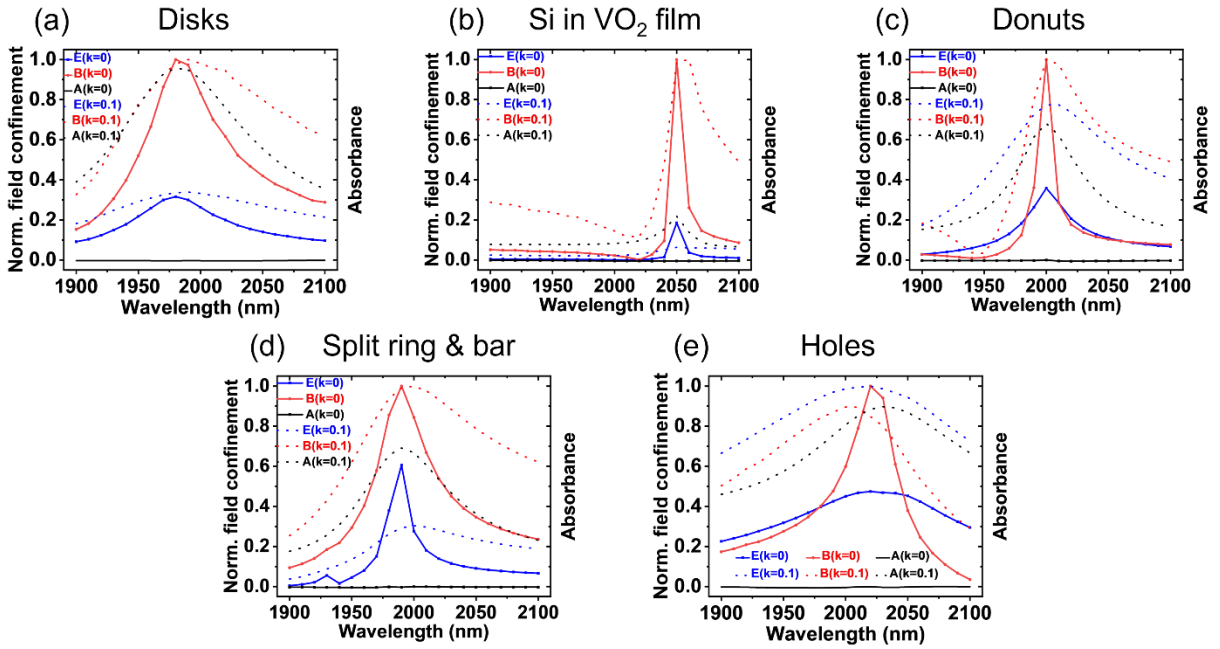

Figure 3.3: Resonance in lossless and lossy VO_2 metasurfaces

(a). VO_2 nanodisks with spectrally overlapping resonances at 1960 nm. (b). Silicon disk in VO_2 film with spectrally overlapping resonances designed at 2050 nm. (c). VO_2 donuts with spectrally overlapping

resonances at 2000 nm. (d). VO_2 split ring and bar engineered to excite spectrally overlapping resonances at 1980 nm. (e). VO_2 holes with spectrally overlapping resonances at 2020 nm.

3.4 – VO_2 Metasurface Fabrication

The VO_2 thin films can be grown using a variety of physical vapor deposition methods such as, sputtering, pulsed laser deposition, and sol-gel methods[96]. There have also been some demonstration of growth using chemical vapor deposition methods as seen in the reference[97,98]. Vanadium, as a transition metal, has multiple oxidation states and can form many thermodynamically stable oxides[99]. Many of these oxides have a transition from insulating to metallic behavior; however, for most of them, the transition temperature is significantly higher than room temperature, which is less desirable for thermal or non-thermal modulation. This multiplicity of stable oxide states makes it challenging to obtain stoichiometrically accurate VO_2. Different growth methods and conditions also result in different grain sizes and sample uniformity which affects the optical properties of the material and can cause deviations over large area nanostructures. Thus, the thin film growth step requires careful optimization to obtain tunable spectroscopic optical properties that are consistent and repeatable. The selected method was chosen over several other synthesis methods that we thoroughly explored experimentally for comparison, including pulsed laser deposition, solution processing, and rapid thermal processing[100]. An electron microscopy image of the resultant film is shown below, and extensive characterization results for these films are presented.

The nanodisks were fabricated from their thin film precursors using electron beam evaporation of an SiO_2 hard mask, electron beam lithography, and two steps of reactive ion etching.

3.4.1 – VO_2 Thin Film Growth and Characterization

VO_2 thin film growth could utilize one of two ways[101]. The first method involves a single-step synthesis of VO_2 on the substrate where stoichiometry, uniformity, and material properties are fixed in one step. This method is achieved at high temperatures (near 500°C) to permit the crystallization of VO_2 onto the substrate. The second method utilizes a dual-step means where an amorphous vanadium oxide film is grown or spun or drop-casted onto the substrate. This film is then given a post-deposition treatment yielding the desired vanadium dioxide stoichiometry with useful optical properties. In this work, VO_2 thin films are grown on fused-quartz substrates using the second method by RF magnetron sputtering and ex-situ annealing. Fused quartz substrates were chosen due to their low index at wavelengths of interest for device fabrication thus, enabling a high index contrast in the VO_2 device. A VO_2 target (AJA 2" diameter) is used in the first step without substrate heating with an oxygen-vanadium mole ratio close to the desired stoichiometry. The deposition power and pressure were kept at 200 W and 3.3 mTorr respectively for the sputtered films. These films are then annealed in the second step in a hot wall 1" quartz tube furnace under vacuum to yield polycrystalline VO_2 films. Multiple characterization approaches are used to investigate the properties of the synthesized thin films. These include temperature-dependent spectroscopy, X-ray photoelectron spectroscopy, X-ray diffractometry, atomic force microscopy, and variable angle spectroscopic ellipsometry.

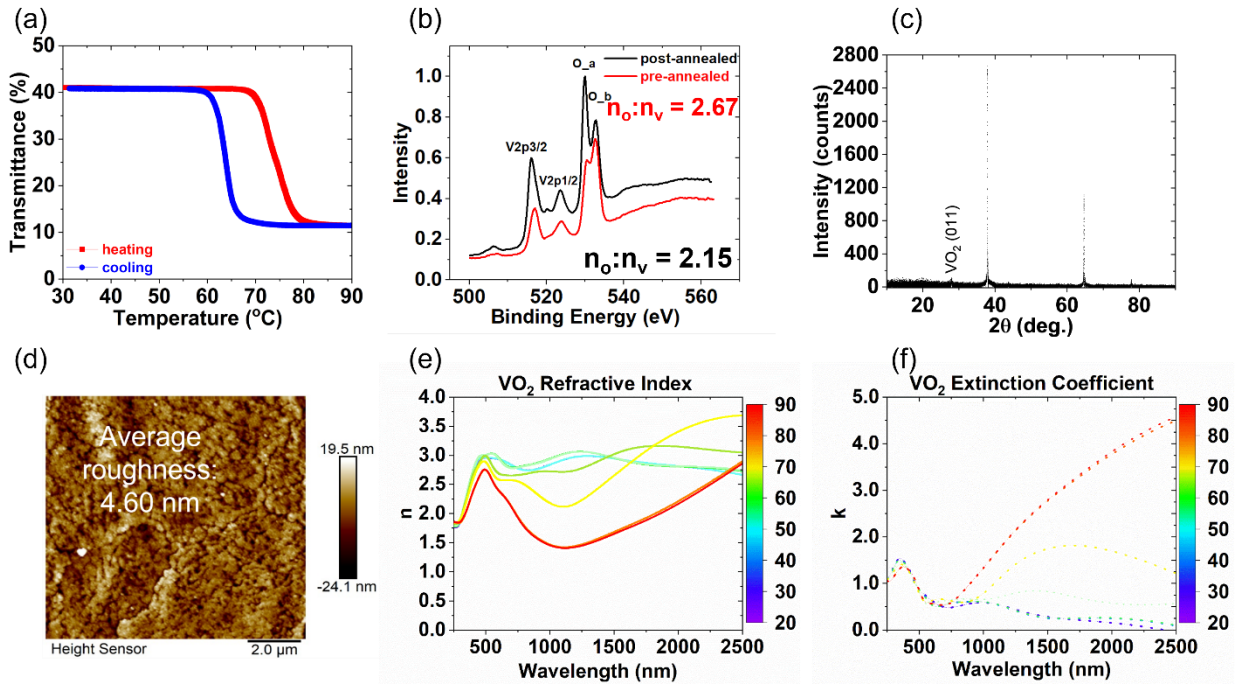

Figure 3.4: ***Thin film characterization on fused quartz substrate***

(a). Temperature-dependent transmittance measurement of a ~170 nm thick film at 1340 nm. (b). X-ray photoelectron spectroscopy showing the mole ratio of the sputtered (pre-annealed) films and the post-deposition treated (post-annealed) films. (c). X-ray diffractometry showing the prominent VO_2 M1 (011) peak at ~28°. (d). Atomic force microscopy image revealing roughness of VO_2 film after annealing. (e). Temperature-dependent refractive index measured using the RC2 Woolam Ellipsometer. (f). Temperature-dependent extinction coefficient showing transition from insulating VO_2 to metallic VO_2 with increase in absorption.

To investigate uniformity of the film over a large area, transmittance maps were taken over a 100 μm by 100 μm area. This area is sufficient to fabricate continuously tunable nanophotonics. The map in the insulating phases shows 51.9% ± 2% transmittance and in the metallic phase shows 16.6% ± 0.8% transmittance (**Figure 3.5**).

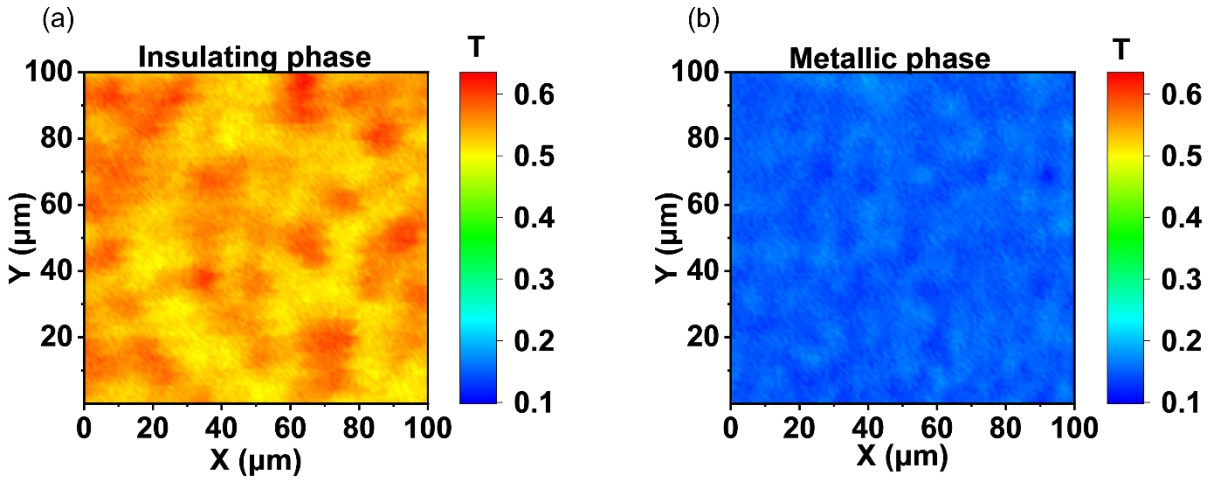

Figure 3.5: Transmittance map of VO2 thin film grown on fused quartz

(a). Insulating phase at room temperature and (b). Metallic phase at 88°C. Both measurements are taken using a supercontinuum laser at 1340 nm with a 1 μm step size.

3.4.2 – VO_2 Thin Film Growth on Z-cut quartz

VO_2 thin films can be grown on different substrates including silicon, fused quartz, and sapphire[102]. In this work, we explored fused quartz and z-cut quartz substrates for VO_2 thin film. Z-cut quartz was chosen with a goal to improve VO_2 thin film growth by growing on vicinal substrates. Although Z-cut quartz is not vicinal, the VO_2 thin film grown on it possessed outstanding optical properties (**Figure 3.6b** and **c**). Z-cut quartz has a hexagonal crystal structure and its lattice constants (a = 4.914 Å, c = 5.405 Å)[103] are close to that of VO_2 (a = 5.38 Å, b = 4.52 Å, c = 5.74 Å)[104] which suggests that there could be quasi-epitaxial growth of VO_2 on the crystalline substrate. The electron micrograph of the annealed VO_2 thin film on z-cut quartz is shown in **Figure 3.6a**.

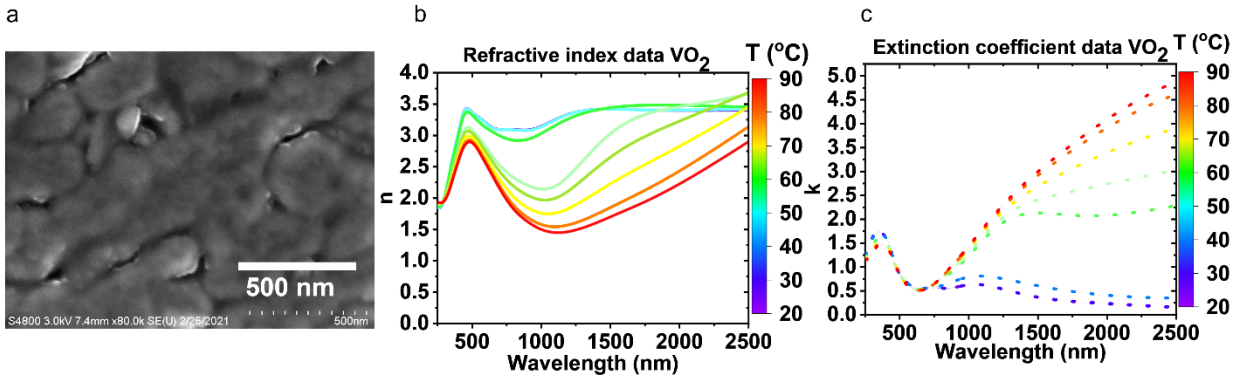

Figure 3.6: ***Thin film characterization of VO_2 on z-cut quartz substrate***

(a). Scanning electron micrograph of VO_2 thin film. (b). Temperature-dependent refractive index showing a refractive index modulation between insulating and metallic phase of ~1.8 at 1282 nm and (c). Temperature-dependent extinction coefficient showing significant increase (~4.7) at 2500 nm between the low loss insulating phase and the lossy metallic phase.

VO_2 thin film growth should be optimized in low humidity atmosphere to minimize flaking effects on the film due to moisture-induced adsorption[105]. Films grown on z-cut quartz substrates seemed to be more prone to moisture-induced adsorption effects relative to those grown on fused quartz substrates possibly due to the very low roughness of the z-cut quartz substrates.

3.4.3 – VO_2 Metasurface Etching

Figure 3.7a shows the fabrication pathway for the VO_2 Huygens nanodisk metasurfaces used in this work. Etching VO_2 anisotropically presents a unique challenge in selecting the right etch recipe and hard mask to achieve nanostructures with smooth vertical sidewalls. Fluoride-based etch gases yield high etch rates due to the high volatility of vanadium fluorides but tend to result in isotropically etched nanostructures. On the other hand, chloride-based etch gases result in slow etch rates and significant redeposition due to the high boiling points of most vanadium

chlorides.[106,107] By heating the sample at an elevated temperature (100 °C) during the etch process and carefully optimizing the etch rate for the sample, well-defined vertical sidewalls can be obtained using the chlorine-based etch recipe, as depicted in **Figure 3.7c**. This level of anisotropy in nanopatterned VO_2 is rare in the available published literature. **Figure 3.7b** shows the morphology of a thin film synthesized, revealing the polycrystalline nature of the VO_2 thin films grown in this work.

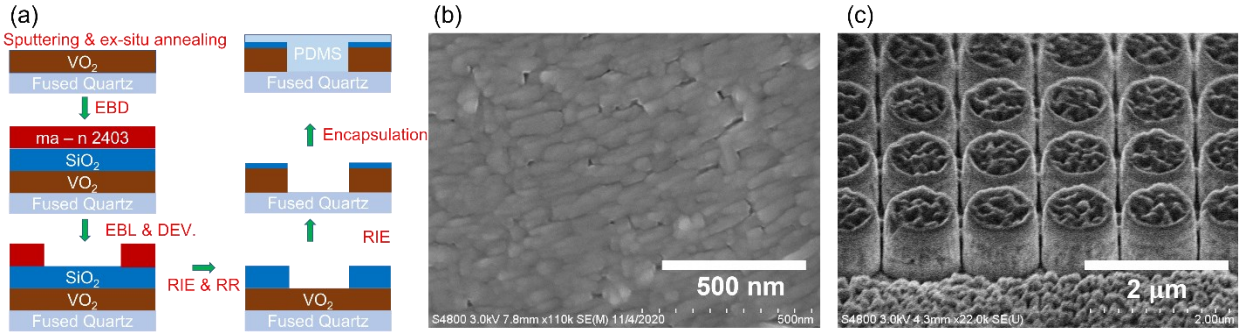

Figure 3.7: ***VO_2 metasurface modulator fabrication***

(a). Schematic showing fabrication pathway for VO_2 Huygens optical modulator. EBD (Electron beam deposition), EBL (Electron beam lithography), DEV (Development), RIE (Reactive ion etching), and RR (Resist removal). (b). Scanning electron micrograph of ex situ annealed VO_2 thin film. (c). Anisotropically-etched VO_2 nanodisks with residual layer of SiO_2 which does not alter the modulating performance of the metasurface (see Appendix C).

3.5 – VO_2 Metasurface Characterization

3.5.1 – Resonance in VO_2 Nanodisks

The transmittance spectrum of the fabricated nanodisks in the insulating and metallic phase is obtained using a spectrometer (Perkin Elmer Lambda 750 S) and compared against its expected modeled results based on feedback from fabrication as shown from the field confinement plot in **Figure 3.8a** using air as the encapsulant. It can be seen clearly in **Figure 3.8b** that resonance dips

are observed at wavelengths close to 2000 nm. This resonance dip disappears in the metallic phase as expected due to dissipative losses in the material. After PDMS encapsulation, it can be clearly seen from **Figure 3.8c** that there is a redshift in the electric and magnetic resonances. The electric field dipole resonance is more sensitive to the higher index change and shifts more to longer wavelengths than the magnetic dipole resonance. This is due to the resonance tuning effect caused by the higher refractive index of PDMS relative to air[78]. We also see this result in a shift in the resonance dip from the transmittance spectrum due to the encapsulant layer (**Figure 3.8d**). From this spectrum, we can select the wavelength for maximum amplitude modulation.

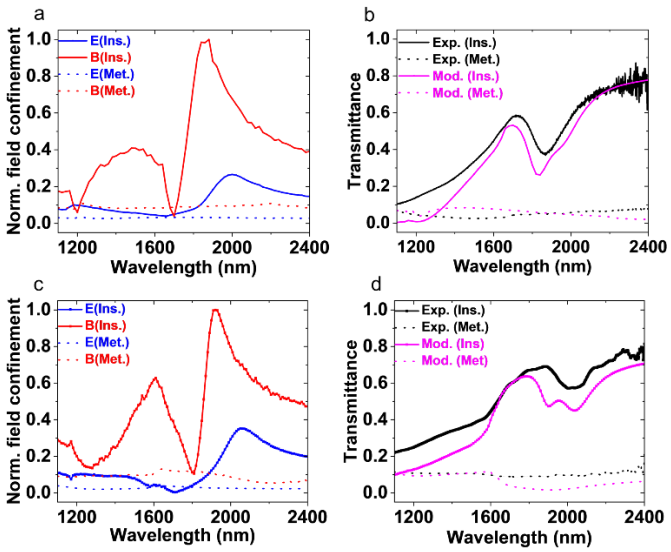

Figure 3.8: Resonances in VO_2 nanodisks.

(a). Modeled field confinement at center of nanodisks based on fabricated geometries before encapsulation. (b). Transmittance spectrum of metasurface before encapsulation. Resonance dip is clearly visible due to spectrally adjacent electric and magnetic dipole resonances (spectral separation = 120 nm). (c). Modeled field confinement at center of nanodisks after encapsulation. Excited resonance modes (dipole and higher order) are redshifted from their original spectral locations in air. The dipole mode resonance spectral separation is 130 nm (d). Transmittance spectrum of metasurface after encapsulation. Resonance dip is red-shifted, and transmittance is slightly enhanced as expected due to a negligible index contrast between the substrate (fused quartz) and the encapsulant (PDMS).

3.5.2 – Optical Modulation in VO_2 Nanodisks

For phase modulation, we model the fabricated metasurface optical response in the vicinity of the higher-order magnetic resonance and search for the highest phase modulation. Here, we select 1635 nm where we obtain a continuous phase modulation of ~67^o as we tune the device from the insulating to metallic behavior as shown in **Figure 3.9b** and an experimentally demonstrated amplitude modulation of ~11 dB at 1635 nm in **Figure 3.9a**. To experimentally confirm the modeled phase shift from the metasurface, we used a custom-made three-beam Mach Zehnder interferometer which uses a continuously referenced method to minimize the effects of drift and noise during the measurements[108]. **Figure 3.9b** shows the modeled phase modulation spectrum around the spectral location of the higher order magnetic resonance. The experimental and modeled phase modulation results agree and show that we have a decent phase modulation at 1635 nm. We then make a temperature-dependent phase measurement at the single wavelength with the highest optical phase shift between structural phases to demonstrate continuous optical phase tunability.

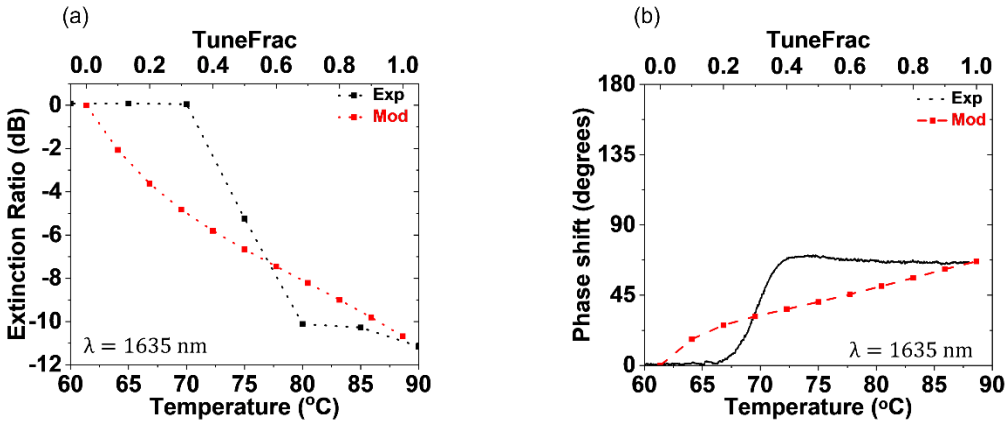

Figure 3.9: Optical modulation in VO_2 nanodisks

(a). Continuous temperature-dependent amplitude modulation comparing experimental and modeling results. (b). Continuously tunable phase shift at 1635 nm comparing experimental and modeling results. Sustained dynamic tunability is achieved over the material phase transition region from ~66°C to ~73°C.

3.6 – Conclusions and Future Outlook

We have modeled and experimentally shown a continuously tunable Huygens metasurface optical modulator operable in the NIR region of the electromagnetic spectrum. The tunable properties are achieved by using a phase change material, VO_2, whose optical properties can be modulated when subject to an external impulse such as temperature, electric field, and optical pumping. In this work, the tunable optical modulation is achieved through thermal tuning. Maximum modeled amplitude modulation of ~19 dB is achieved with a minimal phase modulation of (~35°). The highest modeled phase modulation achieved is 228° with a small residual amplitude modulation of (~4 dB). VO_2 metasurfaces were fabricated successfully and experimental results replicate modeled expectations.

VO_2 metasurface tunable optical modulation can be extended for use in beam steering applications such as in LIDARs by gradual refractive index modulation between structural phases to create a phased array for beam deflection. This can be achieved by using a homogenous

metasurface array where a temperature gradient is maintained along the direction of the modulating phase or by using a gradient metasurface where each nearest neighbor has a different geometry and the structural phases can be gradually tuned by an external impulse[109].

Although VO_2 here was designed in the NIR spectral range, the same design approach can be utilized to design nanophotonic devices in the visible range of the spectrum. By carefully engineering the thin film growth[110,111], relatively low loss (k~0.1) VO_2 can be synthesized. This could be useful for the design and fabrication of tunable integrated nanophotonic devices for applications in the visible[89].

Other means of inducing phase transitions in VO_2 apart from thermal tuning, such as electrical and optical methods, can be explored for faster switching speed and low power consumption. The ultrafast dynamics of the fabricated VO_2 metasurface can be studied using temporal and spatially resolved pump probe measurements, including cathodoluminescence measurements. This could be useful in understanding electron-photon interactions in tunable resonance metasurfaces[112].

This metasurface platform can be engineered for pixelated addressability, which is highly desirable for reconfigurable photonics. Each nanoantenna array can be designed to encode the desired phase information and controlled independently using microheaters. This can be useful for making tunable spatial light amplitude modulators and phase modulators which require no mechanical adjustments for optical performance.

Chapter 4 – Engineering Nearest Neighbor Crosstalk in Huygens Metasurfaces

4.1 – Chapter Overview

The last two chapters have shown efforts towards dynamic active control of optical properties of light using carefully structured nanoantenna arrays. These metasurfaces have identical neighbors, making them suitable for a narrow range of applications such as optical sensing and modulation. For the design and fabrication of more complex devices such as deflectors, lenses, optical cloaks, and holograms, it is necessary to have dissimilar neighbors to achieve the desired amplitude/phase map. Metasurfaces that can excite multipole resonances as well as have a low contrast in relation to their surroundings are strongly affected by nearest neighbor nanoantenna crosstalk. This poses a challenge for the design and fabrication of complex devices since it is impossible to label each nanoantenna independently in the array with its precise imparted amplitude or phase shift.

It will prove essential to accurately characterize the nearest neighbor coupling characteristics of each antenna design using a coupling figure of merit. This could be useful with other design optimization methods to predict designs with minimal crosstalk between adjacent neighbors. Here, we propose a coupling figure of merit which we use to characterize different metasurface designs and use that to predict which design would be the most suitable for beam deflectors as an example case. We investigate three Huygens metasurface designs fabricated in silicon: nanodisks, nanodonuts, and nanobeignets. Our coupling figure of merit is least for the

nanodonut geometry and predicts that geometry to have better performance where reduced crosstalk between dissimilar resonators is critical. We design and fabricate amorphous silicon disk, donut, and beignet beam deflectors on glass and obtain the numerical beam deflection efficiency of 65%, 47%, and 28% respectively for each of these designs.

4.2 – Introduction

From antenna theory, it is known that when two antennas are placed near each other, they experience energy exchange between each other. Some of the energy that one antenna is transmitting is scattered to the nearest neighbor antenna. The amount of energy scattered or transferred from one antenna to another depends on the distance of separation between the two antennas as well as the relative orientation of the antennas[113]. Optical metasurfaces, which are two dimensional arrays of nanoantennas, also experience the nearest neighbor coupling effect. This has far-reaching implications for the actualization of complex optical devices where encoding amplitude and phase information in individual antennas is critical for optimal performance. The coupling effect in nanoantennas is most pronounced in Mie resonance metasurfaces and metasurfaces designed to have a low refractive index contrast between the metasurface and its surroundings, leading to low optical confinement in the metasurfaces[114].

Different approaches have been investigated to overcome nearest neighbor coupling in metasurfaces. These include using truncated waveguide resonators where the high aspect ratio nanoantennas can confine optical waveguide modes within the resonators with minimal leakage to the nanoantenna environment. Here, device performance is due to the contribution of each nanoantenna in the grid rather than mutual coupling between nanoantenna elements in the array[115]. These high aspect ratio structures, however, pose a fabrication challenge in precise pattern

definition through reactive ion etching. Other methods include using small pixelated homogenous arrays in a gradient metasurface[116,117] and numerical optimization of the antenna geometry[118]. In addition, other research work has been done to accurately obtain the performance of complex metasurface devices while accounting for interantenna crosstalk. Some of these include using deep neural network to suggest the electric field of a 50 x 50 μm^2 area while taking nearest neighbor coupling into account[119]. Another method, referred to as the local phase method, quantifies the phase error of each element in a nanoantenna array in the presence of its nearest neighbors, allowing for accurate estimation of the impinged metasurface optical phase values. This method requires the computation of the metasurface as a whole and could be computationally expensive[120]. Also, another approach called the triangulation method solves for the electric field at a point in the far field as a superposition of the scattered electric field due to each nanoantenna in the array. Then using a nonlinear solver, the phase and amplitude of each resonator can be calculated. This method, like the earlier discussed local phase method, also requires a lot of computational memory for complex metasurface devices[121].

In this work, we propose an empirical parametric coupling figure of merit for different metasurface designs, providing information on the relative coupling strength in each design space. Small changes in metasurface designs can lead to more efficient optical confinement in the resonators which will minimize mutual coupling between adjacent nanoantenna elements. A coupling figure of merit can be useful in providing a numerical estimation on the coupling intensity across different designs and aid in making the right design decisions before fabricating gradient metasurface devices with dissimilar nearest neighbors in the array. To demonstrate the accuracy of our proposed figure of merit, we simulate and fabricate different Huygens metasurface beam deflector designs and compare their deflection efficiency with their numerical coupling figure of

merit. The design with the least figure of merit is expected to yield the best deflection efficiency without further design optimization. This assumes that all elements chosen for the beam deflector metasurface transmit light at nearly 100% at the design wavelength. This can prove to be a quick and easy way to overcome coupling in Huygens metasurface platforms using a geometrical approach and a figure of merit for tracking changes in coupling strength with changes in geometry.

4.3 – Coupling Figure of Merit

The coupling figure of merit (FOM) is here defined for a set of two nanoantennas where the geometry of one is kept fixed while the geometry of the other is varied. It is the average deviation of the normalized amplitude or phase values of a homogenous array for a set of parameters spanning a 2π phase range. The FOM seeks to answer the following question: how can one predict the strength of interaction between nearest neighbor nanoantennas if nanoantenna A is kept fixed while nanoantenna B is varied (see **Figure 4.1**)?

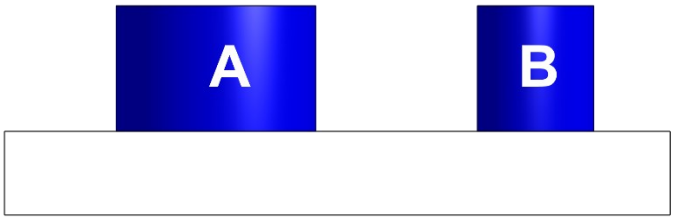

Figure 4.1: ***Schematic to define mutual coupling between nanoantennas of different geometries***

Antenna A is the test antenna and Antenna B is the nearest neighbor that is varied to investigate the impact of coupling on Antenna A's performance.

The FOM is thus defined as:

$$\mathrm{FOM_P} = \sqrt{\sum_{\emptyset_B=0}^{\emptyset_B=2\pi} \left[\frac{\Delta P^2}{N}\right]} \qquad (4.1)$$

where:

ΔP – normalized parameter change (amplitude or phase) for the antenna A when antenna B is varied.

$\emptyset_B$ – antenna B phase and,

N – total number of different neighbor phases sampled.

The effect of mutual coupling in an antenna array can lead to element pattern distortion, effective index variation, and polarization variation for antenna systems that are polarization-sensitive[113]. In this work, we choose to characterize mutual coupling by using the derived FOM equation across diverse Huygens metasurface designs. The FOM value for the ideal array (with zero coupling between nearest neighbors) will be equal to zero. The degree to which the obtained FOM values for different material and geometric platforms investigated is close to zero will represent the degree to which nearest neighbors in the selected geometry are not coupled to each other.

Here, we show the results for three Huygens metasurface geometries, namely nanodisks, nanodonuts, and nanobeignets. The nanodisk geometry was chosen since it represents a standard for comparison with literature. The nanodonut geometry was selected since a 2π phase shift can be obtained by changing the inner diameter while keeping the outer diameter fixed (**Figure 4.2a**). Also, the electric field in the nanodonut is strongly confined in the core while the magnetic field is strongly confined in the outer diameter of the structure and is hypothesized to reduce the impact

of coupling on varying nearest neighbor nanoantenna geometries. In the beignet geometry, varying the side length results in a 2π phase shift (**Figure 4.2b**). The nanobeignet geometry was chosen over the block geometry which gives similar results for ease of fabrication since the edges are made up of fillets instead of sharp, pointed tips that may be difficult to precisely fabricate. Also, to study a geometry close to the circle geometry with less lines of symmetry. The nanobeignets have a squircle shape but the name, beignet was selected since it has a similar shape to the local French donut. First, we obtain a set of geometric parameters for each Huygens metasurface design that, when varied, will produce a zero to 2π phase shift for a homogenous array. Using the nanodisk geometry as the reference geometry, the nanodonut and nanobeignet geometries are plotted in **Figure 4.2** against a phase range from 0° – 360°.

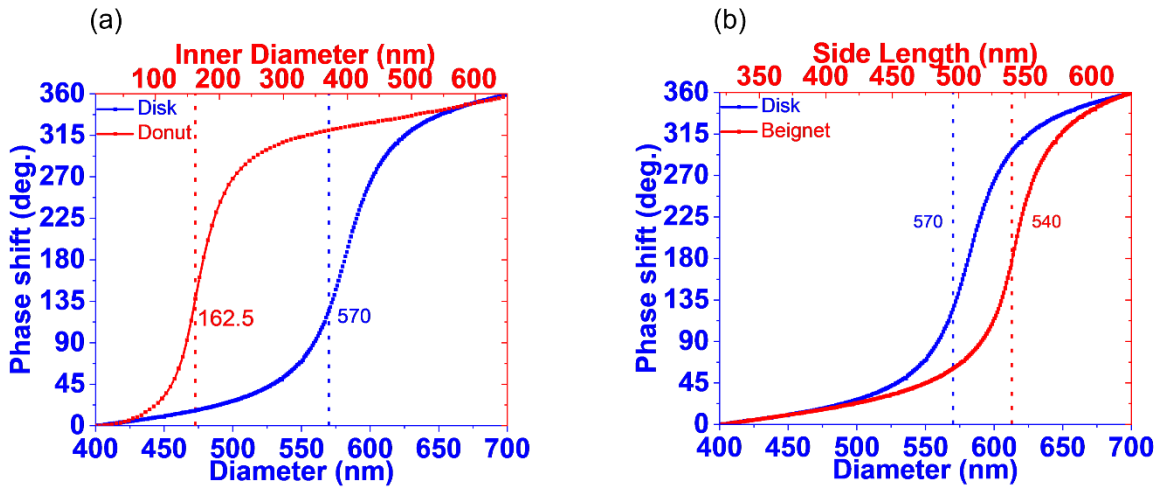

Figure 4.2: ***Huygens metasurface optical phase shift vs. geometry***

(a). Disk and Donut diameter sweeps and (b). Disk and Beignet geometric sweeps covering a full 2π phase range.

Next, two antennas are placed side by side and the geometry of one is varied (Antenna B) while the other one is kept fixed (Antenna A). The transmittance of the nanoantenna array is obtained and compared against the homogenous array with identical neighbors. The phase shift of

the inhomogenous array with varied nearest neighbor is obtained and compared against the reference homogenous array with identical nearest neighbors. The phase shift is measured in the far field of the nanoantenna array. The results are shown in **Figure 4.3**. In **Figure 4.3a**, the disk shows a steeper change in transmittance relative to the donuts as we vary Antenna B. In **Figure 4.3b**, the forward scattered amplitude changes at a much faster rate in the beignets compared to the disks. These suggest based on our proposed coupling figure of merit equation, that the donut geometry has a less significant coupling effect among nearest neighbors compared to the disks and the beignets. For smaller diameters of antenna B, the evanescent field increases around the antenna leading to less field confinement and potentially more nearest neighbor coupling.

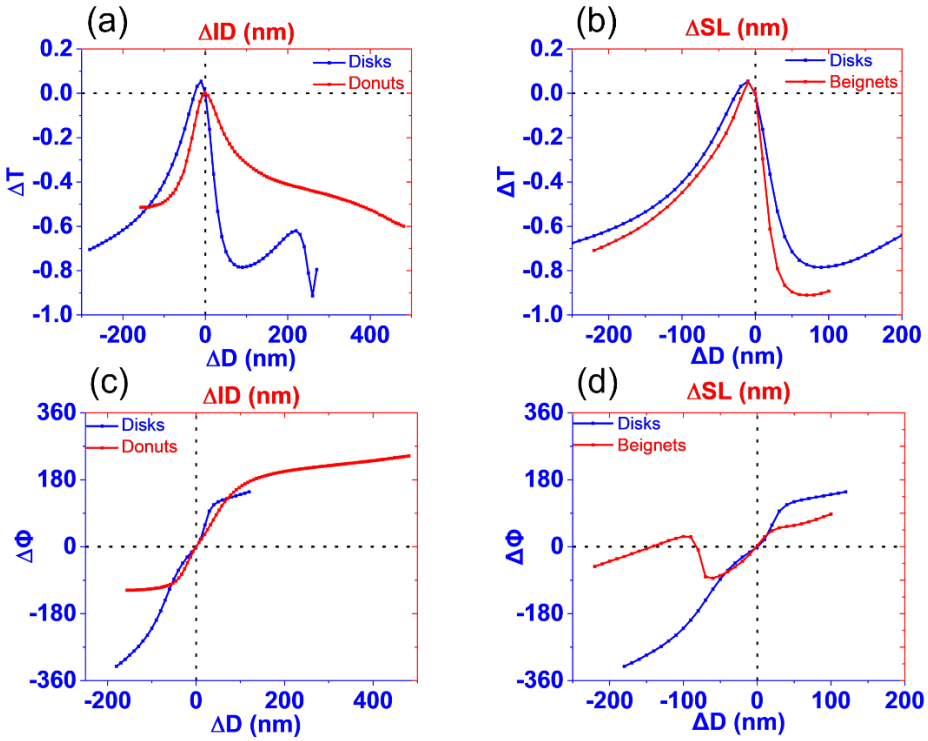

Figure 4.3: Coupling test with two nearest neighbors for various metasurface designs

(a). Transmittance change for variations in disk and donut diameters and (b). Transmittance change for variations in disk and beignet diameters relative to the transmittance of the fixed geometry of antenna A. (c). Optical phase change for alterations in disk and donut diameters and (d). Optical phase change for changes in disk and beignet diameters relative to the fixed geometry

of antenna A. ΔD refers to change in diameter, ΔID refers to change in internal diameter for the donuts, ΔSL refers to change in the side length of the beignets.

The FOM for each geometry was then calculated using equation 3 as shown above. The different root mean square value deviations for the disk, donut, and beignet examined are: 0.52, 0.42, and 0.59 respectively. Based on this FOM results, the donut geometry was expected to perform the best for inhomogeneous phase gradient arrays.

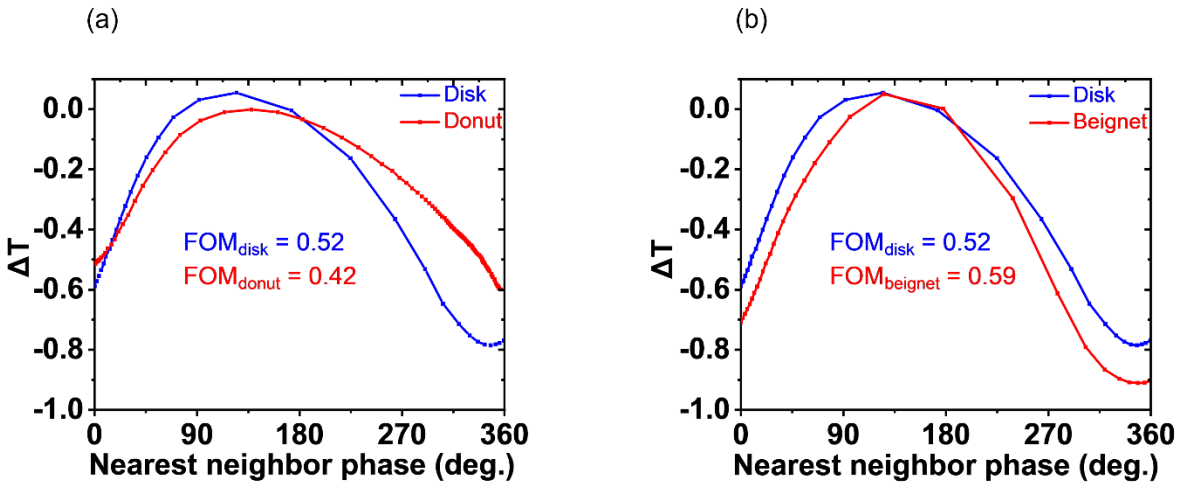

Figure 4.4: FOM for Huygens metasurface designs

(a). Disk vs. Donut geometry and (b). Disk vs. Beignet geometry transmittance change for varying nearest neighbor phase shift where the test Antenna A has a phase shift of 61.1°, 43.3°, and -146.2° for the nanodisk, nanodonut, and nanobeignets. Figure of merit for each metasurface type is given based on this data.

4.4 – Beam Deflector Design and Fabrication

To experimentally observe the detrimental effect of nearest neighbor coupling between dissimilar antennas, we design and fabricate beam deflectors with the modeled Huygens metasurface designs. The beam deflector was chosen since it imparts a linear phase gradient on the impinging beam and can steer the beam into a desired direction. Each Huygens metasurface design was optimized to excite spectrally overlapping resonances for a homogenous array at 1550

nm as shown in **Figure 4.5**. This was done so that backward scattering could be minimized according to the Kerker condition, leading to efficient forward scattering. Then, parametric sweeps are done to select the geometries of highly transmissive nanoantenna elements (HTNE) which span a 2π phase shift, denoting full wavefront control. The design is comprised of amorphous silicon nanoantennas on a glass substrate encapsulated by polydimethylsiloxane (PDMS). Amorphous silicon was chosen due to its high refractive index and low loss in the infrared spectrum as well as its relatively simple fabrication. PDMS was chosen as the encapsulant due to its refractive index match with the glass substrate; it also helps to protect the metasurface from damage.

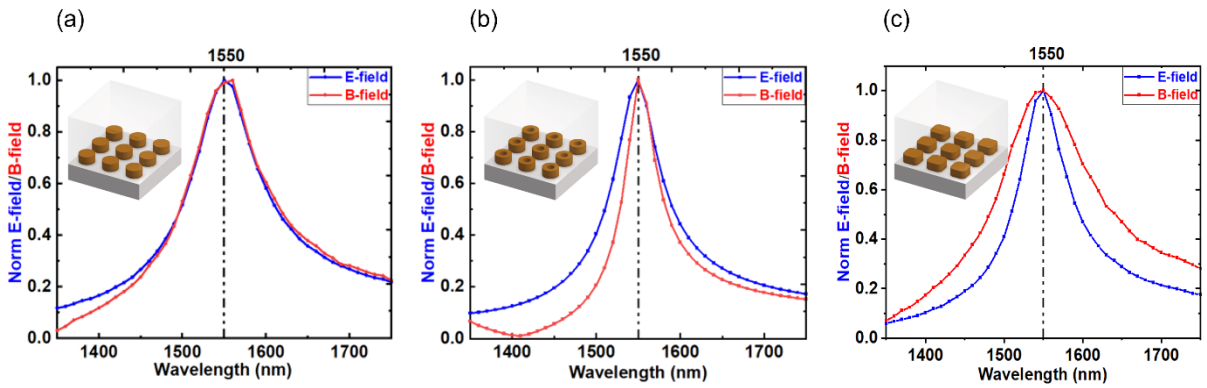

Figure 4.5: ***Resonance spectra for Huygens metasurface geometries***

Overlapping resonances at 1550 nm for a homogeneous array of (a). Silicon nanodisk Huygens metasurfaces (b). Silicon nanodonut Huygens metasurfaces and (c). Silicon nanobeignet Huygens metasurfaces. Inset shows a 3 x 3 homogenous array for each of the metasurface geometries presented here.

To obtain a set of eight elements for the phase gradient beam-deflecting metasurface, the circle diameter is swept above and below the diameter associated with the resonant wavelength of interest without varying all the other parameters. From here, a basic set of homogenous array geometries can be obtained. However, this method results in relatively low efficiency optical deflectors due to non-uniform unit cells. To mitigate this effect, we use a design control such that the unit cell dimensions are fixed in both the x and y directions respectively (see **Figure 4.6**). This

is achieved by choosing a set of HTNE where the diameter along the x-direction is fixed (direction of magnetic field) and the unit cell along the y-direction is fixed (direction of the electric field). Previous studies have shown that this approach to obtaining metasurface beam deflectors is favorable because the overlapping electric and magnetic dipole resonances respond in the same way to change in diameter along the electric field direction. Elements of the phase gradient metasurface are selected based on a predetermined number of phase levels spanning a 2π phase range (**Figure 4.2**). All Huygens metasurface beam deflector geometries discussed in this section were designed following this approach except for the nanodonut geometry, which is unique with the x and y outer diameters fixed and the x and y inner diameters both varied to achieve full 2π phase shift. We then select elements with high transmittance values (transmittance > 90%) which follow the predetermined set of phase levels to complete the basis set for the unit cell of the beam deflecting metasurface (**Figure 4.2**). The details of the geometries selected for each set of Huygens metasurfaces used in the beam deflector designs are given in Appendix D.

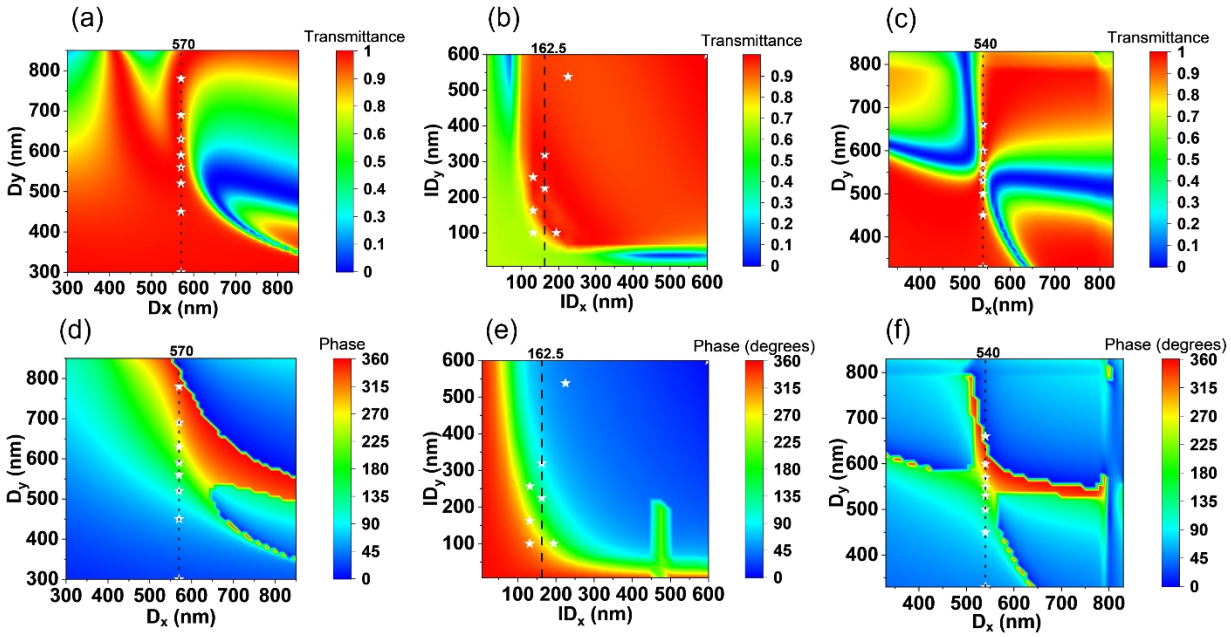

Figure 4.6: Transmittance and phase plots vs. changing metasurface geometries

Transmittance contour plots for (a). nanodisk, (b). nanodonut, and (c). nanobeignet Huygens metasurface geometries and phase contour plots for (d). nanodisk, ©. nanodonut, and (f). nanobeignet Huygens metasurface geometries. Black dotted lines indicate the geometric parameter for the peak of the metasurface resonance at the designed wavelength. White stars show eight HTNE spanning 2π phase shift for each geometry selected. D_x – Diameter along the x-direction, D_y – Diameter along the y direction, ID_x – Inner Diameter along the x-direction, ID_y – Inner Diameter along the y-direction.

The beam deflecting metasurface is designed using finite element modeling (COMSOL Multiphysics with RF module) and the beam deflecting performance is analyzed using a custom-designed mode analysis algorithm which uses the Fast Fourier transform to obtain the deflected intensities and phase. The outgoing anomalously refracted angle is calculated using the generalized Snell's Law equation[122]. The deflected angle is then calculated by subtracting the incident angle from the outgoing transmitted angle. Using the generalized Snell's law equation[123], the anomalous deflection angle was calculated for each of the designs demonstrated. The target deflection angle is 9.0°, 8.3°, and 9.4° for the nanodisk, nanodonut, and nanobeignet geometries respectively

These metasurfaces are fabricated using electron beam evaporation, electron beam lithography, and reactive ion etching. The details of the fabrication steps are similar to the steps

used in Chapter 2 without the addition of the microfluidic channels. **Figure 4.7** shows the morphology of the fabricated Huygens metasurfaces. Fabrication is currently being optimized for the donut geometries to obtain designed hole dimensions in the donut.

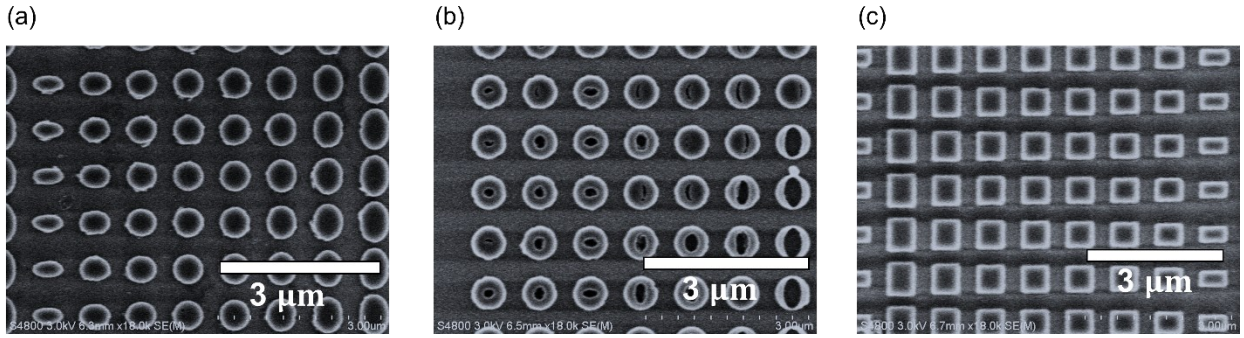

Figure 4.7: SEM of Huygens metasurface beam deflectors

(a). Silicon disk beam deflector, (b). Silicon donut beam deflector and (c). Silicon beignet beam deflector after electron beam resist development.

4.5 – Beam Deflection Efficiency

The beam deflection efficiency is obtained using the mode analysis algorithm as stated earlier. This algorithm first takes in the electric field data of the background field (no metasurface elements; all domains set as PDMS). This is useful for taking the reflected modes from the metasurface into account if working with a reflective metasurface. It also takes in the electric field data where the material domains include the encapsulating material and the substrate material only. This is useful as reference data for obtaining deflection angle and efficiency from a transmissive metasurface. Lastly, it takes in the scattered electric field data from the metasurface surrounded by the encapsulant and substrate materials in the full metasurface model. These datasets are concatenated, yielding square matrices, to make the Fourier transform operation easier and accurate. The beam deflecting efficiency from the transmissive metasurface is obtained by dividing

the metasurface Fourier intensity in a particular mode by the Fourier intensity of the electric field without the metasurface (that is, when the material domains are set to the encapsulant and substrate materials).

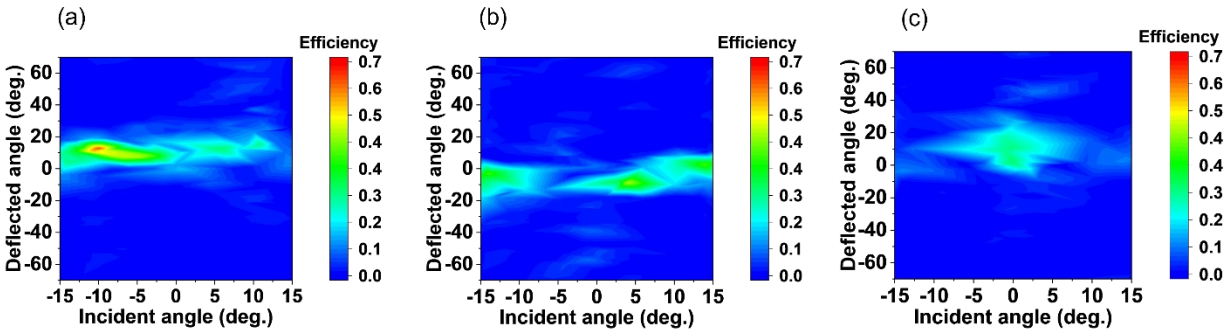

Figure 4.8: Beam deflector efficiency for different Huygens metasurface designs

(a). Disk geometry with a maximum deflection efficiency of ~65%, (b). Donut geometry with a maximum deflection efficiency of ~47%, and (c) Beignet geometry with a maximum deflection efficiency of ~28%.

As shown in **Figure 4.8**, the highest efficiency of the nanodisk is greater than the nanodonut although, the nanodisk has a higher nearest neighbor coupling strength as determined by the coupling figure of merit equation. This may be because of the inclusion of elements in the donut geometry with relatively low transmittance (< 90%). These elements were chosen to satisfy the phase requirement of a gradual, linear phase gradient spanning a 2π phase shift. The average transmittance of the selected elements for the nanodisk, nanodonut, and nanobeignet beam deflectors are 0.98, 0.93, and 0.95 respectively. An effective maximum beam deflection efficiency is then obtained by normalizing the numerically calculated beam deflection efficiency using the average transmittance values for each geometry. This yields effective maximum efficiencies of ~66%, ~50% and, ~29% for the nanodisk, nanodonut, and nanobeignet geometries respectively.

Another possible explanation for the discrepancy between the FOM prediction and the numerically determined deflection ef.ficiency is that the current definition of efficiency is

governed by only change in one optical parameter which is the amplitude (in this case the forward scattered amplitude). By incorporating the change in optical phase as the diameter of antenna B varies relative to antenna A, an effective FOM can be determined which should be more accurate towards estimating the field interactions between both antennas. This makes sense here since the electric field shared between both antennas is a function of both the optical amplitude and phase. A hypothetical effective FOM equation can be the following:

$$FOM_{eff} = 0.5 \times (FOM_T + FOM_{\emptyset}) \quad (4.2)$$

where:

FOM_T – FOM based on transmittance.

$FOM_{\emptyset}$ – FOM based on phase.

FOM_{eff} – Effective FOM based on contributions from scattered amplitude and phase.

The FOM_{eff} is defined here as the average of the two figures of merit discussed and its validity can be tested across multiple designs.

In addition, the nanobeignet design which has the least maximum beam deflection efficiency has only four lines of symmetry relative to the disks and donuts which have infinite lines of symmetry in a homogenous array. Breaking the symmetry as seen in inhomogenous gradient arrays could be more sensitive to coupling and reduce the overall maximum efficiency of the gradient metasurface. To confirm this, it could be useful to obtain the coupling figure of merit and design metasurface beam deflectors using geometries with varying symmetry such as a rhombus. This could further push our understanding of the correlation between symmetry and interelement coupling in nanoantenna arrays.

4.5 – Conclusions and Future Outlook

In summary, an empirical coupling figure of merit was developed for Huygens metasurfaces to quantify the extent of interelement coupling between nearest neighbor nanoantennas across diverse designs. Across the three dielectric Huygens metasurface designs investigated, namely amorphous silicon nanodisks, nanodonuts, and nanobeignets, the nanodonut gave the closest figure of merit value of 0.42 to an ideal metasurface element geometry where no nearest neighbor coupling exists. This indicates that dielectric nanodonut arrays are expected to be relatively efficient gradient metasurfaces. Gradient beam-deflecting metasurfaces are designed for each of these three resonator types to validate the FOM prediction for best performance with minimal perturbations from nearest neighbor coupling. The designed beam deflection efficiencies of the Huygens metasurface designs discussed here are ~65% (nanodisk), ~47% (nanodonut), and ~28% (nanobeignets), where variations in the transmission in each resonator type need to be accounted for in the final analysis. Fabrication and characterization of these structures is well underway.

Going forward, we will fabricate and optically characterize these Huygens metasurfaces, comparing their designed deflection efficiencies and angles with experimental results and further confirming whether the formulated nanoantenna coupling FOM is a useful method for analyzing nearest neighbor coupling in metasurface designs or not. Also, to further establish this FOM as a standard for characterizing nearest neighbor coupling in optical nanoantennas, it will be necessary to apply the FOM to other geometric and material platforms such as plasmonic nanoantennas, Paratchatnam-Berry phase nanoantennas, and truncated waveguide nanostructures.

Furthermore, this coupling FOM could be applied to a mix of different intuitive nanoantenna designs such as a disk-donut dimer where a unit cell is composed of a disk and a donut. Exploring these designs could unravel novel engineered structures that help to confine light better, leading to more efficient beam shaping metasurface devices. A more complex phase gradient metasurface, such as a lens or hologram, can then be designed and fabricated with a geometry selected based on its performance according to the proposed FOM.

In addition, the geometry of other nearest neighbors in an array such as second or third nearest neighbors can be varied and characterized using the proposed FOM to determine whether the proposed FOM should be expanded to include the impact of these additional next nearest neighbor antennas. This could help elucidate the impact of geometric variations in multiple nearest neighbors on the nanoantenna element whose geometry is not varied.

Chapter 5 – Towards the design and fabrication of highly efficient tunable metaholograms

5.1 – Chapter Overview

Optical metasurfaces may prove to be useful in optical display and holographic applications due to their ability to rapidly impose a sudden phase shift on impinging light. These metasurfaces are particularly beneficial because of their smaller footprint, allowing for easier and efficient photonic device integration. All-dielectric Huygens metasurfaces are desirable for use in highly efficient metasurface holograms due to their low loss and low aspect ratio, which may be beneficial towards efficient fabrication. Their responsiveness to changes in material and geometric properties make them suitable for efficient, reprogrammable holograms. However, the nearest neighbor crosstalk that exists in this nanoantenna type makes the hologram design challenging. In this chapter, progress towards precise determination of individual phase values for each holographic pixel is demonstrated. First, we use the Gerchberg-Saxton algorithm to retrieve the target hologram's phase map from a target image. Then, we show progress towards a phase-to-nanoantenna map using a numerical solver to obtain solutions to nonlinear equations generated by the triangulation method. When fully developed, this method may pave the way towards achieving low aspect ratio reconfigurable photonic beam shaping metasurface devices like beam deflectors, lenses, orbital angular momentum modulators, and holograms.

5.2 – Introduction

Holography is a way through which full-scale optical wavefront control can be demonstrated by recording and reconstruction of an optical field. It was first demonstrated by Dennis Gabor in 1948 and initially used in electron microscopy[124]. It was then adapted for application in optics after the laser was invented. Holography solves the basic problem of writing and reproducing the optical field information obtained from a coherently illuminated 3-D object. The recorded optical information includes the amplitude and phase of the optical wave scattered off the recorded object, which preserves the total object details better than conventional optical detectors that can only record the intensity of light[125]. This is usually an interference pattern of the object field and a reference beam separated by a beam splitter. The reference beam is guided by some optics, e.g. a mirror, to a light sensitive recording device, e.g. a photographic plate, where both beams interfere. To reconstruct the object field, the reference beam is impinged onto the recording device allowing the object field to be reproduced. The viewer then sees a diffracted optical field, or virtual image, of the original object[126].

Although conventional holography enables encoding and decoding of the entire optical field of an object, the recording method poses some challenges, including large footprint, reduced resolution, and small viewing angle. Recently, optical metasurfaces which are subwavelength two-dimensional antenna arrays have been shown to be able to arbitrarily manipulate the amplitude, phase, polarization, and wavenumber of light abruptly according to design. This approach has numerous benefits compared to conventional holographic recording methods because of its potential for high spatial resolution, high signal-to-noise ratio, smaller footprints, elimination of

unwanted diffraction orders, as well as larger viewing angles, all of which may be achieved using metasurface holograms[127].

Significant research has been done to realize the design and fabrication of metasurface holograms. Several groups have presented plasmonic metasurface holograms which are mostly polarization dependent with efficiencies ranging from 0.54% to 80%[75,128–130]. These low efficiencies in some of the demonstrated holograms are due to dissipative losses in the plasmonic material used. To circumvent this, dielectric metasurface holograms have been shown to reach record efficiencies of 97.9%[73,131].

The metasurface holograms described above were mostly designed for static functionality. Dynamic reconfigurability is highly desired and applicable in optical encryption, tunable optical displays, as well as augmented and virtual reality platforms[9,80,116].

The steps in making a tunable metasurface hologram from an existing object or image include phase map quantization in all tuning states, nanoantenna selection to switch between tuned states, and fabrication. Each of these steps can contribute to loss in overall conversion efficiency, so it is important to optimize each process pathway towards achieving highly efficient tunable metaholograms.

5.3 – Phase Map Design

Electromagnetic fields oscillate on the order of 10^{15} Hz and conventional optical photodetectors can only detect the intensity of the light at these frequencies[132]. The phase information in the light wave is not captured, leading to loss of a significant part of the optical information in the wave. A quick experiment to show that the phase of an object field contains

important information about the field was performed. The Fourier transform operation was done on two different images and their phases were interchanged, convolved with the respective object Fourier intensities and the inverse Fourier transform was obtained. Although the Fourier magnitudes for each image were not interchanged during the convolution, the inverse Fourier transform yielded an output that matches the other image in the test associated with the swapped phase (**Figure 5.1a**). A control test was done where their Fourier intensities were exchanged, convolved with their respective Fourier phases and the inverse Fourier transform was done. The inverse Fourier transform yielded an output that matched each original image whose Fourier phase was not interchanged (**Figure 5.1b**). This confirmed that a significant portion of the object field information is contained in the lost phase of the object when it is not retrieved.

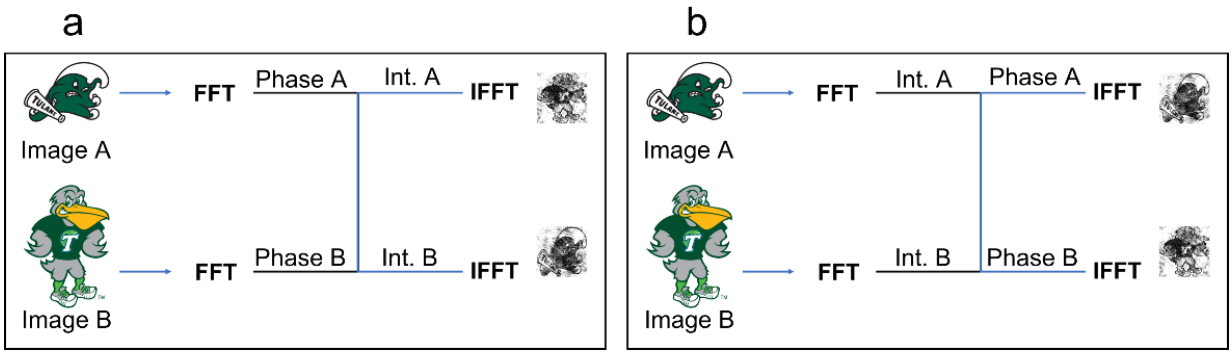

Figure 5.1: Importance of phase information in image processing

(a). Fourier phase of the two images swapped and intensities kept constant. The images are preserved in the phase information. (b). Fourier intensities of the two images swapped and phase kept constant. Again, the images preserve their respective phase information after the inverse fourier transorm operation.

To map the holographic phase to be recorded from an image, a way of extracting the phase information from the intensity information that is recorded should be used. Many methods have been developed which are in general iterative to retrieve the lost phase information from measured intensity data. These include using error-reduction algorithms such as the Gerchberg-Saxton

algorithm, the steepest-descent method, the input-output algorithm, and the conjugate-gradient method[133]. The Gerchberg-Saxton algorithm was used in this work and was sufficient towards obtaining a phase map from an image that may be used to create a tunable metasurface hologram.

5.3.1 – Gerchberg-Saxton Algorithm

The Gerchberg-Saxton (GS) algorithm is an iterative error-reduction algorithm designed to obtain fast solutions of the phase of a complete wave function whose intensity is propagated in an iterative fashion between the Fourier and imaging planes of a viewing system[125,134,135]. This algorithm solves for the object function O(x,y) from the magnitude of its Fourier transform |P(ux,uy)| using the following steps.

Let Fk(u), Φk, fk(x), fk(u) be estimates of the Fourier magnitudes, phase, measured, and object magnitudes.

1. Assign a random phase to the object function O(x,y) in the image plane. A random phase is selected for nearly uniform energy distribution across a wide range[126]. Let φ_x be the chosen random phase. Neglecting the initial object magnitude for this phase-only hologram, we can write the object function as $fk(x) = \exp(i\varphi_x)$.
2. Obtain the Fourier transform of fk(x). This ensures that the new object function in the image plane is propagated to the Fourier plane.

   $Fk(u) = FT[\exp(i\varphi_x)]$
3. Replace the Fourier magnitude by the measured object magnitude while retaining the Fourier phase.

   $Fk'(u) = fk(u)[\exp(i\varphi_x)]$
4. Obtain the inverse Fourier transform of step 3 above.

5. Illuminate the computed phase hologram by convolving the phase with a gaussian beam.
6. Obtain the inverse Fourier transform of step 5 above.
7. Compare the resulting object magnitude to the original object magnitude and evaluate the error.
8. Update the Fourier phase in step one based on the result in step 7.

The obtained Fourier phase map can be discretized according to the desired number of phase levels to be used in the nanoantenna design. **Figure 5.2** shows the results from the GS algorithm test on a Tulane Angry Wave image. It can be clearly seen that the reconstructed image looks very much like the original normalized grayscale image. The phase map shown in **Figure 5.2b** is sufficient to retrieve the image and may now be converted into a phased array metasurface design.

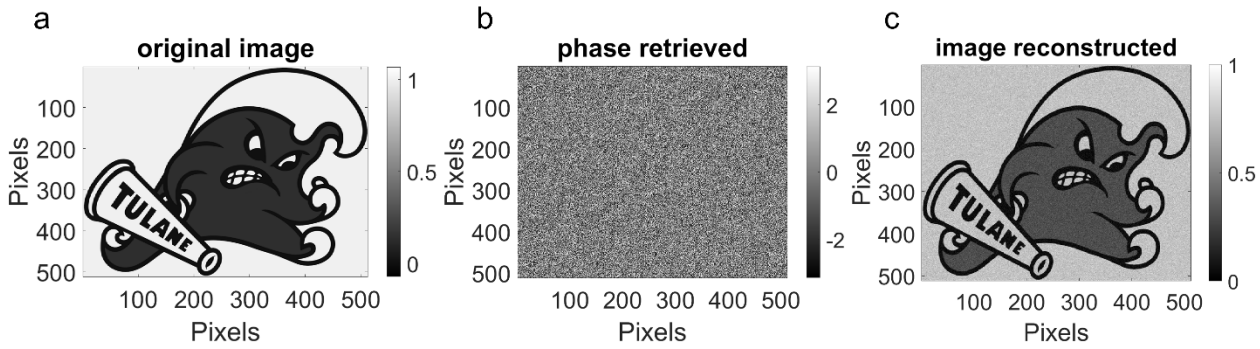

Figure 5.2: GS algorithm results

(a). Original image normalized to grayscale values. (b). Phase retrieved from GS algorithm and (c). Image reconstructed from retrieved phase using GS algorithm.

5.4 – Nanoantenna Design

After the phase map is obtained and discretized according to the desired number of phase levels, the next step is to find the library of antennas that accurately encodes this quantized phase map. The mode of operation of our low aspect ratio Huygens metasurfaces which support Mie dipole resonances depends on coupling between the incident light and the nanoantennas as well as

coupling between nearest neighbor nanoantennas. The crosstalk between nearest neighbor antennas ensures that each nanoantenna phase is dependent on the phase of its nearest neighbor in the array, making it challenging to encode unique phase values in individual nanoantenna elements in the array. To accurately determine each nanoantenna's phase value with varying nearest neighbors, we adopted the triangulation method to solve for individual phase values.

5.4.1 – The Triangulation Method

The triangulation method is based on the principle of superposition. Here, the scattered field at each point in the imaging domain is a superposition of the field due to each scatterer in the array. The phase and amplitude at each point can be obtained by setting them as unknowns in a system of nonlinear equations. To illustrate this method, we use a 1 x 3 nanoantenna array and solve for the phase and amplitude of the center nanoantenna. The process starts by computing the scattered electric field due to these nanoantennas using finite element method in COMSOL Multiphysics RF module. As shown in **Figure 5.3a**, the electric field at point P_1 is a superposition of the scattered electric field contribution of each of the three nanoantennas in the array. Three points are then selected (**Figure 5.3b**) in the imaging domain and the electric field values at these points are noted. The electric field at each point is a sum of the scattered electric fields due to each of the three nanoantennas present in the array.

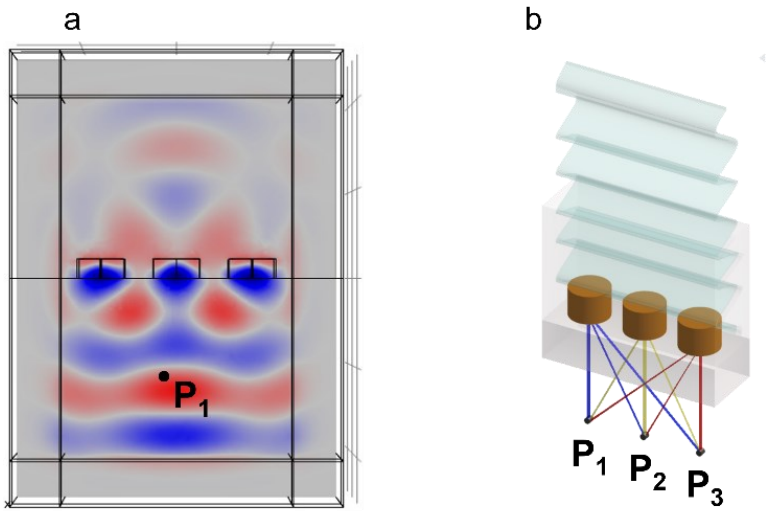

Figure 5.3: The Triangulation Method

(a). Scattered field due to three similar nanoantennas placed beside each other. P_1 is a point in the far field where the scattered electric field can be approximated to behave like a plane wave (b). Schematic showing three points P_1, P_2, and P_3 beneath three nanoantennas where the electric field at each point is a sum of the scattered electric field due to each nanoantenna in the array.

Three non-linear equations are obtained at each of these points, approximating the antennas as electric dipoles designed to scatter efficiently in the forward direction and suppress scattering in the backward direction. While this is a reasonable approximation, it is important to note that the dielectric nanoantennas do not exactly behave like an electric point dipole source. The electric field of a single point dipole emitter is given as:

$$E = \frac{k^2}{4\pi\varepsilon_0 r} e^{ikr} \qquad (5.1)$$

while the electric field of a dielectric nanoantenna is slightly different due to the design constraint for efficient scattering in one direction, leading to a suppression of the scattered field in the opposite direction[136]. The equation describing the scattered electric field is then modified to be:

$$E = \frac{k^2}{4\pi\varepsilon_0 r} e^{ikr} |1+\cos\theta|^2 \qquad (5.2)$$

where θ is the scattered angle. If $\theta = \pi$, E = 0; if $\theta = 0$, E = E_{max}. This leads to efficient forward scattering for nanoantennas when $\theta = 0$ as seen in **Figure 5.4**. These equations are simultaneously solved using a MATLAB nonlinear solver algorithm (Levenberg-Marquardt), a numerical method to obtain the phase of each of the nanoantenna elements. Once the phase of each antenna is known in relation to its nearest neighbors, a library of nanoantenna elements and their corresponding phase shift as a function of neighbors may be assembled. A holographic quantized phase map may then be transformed into a nanoantenna array design that considers dissimilar nearest neighbors.

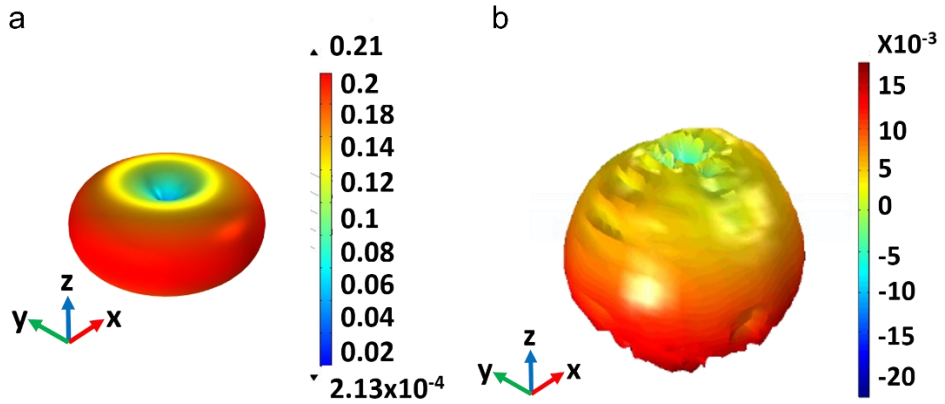

Figure 5.4: ***Far-field radiation plots***

(a). Far-field radiation of an electric field dipole with a torus shape showing a uniformly radiated electric field. (b). Far-field radiation of a dielectric nanoantenna with a cardioid shape. This is typically designed to scatter most of the light in the forward direction while suppressing back scattered radiation, leading to its apple-like shape.

5.4.2 – Nanoantenna Phase Extraction

As stated earlier, the nonlinear equations generated are solved simultaneously for the amplitude and phase of each individual emitter. The inbuilt Levenberg-Marquardt algorithm was used to obtain the unknown values of scattered amplitude and phase. This takes initial guesses for

the unknowns as inputs and solves for the output values. This algorithm has multiple exit conditions for filtering wrong solutions.

We tested a digital experiment to validate the efficacy of this method. This involved using three-point emitters whose amplitude and phase are preset. **Figure 5.5** shows the results obtained from the algorithm. Eleven initial guesses were used and five of them didn't converge to the correct solution and were filtered out using the exit conditions. This method can be applied to nanoantennas in an array to obtain the amplitude and phase of each antenna in the presence of mutual antenna coupling.

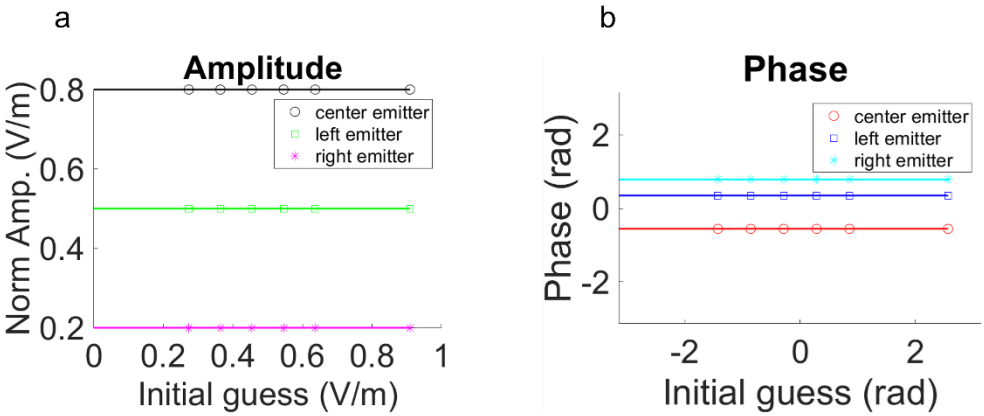

Figure 5.5: Numerical solutions amplitude and phase for three-point emitters

(a). Normalized amplitude solutions obtained by numerical method for three-point emitters. (b). Phase solutions obtained by numerical method for the same three-point emitters. Circle symbols indicate solution results while solid lines indicate exact pre-set values for the original amplitude and phase values.

5.5 – Conclusions and Future Work

In summary, this chapter discusses design and numerical efforts towards accurately obtaining the impinged amplitude and phase from light incident on a nanoantenna array. Progress towards the design of a phase-only hologram has been shown. Using the Gerchberg-Saxton

algorithm, the phase of a chosen image was retrieved using an iterative Fourier transform approach. A path towards obtaining the individual phase values in a nanoantenna array where each nanoantenna was coupled to its nearest neighbor is demonstrated using what is referred to as the triangulation method. This method was tested using three-point emitters and gave accurate results while eliminating incorrect solutions.

Forging ahead, the numerical method demonstrated here for nanoantenna phase extraction from quasi-point sources should be applied to actual metasurface antenna element arrays. Preferably, this could first be applied to simple arrays such as a 2 x 1 array where each nanoantenna is well separated beyond reasonable crosstalk between them. The phase results can be compared with results obtained from COMSOL to confirm that they agree. Next, the method should be applied when the two nanoantennas are brought into proximity of each other. Once these tests have been done, this method could be optimized for larger arrays[137].

Furthermore, optimized designs can be chosen using the coupling figure of merit described in chapter 4. This could aid with the efficient design and encoding of different phase values in each pixel and improve the overall metasurface hologram efficiency.

Chapter 6 – Conclusions and Future Perspectives

This dissertation has been written to give insight into the properties and potential of reconfigurable photonics using dielectric metasurfaces, which is a rapidly growing research area. The ability to tune this diverse resonant platform using various external impulses provides extra degrees of freedom for tailoring the optical responses to yield the desired performance. Due to its exciting physics, this platform could lead to delightful applications in dynamic beam steering, where phase gradient metasurfaces can be deployed, suitable for LIDAR systems. Other interesting uses of this platform include varifocal lensing where the focal length of the lens is tuned by an external stimulus on demand, optical sensing of bulk fluids and biofluids at various temperatures, and so much more. Three applications were explored in-depth in this dissertation: portable and cheap refractive index sensing and biomarker detection; continuously tunable amplitude and phase modulation; and static and tunable holographic displays. These give a taste of the abundant potential that this metasurface platform possesses in engineering photon-matter interactions for exciting, impactful applications.

6.1 – Metasurface-based fluid detection

Chapter 2 discussed dynamic tunability in a Huygens metasurface by modulating the metasurface environment towards obtaining a portable (< 250 $in.^3$) and cheap (<$4000) sensor. The low-cost sensor showed sensitivity to 1.9×10^{-6} change in the bulk fluid refractive index without the use of a spectrometer or other complex optics. Two Mie resonance and one asymmetric

resonance amorphous silicon metasurface on glass were fabricated on the same chip and were used for simultaneous measurements of transmitted optical response due to bulk fluid refractive index changes. Furthermore, a 10kDa culture filtrate peptide (CFP-10) biomarker was detected using our sensor testbed with 10 pM resolution.

The relentless effort in academia and industry to pursue Feynman's acclamation that there is "enough room at the bottom" could push further development of the nanophotonic sensor testbed towards sensors with a much smaller form factor at even cheaper costs. For example, it may be possible to develop a smart wearable watch, based on the discussed metasurface-based sensing platform, that detects how much sodium is lost in sweat for active professionals with a high sodium diet vs. active professionals with a lower sodium diet both of whom have no pre-existing conditions. This application could spread across a broader demography and could lead to further advancements in biomedical research and improved patient outcomes.

In addition, the described biosensor can be further modified to allow for sensing multiple biomarkers simultaneously. Alternatively, it could be miniaturized into a small household self-diagnosis kit for early detection of infectious diseases. This could be useful in developing countries where access to primary health care might be restricted. Replacing component parts such as the device computer with microcontrollers or direct connection to a smartphone could reduce the scale of the device further for compact deployment and easy use.

6.2 – Continuous optical wavefront tuning

Chapter 3 of this dissertation described the utilization of metasurfaces based on a phase change material, vanadium dioxide (VO_2), to achieve continuous tuning of the amplitude and the

phase of the impinging light wave as the material is tuned between its structural phases. Spectrally overlapping resonances are excited at near infrared wavelengths and higher order resonances are excited at shorter wavelengths. By tuning the material's optical properties from its insulating phase to its metallic phase, we obtain large amplitude modulation (extinction ratio - ~19 dB) with little residual phase modulation (~35^{o}) at 1920 nm. Also, a large phase modulation (~228^{o}) was obtained at 1676 nm with a little amplitude modulation (extinction ratio - ~4 dB).

Going forward, tunable beam deflecting metasurfaces could be realized using this metasurface platform, which is applicable in beam steering systems useful for autonomous vehicles. This can be achieved by using "supercells" of spatially homogenous metasurfaces which could define each puzzle piece for the pixelated metasurface. By slowly tuning the temperature, electric field, or impinging photons on the metasurface, we can gradually change the direction of the steered beam in a continuous and reversible manner. This design concept is also useful in more complex optical setups like lenses and holograms.

Furthermore, VO_2 metasurfaces can be designed for visible wavelength applications centered around the excitonic resonances of two-dimensional dichalcogenides like MoS_2 to investigate the coupling between Mie resonances in VO_2 and excitonic resonances in MoS_2. By thermally tuning the refractive index of VO_2, the excitonic resonances could blue shift, red shift, or decay. This might be useful for the implementation of tunable optical metasurface switches. In addition, these metasurfaces could be used for optical sensing at high temperatures (above room temperature) by exploiting the near field enhancement of plasmonic resonances in the metallic phase of VO_2.

6.3 – Tailoring mutual coupling in metasurfaces

Chapter 4 of this dissertation studied the characterization of the intensity of the local field mutual coupling between nearest neighbor antennas in an array. An equation for the coupling figure of merit (FOM) was proposed and tested across three different dielectric Huygens metasurface designs. The nanodonut design, with a coupling FOM of 0.42 came closest to the ideal design which will have a coupling FOM of zero. For experimental validation, beam deflectors were designed and fabricated for each of the three metasurface geometries studied. The highest beam deflecting efficiency of ~65% was achieved in the disk design. The donut design contained some elements whose transmittance values were not close to unity and could have adversely impacted its beam deflecting efficiency.

Marching on, extending the coupling figure of merit beyond Huygens metasurfaces will lead to a robust method for estimating coupling in metasurfaces and potentially enable unprecedented novel and intuitive designs for efficient optical performance. The coupling FOM can also be incorporated into the process tree of a metasurface design framework which could lead to a quicker turnaround in making design decisions. This process tree could include different design optimization methods such as deep neural networks, statistical optimization, and inverse design that score metasurface geometries according to this FOM.

6.4 – Towards tunable metasurface holograms

Chapter 5 of this dissertation discusses efforts towards making dynamically tunable holograms. A phase map for the intended holographic image is obtained from its intensity map using the Gerchberg-Saxton algorithm. A non-linear solver was used to obtain the phase-

nanoantenna map in the presence of nearest neighbor coupling. The non-linear solver algorithm was tested on a system of three-point emitters whose amplitude and phase information are known, and it yielded accurate results.

Although the tunable metasurface hologram was not yet experimentally realized as at the time of writing, achieving this would be a huge breakthrough in next generation display technology. It will be beneficial to test for the computational cost for accurately obtaining phase and amplitude information using the non-linear solver described in chapter 5. Also, for large area holographic displays, a compression algorithm like METAC (used for large area lensing) can be deployed to make computation easier and more efficient[137].

6.5 – Final perspective

It has been an interesting and rewarding experience putting together this contribution to aid further comprehension of practical applications of dynamic tunability in dielectric Huygens metasurfaces. Due to the explosive ongoing research and technological advancements in this field, it will be no surprise to see some full-scale deployment of tunable metasurfaces in cameras, sensors, and displays in the world around us. This ongoing progress will simultaneously pave the way for greater understanding of fundamental light-matter interactions at the nanoscale.

Appendix A: Related Publications and Presentations

7.1 – Journal Publications

IO Oguntoye, BK Simone, S Padmanabha, GZ Hartfield, P Amrollahi, TY Hu, AJ Ollanik, MD Escarra, ***ACS Applied Nano Materials*** **(2022)** Silicon Nanodisk Huygens Metasurfaces for Portable and Low-Cost Refractive Index and Biomarker Sensing.

IO Oguntoye, S Padmanabha, M Hinkle, T Koutougeras, AJ Ollanik, MD Escarra, (2022) "Continuously Tunable Amplitude and Phase Modulation with Vanadium Dioxide Metasurfaces", *in preparation*.

IO Oguntoye, S Padmanabha, M Hinkle, AJ Ollanik, MD Escarra, (2022) "Engineering Nearest Neighbor Crosstalk in Huygens Metasurfaces", *in preparation.*

IO Oguntoye, T Koutsougeras, S Padmanabha, M Hinkle, MD Escarra (2022) "Synthesis and Characterization of Vanadium Dioxide Thin Films for Photonic Applications", *in preparation.*

AJ Ollanik, **IO Oguntoye,** Y Ji, MD Escarra, ***Journal of Optical Society of America (B)*** **(2021)** Resonance tuning for dynamic Huygens metasurfaces.

KM Islam, R Synowicki, T Ismael, **I Oguntoye**, N Grinalds, MD Escarra, ***Advanced Photonics Research*** **(2021)** In-Plane and Out-of-Plane Optical Properties of Monolayer, Few-Layer, and Thin-Film MoS2 from 190 to 1700 nm and Their Application in Photonic Device Design.

AJ Ollanik, **IO Oguntoye**, GZ Harfield, MD Escarra, ***Advanced Material Technologies*** **(2019)** Highly Sensitive, Affordable, and Adaptable Refractive Index Sensing with Silicon-Based Dielectric Metasurfaces.

7.2 – Conference Proceedings

S Padmanabha, **IO Oguntoye,** J Franz, J Myers, R Bekele, A Clabeau, V Nguyen, J Sanghera, MD Escarra, ***CLEO: Applications and Technology,*** **(2022)** Reconfigurable Metalenses based on Antimony Trisulfide (Sb_2S_3) Phase Change Material.

IO Oguntoye, S Padmanabha, T Koutsougeras, M Hinkle, MD Escarra, ***CLEO: QELS_Fundamental Science,*** **(2022)** Design and Fabrication of Vanadium Dioxide Metasurfaces for Continuous Optical Wavefront Tuning.

IO Oguntoye, S Padmanabha, AJ Ollanik, MD Escarra, ***CLEO: QELS_Fundamental Science,*** **(2021)** Engineering Nearest Neighbor Coupling in Huygens Metasurfaces.

S Padmanabha, **IO Oguntoye,** J Franz, J Myers, R Bekele, A Clabeau, MD Escarra, ***CLEO: Applications and Technology,*** **(2021)** Photonic Modulation Using Antimony-Trisulphide Phase Change Huygens Metasurfaces.

IO Oguntoye, AJ Ollanik, S Padmanabha, GZ Hartfield, BK Simone, MD Escarra ***CLEO: QELS_Fundamental Science,*** **(2020)** Dynamically Tunable Amplitude and Phase Modulation Using Vanadium Dioxide Huygens Metasurfaces.

BK Simone, **IO Oguntoye**, GZ Hartfield, S Padmanabha, AJ Ollanik, MD Escarra ***CLEO: QELS_Fundamental Science*****, (2020)** Design and Prototyping of a Portable Metasurface-Based Refractive Index Sensor.

I Oguntoye, A Ollanik, Y Ji, G Hartfield, MD Escarra - ***CLEO: Science and Innovations,*** **(2019)** Towards high efficiency, dynamically tunable metaholograms.

7.3 – Other Presentations

T Koutsougeras, **IO Oguntoye**, S Padmanabha, M Hinkle, MD Escarra, ***EIPBN,*** **(2022),** Continuously Tunable Vanadium Dioxide Metasurfaces for Active Optical Wavefront Control.

IO Oguntoye, S Padmanabha, Y Ji, AJ Ollanik, MD Escarra, ***EIPBN,*** **(2021),** Fabrication of Dynamically Tunable Vanadium Dioxide Huygens Metasurfaces for Optical Modulation.

IO Oguntoye, S Padmanabha, MD Escarra, ***Physics and Engineering Physics Summer Research Colloquium,*** **(2021),** Manipulating Nearest Neighbor Coupling in Huygens Metasurfaces.

IO Oguntoye, S Padmanabha, Z Hartfield, B Simone, MD Escarra, ***Physics and Engineering Physics Summer Research Colloquium,*** **(2020),** Vanadium Dioxide Huygens Metasurfaces for Dynamically Tunable Optical Modulation.

IO Oguntoye, S Padmanabha, B Simone, MD Escarra, ***Physics and Engineering Physics Summer Research Colloquium,*** **(2019),** All-Dielectric Huygens' Metasufaces: Sensing and Switching

IO Oguntoye, AJ Ollanik, Y Ji, Z Hartfield, MD Escarra, ***Physics and Engineering Physics Summer Research Colloquium,*** **(2018),** Progress towards tunable metaholograms

Appendix B

8.1 – Supplementary information for Chapter 2

8.1.1 – Geometric parameters

Dimensions	Mie Resonance Nanodisks	Asymmetric Resonance Nanocylinders
Height	190 nm	190 nm
Diameter	330 nm	240 nm
Edge to Edge Spacing	251 nm	415 nm

Table 8.1: Modeled amorphous silicon metasurface dimensions

8.1.2 – Circuit Design and Methodology

A stack of voltage regulators and dividers as well as the laser driver is used to fix the output power of the laser beam. The laser beam is incident on the measurement chip and the transmitted signal is collected on a 4-quadrant photodetector represented by $V_1 – V_4$. These are collected by the 4-channel datalogger connected to a computer for on demand viewing and data analysis.

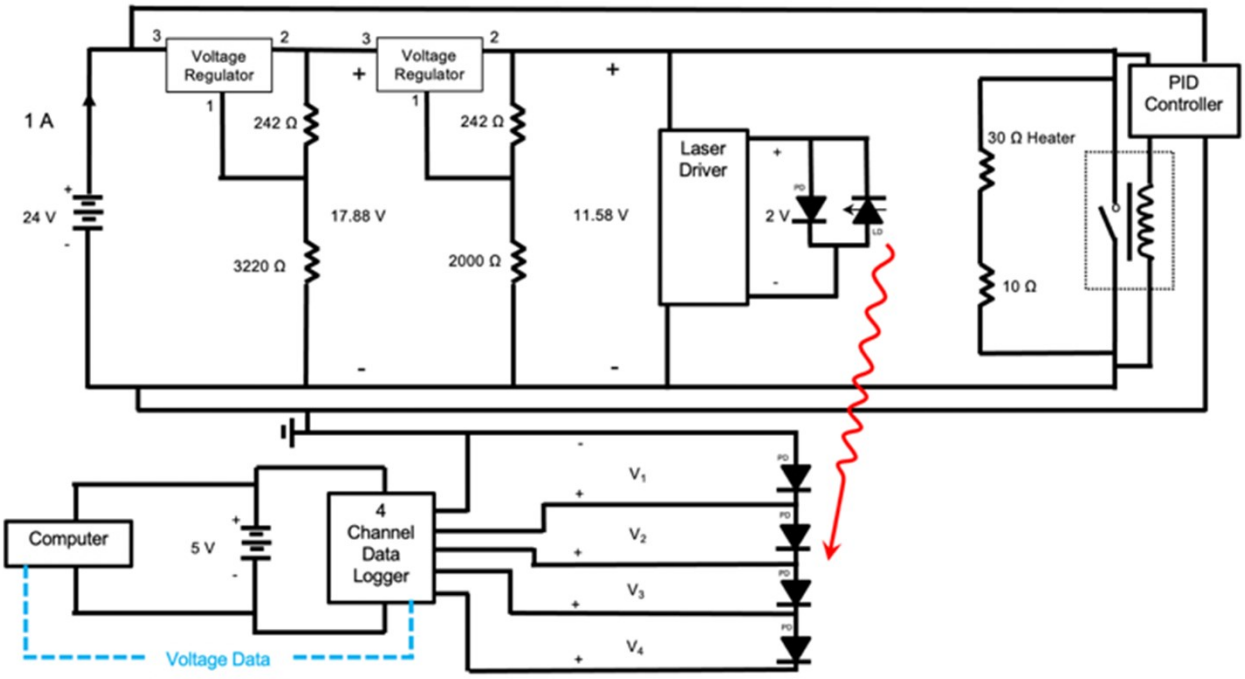

Figure 8.1: Electronic circuitry for sensor operation

Component	Purpose	Vendor	Part #	Amount	Unit Cost ($)	Total Cost QTY1 ($)
Quadrant Photodiode	Detector	Mouser	QP5.8-6-TO5	1	44.54	44.54
Transistor Socket	Interface with detector	DigiKey	ED2152-ND	1	1.84	1.84
Laser Diode	Laser	Thorlabs	L980P010	1	28.95	28.95
Adjustable Collimation Tube	Collimate laser	Thorlabs	LTN330-B	1	244.79	244.79
ESD Protection & Strain Relief Cable	Electrical protection for laser	Thorlabs	SR9A-DB9	1	55.95	55.95
Temperature PID Controller	Controls temperature	Omega	CN16D3-M-DC	1	85.00	85.00
USB Data Logger	Records voltage	CAS Dataloggers	-	1	2,665.00	2,665.00

Custom Enclosure	Seal out light	Protocase	-	1	218.05	218.05
Corner Machine Bracket	Sample door	McMaster	2313N15	1	9.80	9.80
Steel Corner Bracket	Mount drawers	McMaster	1556A24	2	0.43	0.86
Flat-Surface Machine Bracket	Mount drawers	McMaster	2312N33	1	5.11	5.11
Miniature Drawer Slides	Access sample	McMaster	3351N11	1	26.13	26.13
Tubing Union Assembly	Access tubing	Idex-hs	P-630	2	10.99	21.98
Quick-Turn Tube Coupling	Syringe connection	McMaster	51525K317	1	15.48	1.55
Vibration-Damping Mount	Feet for enclosure	Mcmaster	60525K21	4	4.13	16.52

Dovetail Rail 6"	Align optics	Thorlabs	RLA0600	1	45.72	45.72
Dovetail Rail Carrier	Mount optics	Thorlabs	RC1	2	26.94	53.88
1/2" Post Holder 1" Length	Mount optics	Thorlabs	PH1	2	7.24	14.48
Optical Post 1" Length	Mount optics	Thorlabs	TR1	2	4.88	9.76
Cage Plate 1" Dia.	Mount laser	Thorlabs	CP33	1	16.39	16.39
Mirror Mount	Mount detector	Thorlabs	MFM10	1	26.52	26.52
Laser Mount Adapter	Mount laser	Thorlabs	AD15F	1	33.00	33.00
SCR	Relay for PID	Mouser	TN3015H-6T	1	1.20	1.20
Circuit Board	Connect electronics	McMaster	1305N11	1	6.96	6.96

PCB Standoffs	Mount PCB	Mcmaster	91443A220	1	5.05	2.02
USB Adapter	Access data logger	McMaster	1423N8	1	23.04	23.04
USB Cord	Data logger-computer	McMaster	4974T77	1	16.67	16.67
Barrel-Style DC Connector	Access power supply	Mcmaster	8320N118	1	1.06	1.06
Adapter Cord	AC to DC	McMaster	70235K934	1	14.84	14.84
Friction Hinge	For door	McMaster	1467A4	1	3.60	3.60
Constant Power LD Driver	Power laser	Thorlabs	LD1100	1	98.75	98.75
U-Channel, Aluminum 6063	Mount heater & stage	McMaster	9001K802	1	8.99	8.99

Z-Bar, Aluminum 6061	Hold sample	McMaster	7062T11	1	3.16	0.79
Miniature Snap-Acting Switch	Interlock	McMaster	7779K12	1	4.93	0.00
Voltage Regulator	Power heater & laser	Amazon	L7812CV	1	6.49	2.60
Black out foam	Light-tight edges	Amazon	R534H	1	2.93	0.293
Black Acrylic Paint	Anti reflection	Walmart	21885EX	1	0.50	0.01
Relay	Heater Circuit	Mouser	OSA-SH-224DM5	1	2.41	2.41

Tygon Tubing	Microfluidics	Darwin-Microfluidics	LVF-KTU-13	1	73.79	2.24
24-gauge wire	Electronics	DigiKey	2183-2634-ND	1	4.75	0.16
Electrical Headers	Electonics	DigiKey	528-2947-ND	4	1.25	5.00
Black Foam Core Board	Light Tight	Uline	n/a	1	4.40	0.09
1/4"-20 Screws	Mounting Optics	Thorlabs	SH25S038	1	8.27	0.66
8-32 Screws	Sample Stage	Thorlabs	SH8S025	1	6.65	0.27
4-40 Screws	Sample Stage	Thorlabs	SH4S038	1	8.87	0.71
Washers	Sample Stage	Thorlabs	W8S038	1	3.59	0.25
4-40 Nuts	Sample Stage	Grainger Industries	2GA51	1	2.09	0.04

12.7 mm Dovetail Translation	Stage motion control	Thorlabs	DT12/M	2	84.14	168.28
Wafer-scale nanoimprint Lithography[138]	Sensor Platform			1	7.50	7.50
TOTAL PER UNIT						3,994.25

Table 8.2: Sensor bill of materials

Appendix C

9.1 – Supplementary Information for Chapter 3

9.1.1 – VO_2 Metasurface Design Geometries

Geometry	Height (nm)	Diameter (nm)	Unit Cell (nm)
Disks	394	882	1162
Donut[a]	310	1020	1275
Silicon in VO_2 disks	235	880	1270
Split ring and bar[b]	430	845	1185
Holes	480	870	1110

Table 9.1: Modeled dimensions of VO_2 metasurfaces

[a] The donut geometry has an inner diameter of 89.9 nm.

[b] The bar in the split ring and bar geometry has a length of 600 nm and a width of 150 nm.

9.1.2 – VO_2 Metasurface Fabrication Protocol

- VO_2 Thin Film Growth
  - Substrate sanitized using acetone, isopropyl alcohol (IPA), and in pre-sputtering process with Ar plasma (Parameters for pre-sputtering process are RF Power: 30 W, Pressure: 30 mTorr, Time: 5 minutes)
  - V_xO_y is sputtered onto the substrate (Sputtering parameters are RF Power: 200 W, Base Pressure: $\leq 1.2 \times 10^{-6}$ Torr, Deposition Pressure: 3.3 mTorr, Deposition rate: ~0.31 -

0.36 Å/s). Note that the power must be ramped up slowly at a rate of 1 W/s or less (since this target is an insulating target) to avoid thermal shocks that can lead to cracks in the insulating target.

- Sputtered film is annealed in a 1" quartz tube. Annealing parameters are Base Pressure: ~15 mTorr, Annealing temperature: 500 ^{o}C, Average ramp rate: 7.95 ^{o}C/min., Steady temperature: 500 ^{o}C, Annealing time: 60 mins. Gas flow: 0 sccm (no gas flow during annealing). Note that sample is placed on a ceramic boat in the upstream zone of the hot wall tube furnace. Also, the tube furnace should be allowed to cool down naturally to room temperature to prevent soft flaking of the surface layer of the annealed film.

❖ VO_2 Metasurface Fabrication

- SiO_2 electron beam evaporated onto sample. SiO_2 thickness should be 1.5x – 2x the VO_2 thickness for a successful future etch. The SiO_2 acts as the hard mask during the VO_2 etch. SiO_2 deposition is done in manual deposition mode. SiO_2 is moisture-sensitive and could flake off if humidity is high in the chamber. Gettering can be done using titanium or chromium to trap water vapor down and reduce the moisture content of the vacuum chamber before deposition. When gettering is done, the shutter should be closed to prevent metallic deposition on sample.
- Carbon coating is done on the sample. This is useful for charge dissipation during electron beam lithography and helps to protect the underlying SiO_2 layer from flaking off due to moisture-induced adsorption.
- Negative electron beam resist (ma-N 2403) is spun onto the sample. Spin coating parameters are the following: Step 1 (Spin): 500 rpm for 5 s at 1200 rpm/s. Step 2 (Spread): 3000 rpm for 35s at 1200 rpm/s. Two layers of ma-N 2403 are spun on the

sample to achieve a thickness of ~ 600 nm. The resist acts as a soft mask in a future etch step (SiO_2 etch) and it is critical to have enough resist material to prevent etching unwanted areas of the sample.

- Electron beam lithography is done on the sample to write the metasurface pattern through the resist. Parameters are Dose: 200 $\mu C/cm^2$.
- Resist development is done using ma – D 525 for 1 minute and rinsed in deionized water for 4 – 5 minutes.
- Reactive ion etching is done on the sample to remove unpatterened SiO_2 layer. The electron beam resist acts as a soft mask for the SiO_2 cylinders. Parameters are ICP power: 1000 W, RIE power: 250 W, Chamber pressure: 30 mTorr, CHF_3 flow rate: 12 sccm, Argon flow rate: 38 sccm, Etch rate: 55 – 60 nm/min.
- Resist removal is done on the sample to remove residual resist using Remover – PG solvent at 80 ^oC for 10 minutes. The sample is then transferred to another remover solvent bath at 80 ^oC for 10 minutes. Then the sample is rinsed in deionized water.
- Reactive ion etching is done on the sample to remove unpatterned VO_2 layer using chlorine and argon gases. Recipe is as follows: ICP power: 700 W, RIE power: 250 W, Chamber pressure: 7 mTorr, Cl_2 flow rate: 60 sccm, Ar flow rate: 180 sccm, Etch rate: ~5-10 nm/min, Substrate temperature: ~100 ^oC.
- The sample is then encapsulated in PDMS via spin coating. Process parameters are the following: Step 1 (Spin): 500 rpm for 5 s at 1200 rpm/s. Step 2 (Spread): 7000 rpm for 5 minutes at 1200 rpm/s. This yields a thickness of about 3 μm which is at least one wavelength away from the nanoantennas for most of the wavelengths of interest. Some SiO_2 residue could remain after the VO_2 etch. As shown from some model (see **Figure**

9.1 below), this should not change the performance of the already simulated VO_2 metasurface.

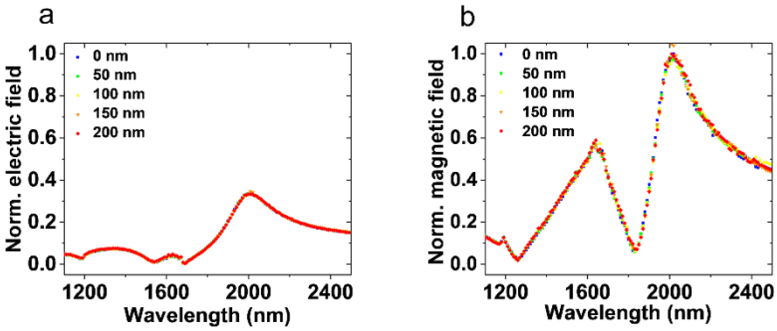

Figure 9.1: Effect of residual SiO_2 layer on VO_2 metasurface

(a). Normalized electric field confined in the VO_2 nanodisks (b). Normalized magnetic field confined in the VO_2 nanodisks. Both plots are normalized to the magnetic field strength of the VO_2 nanodisks with no residual SiO_2 layer on them.

Appendix D

10.1 – Supplementary Information for Chapter 4

10.1.1 – Nanodisk Beam Deflector Geometry

Nanodisk Element	1	2	3	4	5	6	7	8
D_x (nm)	570	570	570	570	570	570	570	570
D_y (nm)	300	450	520	560	590	630	690	780

Table 10.1: Array parameters for Figure 4.6a, λo=1550 nm

Other important parameters include height = 255 nm, Unit cell periodicity (in both x and y directions) = 858 nm.

10.1.2 – Nanodonut Beam Deflector Geometry

Nanodonut Element	1	2	3	4	5	6	7	8
ID_x (nm)	600	131.25	131.25	193.75	131.25	162.5	162.5	225
ID_y (nm)	600	100	102.5	100	256.3	225	318.8	537.5

Table 10.2: Array parameters for Figure 4.6b, λo=1550 nm

Other important parameters include height = 240 nm, Unit cell periodicity (in both x and y directions) = 930 nm.

10.1.3 – Nanobeignet Beam Deflector Geometry

Nanobeignet Element	1	2	3	4	5	6	7	8
D_x (nm)	540	540	540	540	540	540	540	540
D_y (nm)	330	450	500	530	550	570	600	660

Table 10.3: Array parameters for Figure 4.6c, λo=1550 nm

Other important parameters include height = 260 nm, Unit cell periodicity (in both x and y directions) = 825 nm, Fillet radius = 43.2 nm.

References

1. Maksymov, I. S., Staude, I., Miroshnichenko, A. E. & Kivshar, Y. S. Optical yagi-uda nanoantennas. *Nanophotonics* **1**, 65–81 (2012).

2. Cai, W. & Shalaev, V. *Optical metamaterials: Fundamentals and applications*. *Optical Metamaterials: Fundamentals and Applications* (Springer New York, 2010). doi:10.1007/978-1-4419-1151-3.

3. Barber, d. J. & freestone, i. C. An investigation of the origin of the colour of the lycurgus cup by analytical transmission electron microscopy. *Archaeometry* **32**, 33–45 (1990).

4. Jagadis Chunder Bose. On the rotation of plane of polarization of electric wave by a twisted structure. *Proc. R. Soc. London* **63**, (1898).

5. Smith, D. R., Padilla, W. J., Vier, D. C., Nemat-Nasser, S. C. & Schultz, S. Composite Medium with Simultaneously Negative Permeability and Permittivity. *Phys. Rev. Lett.* **84**, 4184–4187 (2000).

6. Pendry, J. B. Negative Refraction Makes a Perfect Lens. *Phys. Rev. Lett.* **85**, 3966 (2000).

7. Gonano, C. A. A perspective on metasurfaces, circuits, holograms and invisibility. (Polytecnico di Milano, 2015).

8. Hsiao, H.-H., Chu, C. H. & Tsai, D. P. Fundamentals and Applications of Metasurfaces. *Small Methods* **1**, 1600064 (2017).

9. Zou, C., Staude, I. & Neshev, D. N. *Tunable metasurfaces and metadevices*. *Dielectric Metamaterials* (Elsevier Ltd, 2020). doi:10.1016/b978-0-08-102403-4.00012-8.

10. Cheng, J., Jafar-Zanjani, S. & Mosallaei, H. All-dielectric ultrathin conformal metasurfaces: Lensing and cloaking applications at 532 nm wavelength. *Sci. Rep.* **6**, 1–5 (2016).

11. Kamali, S. M., Arbabi, A., Arbabi, E., Horie, Y. & Faraon, A. Decoupling optical function and geometrical form using conformal flexible dielectric metasurfaces. *Nat. Commun. 2016 71* **7**, 1–7 (2016).

12. Simone, B. K. *et al.* Design and Prototyping of a Portable Metasurface-Based Refractive Index Sensor. in *Conference on Lasers and Electro-Optics* FF3E.5 (Optical Society of America, 2020).

13. Wu, J. *et al.* On-Chip Optical Gas Sensors Based on Group-IV Materials. *ACS Photonics* **7**, 2923–2940 (2020).

14. Duarte, D. P., Nogueira, R. N. & Bilro, L. B. A low-cost liquid refractive index sensor based on plastic optical fibre and CCD array. *Meas. Sci. Technol.* **31(4)**, 047001 (2020).

15. Xu, Y. *et al.* Optical Refractive Index Sensors with Plasmonic and Photonic Structures: Promising and Inconvenient Truth. *Adv. Opt. Mater.* **7(9)**, 1801433 (2019).

16. Chen, Z., Liu, L., He, Y. & Ma, H. Resolution enhancement of surface plasmon resonance sensors with spectral interrogation: resonant wavelength considerations. *Appl. Opt.* **55**, 884 (2016).

17. Pfeifer, P., Aldinger, U., Schwotzer, G., Diekmann, S. & Steinrücke, P. Real time sensing of specific molecular binding using surface plasmon resonance spectroscopy. *Sensors Actuators, B Chem.* **54**, 166–175 (1999).

18. Liu, L. *et al.* Parallel scan spectral surface plasmon resonance imaging. *Appl. Opt.* **47**, 5616–

5621 (2008).

19. Chen, H., Kou, X., Yang, Z., Ni, W. & Wang, J. Shape- and size-dependent refractive index sensitivity of gold nanoparticles. *Langmuir* **24**, 5233–5237 (2008).

20. Mock, J. J., Smith, D. R. & Schultz, S. Local refractive index dependence of plasmon resonance spectra from individual nanoparticles. *Nano Lett.* **3**, 485–491 (2003).

21. Martinsson, E., Otte, M. A., Shahjamali, M. M., Sepulveda, B. & Aili, D. Substrate Effect on the Refractive Index Sensitivity of Silver Nanoparticles. *J. Phys. Chem. C* **118**, 6 (2014).

22. Wang, L. J., Li, Y. H. & Xu, Z. Y. Long-period grating inscription on polymer functionalized optical microfibers and its applications in optical sensing. *Photonics Res.* **4**, 45–48 (2016).

23. Belushkin, A., Yesilkoy, F. & Altug, H. Nanoparticle-Enhanced Plasmonic Biosensor for Digital Biomarker Detection in a Microarray. *ACS Nano* **12**, 4453–4461 (2018).

24. Prasad, A., Choi, J., Jia, Z., Park, S. & Gartia, M. R. Nanohole array plasmonic biosensors: Emerging point-of-care applications. *Biosens. Bioelectron.* **130**, 185–203 (2019).

25. Yavas, O., Svedendahl, M., Dobosz, P., Sanz, V. & Quidant, R. On-a-chip Biosensing Based on All-Dielectric Nanoresonators. *Nano Lett.* **17**, 4421–4426 (2017).

26. Jason-Moller, L., Murphy, M. & Bruno, J. A. Overview of Biacore systems and their applications. *Curr. Protoc. protein Sci.* **45**, 19–13 (2006).

27. Ding, J. F., Zhang, A. P., Shao, L. Y., Yan, J. H. & He, S. Fiber-taper seeded long-period grating pair as a highly sensitive refractive-index sensor. *IEEE Photonics Technol. Lett.* **17**, 1247–1249 (2005).

28. Agarwal, A., Hu, J., Kimerling, L. C. & Sun, X. Design guidelines for optical resonator biochemical sensors. *JOSA B* **26**, 1032–1041 (2009).

29. Oh, S.-H. *et al.* Nanophotonic biosensors harnessing van der Waals materials. *Nat. Commun.* **12**, 3824 (2021).

30. Tseng, M. L., Jahani, Y., Leitis, A. & Altug, H. Dielectric Metasurfaces Enabling Advanced Optical Biosensors. *ACS Photonics* **8(1)**, 47–60 (2021).

31. Barth, I., Conteduca, D., Reardon, C., Johnson, S. & Krauss, T. F. Common-path interferometric label-free protein sensing with resonant dielectric nanostructures. *Light Sci. Appl.* **9(1)**, 1–9 (2020).

32. *Global tuberculosis report 2020. Geneva: World Health Organization; 2020. Licence: CC BY-NC-SA 3.0 IGO*. (2020).

33. Bontempi, N. *et al.* Highly sensitive biosensors based on all-dielectric nanoresonators. *Nanoscale* **9**, 4972–4980 (2017).

34. Triggs, G. J. *et al.* Chirped guided-mode resonance biosensor. *Optica* **4**, 229 (2017).

35. Shamkhi, H. K. *et al.* Transverse scattering and generalized kerker effects in all-dielectric mie-resonant metaoptics. *Phys. Rev. Lett.* **122**, 1–6 (2019).

36. Yu, N. *et al.* Flat Optics: Controlling Wavefronts With Optical Antenna Metasurfaces. *IEEE J. Sel. Top. Quantum Electron.* **19**, 4700423–4700423 (2013).

37. Won, R. Into the 'Mie-tronic' era. *Nat. Photonics* **13**, 585–587 (2019).

38. Kruk, S. & Kivshar, Y. Functional Meta-Optics and Nanophotonics Govern by Mie Resonances. *ACS Photonics* **4**, 2638–2649 (2017).

39. Ollanik, A. J., Oguntoye, I. O., Hartfield, G. Z. & Escarra, M. D. An Affordable, Customizable, and Highly Sensitive Metasurface-Based Refractive Index Sensor. in *Conference on Lasers and Electro-Optics* STh1F.5 (Optical Society of America, 2019).

40. Ollanik, A. J., Oguntoye, I. O., Hartfield, G. Z. & Escarra, M. D. Highly Sensitive, Affordable, and Adaptable Refractive Index Sensing with Silicon-Based Dielectric Metasurfaces. *Adv. Mater. Technol.* **4(2)**, 1800567 (2019).

41. Mehran, M. & Maleki, M. Guided-mode resonance sensors: different schemes for different applications. *JOSA B, Vol. 39, Issue 6, pp. 1634-1643* **39**, 1634–1643 (2022).

42. Liu, Y., Zhou, W. & Sun, Y. Optical Refractive Index Sensing Based on High-Q Bound States in the Continuum in Free-Space Coupled Photonic Crystal Slabs. *Sensors* **17**, 1861 (2017).

43. Kuswandi, B., Nuriman, Huskens, J. & Verboom, W. Optical sensing systems for microfluidic devices: A review. *Anal. Chim. Acta* **601**, 141–155 (2007).

44. Mariani, S., Strambini, L. M. & Barillaro, G. Electrical Double Layer-Induced Ion Surface Accumulation for Ultrasensitive Refractive Index Sensing with Nanostructured Porous Silicon Interferometers. *ACS Sensors* vol. 3 595–605 (2018).

45. Grahame, D. C. The electrical double layer and the theory of electrocapillarity. *Chem. Rev.* **41**, 441–501 (1947).

46. Tan, C. Y. & Huang, Y. X. Dependence of Refractive Index on Concentration and Temperature in Electrolyte Solution, Polar Solution, Nonpolar Solution, and Protein Solution. *J. Chem. Eng. Data* **60**, 2827–2833 (2015).

47. Heller, W. Refractive Index Mixture. *J. Phys. Chem.*. **69**, 1123–1129 (1965).

48. Ma, Z., Guan, Y. & Liu, H. Superparamagnetic silica nanoparticles with immobilized metal affinity ligands for protein adsorption. *J. Magn. Magn. Mater.* **301**, 469–477 (2006).

49. Wang, Y. & Ferrari, M. Surface modification of micromachined silicon filters. *J. Mater. Sci.* **35**, 4923–4930 (2000).

50. Bhowmik, K., Pramanik, S., Medda, S. K. & De, G. Covalently functionalized reduced graphene oxide by organically modified silica: A facile synthesis of electrically conducting black coatings on glass. *J. Mater. Chem.* **22**, 24690–24697 (2012).

51. Bariana, M., Aw, M. S., Kurkuri, M. & Losic, D. Tuning drug loading and release properties of diatom silica microparticles by surface modifications. *Int. J. Pharm.* **443**, 230–241 (2013).

52. Salimi, K., Usta, D. D., Koçer, İ., Çelik, E. & Tuncel, A. Protein A and protein A/G coupled magnetic SiO2 microspheres for affinity purification of immunoglobulin G. *Int. J. Biol. Macromol.* **111**, 178–185 (2018).

53. Wan, M., Amrollahi, P., Sun, D., Lyon, C. & Hu, T. Y. Using Nanoplasmon-Enhanced Scattering and Low-Magnification Microscope Imaging to Quantify Tumor-Derived Exosomes. *J. Vis. Exp.* 59177 (2019) doi:10.3791/59177.

54. Fu, Y.-L., Deng, C.-S. & Ma, S.-S. Design and analysis of refractive index sensors based on slotted photonic crystal nanobeam cavities with sidewall gratings. *Appl. Opt.* **59**, 896 (2020).

55. Giorgis, F., Descrovi, E., Summonte, C., Dominici, L. & Michelotti, F. Experimental

determination of the sensitivity of Bloch Surface Waves based sensors. *Opt. Express* **18**, 8087 (2010).

56. Di Falco, A., O'Faolain, L. & Krauss, T. F. Chemical sensing in slotted photonic crystal heterostructure cavities. *Appl. Phys. Lett.* **94**, 92–95 (2009).

57. Hu, J. *et al.* Demonstration of chalcogenide glass racetrack microresonators. *Opt. Lett.* **33**, 761 (2008).

58. Bashkatov, A. N. & Genina, E. A. Water refractive index in dependence on temperature and wavelength: a simple approximation. *Saratov Fall Meet. 2002 Opt. Technol. Biophys. Med. IV* **5068**, 393–395 (2003).

59. Harvey, A. H., Gallagher, J. S. & Sengers, J. L. Revised formulation for the refractive index of water and steam as a function of wavelength, temperature and density. *J. Phys. Chem. Ref. Data* **27**, 761–774 (1998).

60. White, I. M. & Fan, X. On the performance quantification of resonant refractive index sensors. *Opt. Express* **16**, 1020–1028 (2008).

61. Chen, X. & Hu, T. Y. Strategies for advanced personalized tuberculosis diagnosis: Current technologies and clinical approaches. *Precis. Clin. Med.* **4**, 35–44 (2021).

62. Dai, Z. *et al.* A multiple-antigen detection assay for tuberculosis diagnosis based on broadly reactive polyclonal antibodies. *Iran. J. Basic Med. Sci.* **20**, 360–367 (2017).

63. Yoon, Y. *et al.* Clogging-free microfluidics for continuous size-based separation of microparticles. *Sci. Rep.* **6(1)**, 1–8 (2016).

64. Maltezos, G. *et al.* Microfluidic blood filtration device. *Biomed Microdevices* **13**, 143–146

(2011).

65. Stern, E. *et al.* Label-free biomarker detection from whole blood. *Nat. Nanotechnol.* **5**, 138–142 (2010).

66. Ollanik, A. J., Smith, J. A., Belue, M. J. & Escarra, M. D. High-Efficiency All-Dielectric Huygens Metasurfaces from the Ultraviolet to the Infrared. *ACS Photonics* **5**, 1351–1358 (2018).

67. Altug, H., Oh, S.-H., Maier, S. A. & Homola, J. Advances and applications of nanophotonic biosensors. doi:10.1038/s41565-021-01045-5.

68. Reverberi, R. & Reverberi, L. Factors affecting the antigen-antibody reaction. *Blood Transfus* **5**, 227–240 (2007).

69. Capasso, F. The future and promise of flat optics: A personal perspective. *Nanophotonics* **7**, 953–957 (2018).

70. Capasso, F. *et al.* Metalenses at visible wavelengths: Diffraction-limited focusing and subwavelength resolution imaging. *Science (80-.).* **352**, 1190–1194 (2016).

71. Ndao, A. *et al.* Octave bandwidth photonic fishnet-achromatic-metalens. *Nat. Commun.* **11**, (2020).

72. Engelberg, J. *et al.* Near-IR wide-field-of-view Huygens metalens for outdoor imaging applications. *Nanophotonics* **9**, 361–370 (2020).

73. Wang, L. *et al.* Grayscale transparent metasurface holograms. *Optica* **3**, 1504 (2016).

74. Ansari, M. A. *et al.* A Spin-Encoded All-Dielectric Metahologram for Visible Light. *Laser Photonics Rev.* **13**, (2019).

75. Zheng, G. *et al.* Metasurface holograms reaching 80% efficiency. *Nat. Nanotechnol.* **10**, 308–312 (2015).

76. Oguntoye, I. O. *et al.* Silicon Nanodisk Huygens Metasurfaces for Portable and Low-Cost Refractive Index and Biomarker Sensing. *ACS Appl. Nano Mater.* acsanm.1c04443 (2022) doi:10.1021/ACSANM.1C04443.

77. Gutruf, P. *et al.* Mechanically tunable dielectric resonator metasurfaces at visible frequencies. *ACS Nano* **10**, 133–141 (2016).

78. Ollanik, A. J., Oguntoye, I., Ji, Y. & Escarra, M. D. Resonance tuning for dynamic Huygens metasurfaces. *J. Opt. Soc. Am. B* **38**, C105 (2021).

79. Cui, T., Bai, B. & Sun, H. Tunable Metasurfaces Based on Active Materials. **1806692**, 1–14 (2019).

80. Simpson, R. E., Yang, J. K. W. & Hu, J. Are phase change materials ideal for programmable photonics?: opinion. *Opt. Mater. Express* **12**, 2368 (2022).

81. Zhang, Y. *et al.* Broadband transparent optical phase change materials for high-performance nonvolatile photonics. *Nat. Commun. 2019 101* **10**, 1–9 (2019).

82. Hallman, K. A., Miller, K. J., Baydin, A., Weiss, S. M. & Haglund, R. F. Sub-Picosecond Response Time of a Hybrid VO2:Silicon Waveguide at 1550 nm. *Adv. Opt. Mater.* **9**, (2021).

83. Jung, Y. *et al.* Integrated Hybrid VO2–Silicon Optical Memory. *ACS Photonics* **9**, 217–223 (2022).

84. Yang, Z., Ko, C. & Ramanathan, S. Oxide Electronics Utilizing Ultrafast Metal-Insulator

Transitions. *Annu. Rev. Mater. Res.* **41**, 337–67 (2011).

85. Kim, Y. *et al.* Phase Modulation with Electrically Tunable Vanadium Dioxide Phase-Change Metasurfaces. *Nano Lett* **19**, 3961–3968 (2019).

86. Mou, N., Tang, B., Li, J., Dong, H. & Zhang, L. Switchable ultra-broadband terahertz wave absorption with VO 2-based metasurface. *Sci. Reports* | **12**, 2501 (123AD).

87. Ge, J., Zhang, Y., Dong, H. & Zhang, L. Nanolayered VO2-Based Switchable Terahertz Metasurfaces as Near-Perfect Absorbers and Antireflection Coatings. *ACS Appl. Nano Mater.* **5**, 5569–5577 (2022).

88. Butakov, N. A. *et al.* Switchable Plasmonic-Dielectric Resonators with Metal-Insulator Transitions. *ACS Photonics* **5**, 371–377 (2018).

89. Kepič, P. *et al.* Optically Tunable Mie Resonance VO2Nanoantennas for Metasurfaces in the Visible. *ACS Photonics* **8**, 1048–1057 (2021).

90. Kang, T. *et al.* Large-scale, power-efficient Au/VO2active metasurfaces for ultrafast optical modulation. *Nanophotonics* **10**, 909–918 (2020).

91. Zanotto, S., Morichetti, F. & Melloni, A. Fundamental limits on the losses of phase and amplitude optical actuators. *Laser Photonics Rev.* **9**, 666–673 (2015).

92. Cueff, S. *et al.* VO2 nanophotonics. *APL Photonics* **5**, (2020).

93. Cardin, A., Fan, K. & Padilla, W. Role of loss in all-dielectric metasurfaces. *Opt. Express, Vol. 26, Issue 13, pp. 17669-17679* **26**, 17669–17679 (2018).

94. Variable Fiber Optical Attenuators, Single Mode. https://www.thorlabs.com/newgrouppage9.cfm?objectgroup_id=6161.

95. Falcone, F. *et al.* Babinet principle applied to the design of metasurfaces and metamaterials. *Phys. Rev. Lett.* **93**, (2004).

96. Vu, T. D. *et al.* Physical vapour deposition of vanadium dioxide for thermochromic smart window applications. *J. Mater. Chem. C* **7**, 2121–2145 (2019).

97. Sahana, M. B., Dharmaprakash, M. S. & Shivashankar, S. A. Microstructure and properties of VO2 thin films deposited by MOCVD from vanadyl acetylacetonate. *J. Mater. Chem.* **12**, 333–338 (2002).

98. Guo, B., Wan, D., Ishaq, A., Luo, H. & Gao, Y. Direct synthesis of high-performance thermal sensitive VO2(B) thin film by chemical vapor deposition for using in uncooled infrared detectors. *J. Alloys Compd.* **715**, 129–136 (2017).

99. Wriedt, H. A. The O-V (Oxygen-Vanadium) system. *Bull. Alloy Phase Diagrams* **10**, 271–277 (1989).

100. Robertson, J., Blomdahl, D. & Islam, K. Rapid-throughput solution-based productionof wafer-scale 2D MoS2. *Appl. Phys. Lett* **114**, 163102 (2019).

101. Shi, R. *et al.* Recent advances in fabrication strategies, phase transition modulation, and advanced applications of vanadium dioxide. *Appl. Phys. Rev.* **6**, (2019).

102. Azad, S., Gajula, D., Sapkota, N., Rao, A. & Koley, G. Infrared Transmission Characteristics of Phase Transitioning VO2 on Various Substrates. *Micromachines* **13**, 812 (2022).

103. Quartz single crystal, Z-cut, 10x10x0.5mm, 2sp. https://www.mtixtl.com/SO-Z-101005-S2.aspx.

104. Lee, S., Ivanov, I. N., Keum, J. K. & Nyung Lee, H. Epitaxial stabilization and phase instability of VO 2 polymorphs OPEN. *Sci. Rep.* **6**, (2015).

105. Goodacre, D., Blum, M. & Buechner, C. Water adsorption on vanadium oxide thin films in ambient relative humidity. *J. Chem. Phys* **152**, 44715 (2020).

106. Ham, Y. H. *et al.* Etching characteristics of VO2 thin films using inductively coupled Cl2/Ar plasma. *Jpn. J. Appl. Phys.* **48**, 6–11 (2009).

107. Williams, M. L. CRC Handbook of Chemistry and Physics, 76th edition. *Occup. Environ. Med.* **53**, 504–504 (1996).

108. Ollanik, A. J. *et al.* Characterization of Dynamic and Nanoscale Materials and Metamaterials with Continuously Referenced Interferometry. *Adv. Opt. Mater.* **7**, 1–7 (2019).

109. Kaplan, G. *et al.* Dynamically controlled plasmonic nano-antenna phased array utilizing vanadium dioxide [Invited]. *Opt. Mater. Express, Vol. 5, Issue 11, pp. 2513-2524* **5**, 2513–2524 (2015).

110. Houska, J., Kolenaty, D., Rezek, J. & Vlcek, J. Characterization of thermochromic VO 2 (prepared at 250 °C) in a wide temperature range by spectroscopic ellipsometry. *Appl. Surf. Sci.* **421**, 529–534 (2017).

111. Li, W. W., Yu, Q. & Liang, J. R. Intrinsic evolutions of optical functions,band gap, and higher-energy electronictransitions in VO2 film near the metal-insulator transition region. *Appl. Phys. Lett* **99**, 241903 (2011).

112. Solà-Garcia, M. *et al. Pump-probe cathodoluminescence microscopy*. *arXiv preprint*

http://arxiv.org/abs/2112.03034 (2021).

113. J.L, A. & B.L., D. *Mutual Coupling in Array Antennas*. (1966).

114. An, S. *et al.* Deep Convolutional Neural Networks to Predict Mutual Coupling Effects in Metasurfaces. *Adv. Opt. Mater.* **10**, 2102113 (2022).

115. Arbabi, A., Horie, Y., Ball, A. J., Bagheri, M. & Faraon, A. Subwavelength-thick lenses with high numerical apertures and large efficiency based on high-contrast transmitarrays. *Nat. Commun.* **6:7069**, (2015).

116. Zhao, W. *et al.* Dielectric Huygens' Metasurface for High-Efficiency Hologram Operating in Transmission Mode OPEN. *Sci. Rep.* **6**, (2016).

117. Chong, K. E. *et al.* Efficient Polarization-Insensitive Complex Wavefront Control Using Huygens' Metasurfaces Based on Dielectric Resonant Meta-atoms. *ACS Photonics* **3**, 514–519 (2016).

118. Ollanik, A. J., Smith, J. A., Belue, M. J. & Escarra, M. D. High-Efficiency All-Dielectric Huygens Metasurfaces from the Ultraviolet to the Infrared. *ACS Photonics* **5**, 1351–1358 (2018).

119. Zhelyeznyakov, M. V., Brunton, S. & Majumdar, A. Deep Learning to Accelerate Scatterer-to-Field Mapping for Inverse Design of Dielectric Metasurfaces. *ACS Photonics* **8**, 481–488 (2021).

120. Hsu, L., Dupré, M., Ndao, A., Yellowhair, J. & Kanté, B. Local phase method for designing and optimizing metasurface devices. *Opt. Express* **25**, 24974 (2017).

121. Oguntoye, I., Ollanik, A., Ji, Y., Hartfield, G. & Escarra, M. D. Towards high efficiency,

dynamically tunable metaholograms. in *2019 Conference on Lasers and Electro-Optics, CLEO 2019 - Proceedings* JTh2A-25 (2019).

122. Yu, N. *et al.* Light propagation with phase discontinuities: Generalized laws of reflection and refraction. *Sci.* **334**, 333–337 (2011).

123. Zhang, Q., Li, M., Liao, T. & Cui, X. Design of beam deflector, splitters, wave plates and metalens using photonic elements with dielectric metasurface. *Opt. Commun.* **411**, 93–100 (2018).

124. Gabor D. A New Microscopic Principle. *Nature* **161**, 777–778 (1948).

125. Goodman, J. W. *Introduction to Fourier optics / Joseph W. Goodman, Stanford University.* vol. 4 (W.H. Freeman, 2017).

126. Jiang, Q., Jin, G. & Cao, L. When metasurface meets hologram: principle and advances. *Adv. Opt. Photonics* **11**, 518 (2019).

127. Huang, L., Zhang, S. & Zentgraf, T. Metasurface holography: From fundamentals to applications. *Nanophotonics* **7**, 1169–1190 (2018).

128. Chen, W. T. *et al.* High-Efficiency Broadband Meta-Hologram with Polarization-Controlled Dual Images. *Nano Lett* **14**, 16 (2014).

129. Huang, Y. W. *et al.* Aluminum plasmonic multicolor meta-Hologram. *Nano Lett.* **15**, 3122–3127 (2015).

130. Frese, D. *et al.* Nonlinear Bicolor Holography Using Plasmonic Metasurfaces. *ACS Photonics* **8**, 1013–1019 (2021).

131. Devlin, R. C., Khorasaninejad, M., Chen, W. T., Oh, J. & Capasso, F. Broadband high-

efficiency dielectric metasurfaces for the visible spectrum. *Proc. Natl. Acad. Sci. U. S. A.* **113**, 10473–10478 (2016).

132. Shechtman, Y. *et al.* Phase Retrieval with Application to Optical Imaging. 87–109 (2014) doi:10.1109/MSP.2014.2352673.

133. Fienup, J. R. Phase retrieval algorithms: a comparison. *Appl. Opt.* **21**, 2758 (1982).

134. Gerchberg, R. W. and W. O. S. A practical algorithm for the determination of the phase from image and diffraction plane pictures. *Optik (Stuttg).* **35**, 237 (1972).

135. Fienup, J. R. Phase retrieval algorithms: a comparison. *Appl. Opt. Vol. 21, Issue 15, pp. 2758-2769* **21**, 2758–2769 (1982).

136. Krasnok, A. E., Miroshnichenko, A. E., Belov, P. A. & Kivshar, Y. S. All-dielectric optical nanoantennas. *Opt. Express* **20**, 20599–20604 (2012).

137. She, A., Zhang, S., Shian, S., Clarke, D. R. & Capasso, F. Large area metalenses: design, characterization, and mass manufacturing. *Opt. Express* **26**, 1573 (2018).

138. Sreenivasan, S. V., Willson, C. G., Schumaker, N. E. & Resnick, D. J. Low-cost nanostructure patterning using step and flash imprint lithography. *Nanostructure Sci. Metrol. Technol.* **4608**, 187–194 (2002).